Effects of crystal orientation and ferroelastic domain structure on the photochemical reactivity of $BiVO_4$ and related compounds

Submitted in partial fulfillment of the requirements for

the degree of

Doctor of Philosophy

in

Materials Science and Engineering

Ratiporn Munprom

B.S., Materials Engineering, Kasetsart University
M.S., Energy Science, Technology and Policy, Carnegie Mellon University

Carnegie Mellon University
Pittsburgh, PA

June, 2015

Acknowledgement

This doctoral work would not have been possible without the continual support and help from many people.

First and foremost, I would like to thank my advisors, Dr. Gregory S. Rohrer and Dr. Paul A. Salvador for their guidance and support throughout the course of my graduate research. They have given me great advice and encouragement, and they also set a good example how to be a good scientist. They taught me many things to help me successful in my thesis as well as in my future career. It has been my honor to work with them.

I also want to give special thanks to my committee members, Dr. Mohammad F. Islam, Dr. Marc De Graef and Dr. Kaushik Dayal, for their dedication. Their critical feedback and insightful suggestions added value to the work. In addition, I would like to acknowledge Dr.David Laughlin for an insightful discussion and the opportunity to learn more about ferroic materials. His expertise was really helpful.

I would not be able to come this far, if I did not receive essential contribution from great colleagues and friends. I'm grateful to the members of thin-film group and photochemistry group: Dr. Li Li, Dr. Lu Yan, Dr. Andy Schultz, Dr. Yiling Zhang, Miaolei Yan, Julia Wittkamper, Jimmy Glickstein, Yisi Zhu, Hang-Ah Park, and Siyuan Liu for their support and criticism. A special note of thank to Jason Wolf, Tom Nuhfer, Dr. Adam Wise, William Pingitore for all the help with instruments, Suzanne Smith, Jeanna Pekarcik and Marygrace Antkowski for their administrative assistance, and other MSE staff for their aid throughout this project. I also want to thanks Juliann, Doug and GCC staff for their helpful feedback on early written drafts and presentation. Without the support from these people, it would have been more difficult to complete this research.

I would like to take this opportunity to also thank all my friends for the support and more importantly, for their friendship. They have made my life more pleasant. My department friends, Dr. Li Huang, Dr. Stephanie Bojarski, Clayton Stein, Clare Mahoney, Vincent DeGeorge, Justin Freedman, Ellen Reifler, Lily Nguyen, Rachel Ferebee, Madeleine Kelly, and many more have provided support and created a positive atmosphere for doing work, particularly Dr. Sutatch Ratanaphan, Dr. Amy Wang and Hua Shan for their genuine kindness and enthusiastic support. Many thanks to the Thai community that added more fun and excitement to my life, has made me feel home, and helped me walk through this journey.

My sense of gratitude is extended to Academic development staff: Linda Hooper, John Lanyon, Donora Craighead, Jessica Owens and Dorene Powell. It has been a valuable experience working with them for years. In particular to John and his family, his has been my extended family and they deserve special recognition for all they have done for me. I am deeply grateful to know all of them.

Last but not least, I am thankful to the support of National Science Foundation grant DMR 1206656. Also, I dedicate my work to Anandamahidol Foundation for giving me financial support. As a fellowship receiver, I would like to express my highest gratitude to His Majesty King Bhumibol Adulyahdej of Thailand, who established the foundation as well as has been supporting Thai students in higher education for many years. Without this opportunity, I would not have been able to come to Carnegie Mellon University and pursue my dream. The foundation inspires me to learn as much as I can and find opportunities to give back to others. Above all, I would like to gratefully acknowledge the support and love of my family. They always give me encouragement and understanding unconditionally.

Ratiporn Munprom
June 2015

Abstract

Bismuth vanadate, $BiVO_4$, has been recognized for its high efficiency as a photoanode for water splitting. However, its performance is limited by photogenerated electron–hole recombination. Thus, researchers have attempted to modify $BiVO_4$ to improve its performance. One strategy to improve charge separation is to utilize an internal field arising from surface termination differences. Previous studies concentrated on polygonal single crystals of $BiVO_4$, providing limited information about the orientation-reactivity relationship. The current research focuses on polycrystalline $BiVO_4$, which makes it possible to study the photochemical reactivity of all possible orientations and determine the complete orientation dependence of the photochemical reactivity of $BiVO_4$.

$BiVO_4$ surfaces of all possible orientations have been used to photochemically reduce Ag^+ and oxidize Pb^{2+} and Mn^{2+}. The surface orientations of the grains, measured by electron backscatter diffraction, were correlated to the amounts of reduced and oxidized insoluble products on each grain. The results show that the photochemical reduction of Ag^+ is strongly favored on $BiVO_4$ (001) surfaces. However, Ag+ can be reduced on all orientations, with the rate of reduction decreasing with increasing inclination from the [001] direction. The oxidation of Pb^{2+} is strongly favored on (**hk**0) surfaces perpendicular to (001), and this is consistent with the result of the Mn^{2+} oxidation. Additionally, surfaces within 50 ° of [001] have a much lower activity for the oxidation of Pb^{2+}. The results also show that reduction and oxidation reactions occur on complementary surfaces of $BiVO_4$ crystals.

In addition to surface/crystal orientation, ferroelastic domains also affect the photochemical reactivity of monoclinic $BiVO_4$. The photo-reduction of Ag^+ and the photo-oxidation of Mn^{2+} are shown to occur on a certain set of ferroelastic domains, which are complementary to each other. Moreover, the domains generate contrast in piezoresponse force microscopy (PFM) that correlates to the reactivity, exactly like polar domains in ferroelectrics, such as $BiFeO_3$. This discovery is unexpected because $BiVO_4$ has a centrosymmetric structure, which should not exhibit such phenomena. However, surface polarity in centrosymmetric structures can be induced by flexoelectricity, which occurs when a strain gradient breaks the symmetry leading to a local polarization. Because symmetry is broken by surfaces, they provide a mechanism for the relaxation of internal stress that might create a strain gradient and impart flexoelectricity in a nonpolar material. These internal fields arising from ferroelastic domains in monoclinic $BiVO_4$ are Bismuth vanadate, $BiVO_4$, has been recognized for its high efficiency as a photoanode for water splitting. Previous studies showed that photochemical reactions in polygonal $BiVO_4$ were orientation-selective indicating improved charge separation by an internal field arising from surface termination differences. However, due to the limited numbers of orientations in the polygonal crystal structure, the orientation-reactivity relationship is not fully understood. As a result, the current research focuses on polycrystalline $BiVO_4$, which makes it possible to study the photochemical reactivity of all possible orientations and determine the complete orientation dependence of the photochemical reactivity of $BiVO_4$.

The photochemical reactivities of Ag^+ reduction, and Pb^{2+} and Mn^{2+} oxidation on a sintered $BiVO_4$ ceramic were correlated with the surface orientations of its grains, measured by electron backscatter diffraction. The results show that the photochemical reduction of Ag^+ is strongly favored on $BiVO_4$ (001) surfaces. However, Ag+ can be reduced on all orientations, with the rate of reduction decreasing with increasing inclination from the [001] direction. The oxidation of Pb^{2+} is strongly favored on (**hk**0) surfaces perpendicular to (001), and this is consistent with the result of the Mn^{2+} oxidation. Additionally, surfaces within 50 ° of [001] have a much lower activity for the oxidation of Pb^{2+}. The results also show that reduction and oxidation reactions occur on complementary surfaces of $BiVO_4$ crystals.

In addition to surface/crystal orientation, ferroelastic domains also affect the photochemical reactivity of monoclinic $BiVO_4$. The photo-reduction of Ag^+ and the photo-oxidation of Mn^{2+} are shown to occur on a certain set of ferroelastic domains, which are complementary to each other. Moreover, the domains generate contrast in piezoresponse force microscopy (PFM) that correlates to the reactivity, exactly like polar domains in ferroelectrics, such as $BiFeO_3$. This discovery is unexpected because $BiVO_4$ has a centrosymmetric structure, which should not exhibit such phenomena. However, surface polarity in centrosymmetric structures can be induced by flexoelectricity, which

occurs when a strain gradient breaks the symmetry leading to a local polarization. Because symmetry is broken by surfaces, they provide a mechanism for the relaxation of internal stress that might create a strain gradient and impart flexoelectricity in a nonpolar material. These internal fields arising from ferroelastic domains in monoclinic $BiVO_4$ are capable of improved charge separation and reduced recombination.

To better understand the contribution of the ferroelastic domain structure to improved reactivity, the domain and orientation dependent photochemical reduction of Ag^+ are investigated for two samples in the co-doped family $Na_{0.5x}Bi_{1-0.5x}Mo_xV_{1-x}O_4$: a monoclinic sample ($x = 0.05$) and a tetragonal sample ($x = 0.175$). Like $BiVO_4$, the co-doped $x = 0.05$ monoclinic sample has clear ferroelastic domains that exhibit contrast in piezoresponse force microscopy (PFM) and exhibit domain specific reactivity. The tetragonal $x = 0.175$ sample has no domains, no PFM contrast, and uniform grain reactivity. The orientation dependence of Ag^+ reduction is similar for the two samples, with surfaces near (001) being more active than others. For any given orientation, however, the monoclinic sample is quantitatively more active than the same orientation in the tetragonal sample. These collected results are consistent with the hypothesis that monoclinic-structured $BiVO_4$ ceramics have enhanced photochemical activity owing to ferroelastic domain-selective reactivity, which allows for local separation of photogenerated carriers and redox reactions.

List of Publications

1. **Munprom, R**., Salvador, P. A. & Rohrer, G. S. Polar Domains at the Surface of Centrosymmetric $BiVO_4$. *Chem. Mater.* **26,** 2774–2776 (2014).
2. **Munprom, R**., Salvador, P. A. & Rohrer, G. S. The orientation dependence of the photochemical reactivity of $BiVO_4$. *J. Mater. Chem. A* 3, 2370–2377 (2015).
3. (submitted) **Munprom, R.**, Salvador, P. A. & Rohrer, G. S. Ferroelastic Domains Improve Photochemical Reactivity: A Comparative Study of Monoclinic and Tetragonal $(Bi_{1-0.5x}Na_{0.5x})(V_{1-x}Mo_x)O_4$ Ceramics

Table of Contents

Table of Contents

List of Figures

List of Figures

List of Figures

List of Figures

List of Tables

INTRODUCTION

1.1 Motivation

With an increase in energy demand, solar fuel is one of the alternatives to fossil fuels that has gained flourishing attention. Solar fuel is produced by converting solar energy to chemical fuel, such as H_2.[1] This solar-to-fuel production could be relatively cost-effective because it utilizes a cost-free and abundant energy source of sunlight.[2] Moreover, unlike fossil fuels whose combustion significantly generates greenhouse gases (CO or CO_2), solar fuel technologies, because of their low-to-zero emissions of greenhouse gases, are more environmentally friendly.[3] Thus, researchers have devoted intense efforts to develop solar fuel technologies, aiming for robust and widespread deployment.

One of the promising solar fuel technologies that has been developed is photocatalytic water splitting.[4] This technology generates H_2 fuel by mimicking photosynthesis.[5,6] Specifically, solar energy is absorbed by a photocatalyst, which generates electrons and holes that can react with water to produce H_2 fuel and a clean by-product of O_2. Although the concept of photocatalytic water splitting seems simple, this technology is currently neither practical nor readily commercial because of its inefficiency.[7-9]

The main characteristics of photocatalysts that cause inefficiency to energy conversion are (1) solar harvesting ability, (2) carrier separating ability, and (3) reaction activating ability. [10] In other words, efficient photocatalysts should (1) absorb a large percentage of the solar spectrum, (2) effectively separate photogenerated electrons and holes before they recombine, and (3) provide active sites for the redox reactions. [11,12] The light absorbing ability of a photocatalyst can be determined by its band gap. The smaller the band gap is, the greater the fraction of light that is absorbed. Thus, narrow-band gap photocatalysts are desirable. [11] Additionally, charge separation and availability of the reaction sites increase the possibility of carriers reacting with water, leading to an increase of the overall efficiency. [13,14]

Considering all of the abovementioned characteristics, developing visible-light responsive photocatalysts with a robust charge separation and available active sites is challenging, yet essential. One viable class of materials whose charge separating ability has been attractive for photocatalytic applications is ferroelectrics. [15,16] Ferroelectrics have an internal dipole moment that can promote charge separation. [17] This dipole moment will govern the direction in which electrons and holes travel. Specifically, electrons are attracted to positively terminated surface domains, while holes are oppositely attracted to negatively terminated surface domains. [18] As a result, electrons and holes, as well as the reaction sites, are separated. However, most ferroelectric photocatalysts have a wide band gap, which limits their light absorbing ability, and thus the efficiencies. Therefore, numerous studies still examine emerging new options for photocatalytic materials that have all required properties or attempt to improve the performance of existing materials.

1.2 Objectives

The ultimate goal of this research is to understand photocatalytic activity of one chosen solar photocatalytic material, with an aim at increasing its overall efficiency. Specifically, this research aims to understand charge separation in a known visible-light responsive, non-ferroelectric photocatalytic material. While investigating the material, I uncovered a novel charge-separation method, which is investigated thoroughly herein.

To improve charge separation of photocatalysts, other than using ferroelectric materials, it is possible to use an internal electric field created by surface potential differences. This mechanism commonly has been observed in metal oxides, such as titania (TiO_2)[19], and lately has been recognized in bismuth vanadate ($BiVO_4$). [20] In particular to $BiVO_4$, recent studies showed an efficient separation of oxidation and reduction products, which was proposed to arise from surface potential difference in polygonal particles.[20,21]

Investigations into $BiVO_4$ photocatalysts have markedly increased because of several advantages $BiVO_4$ possesses. First, $BiVO_4$ has a visible-light active band gap.[22] Importantly, it also has been shown to be highly efficient for photocatalytic water oxidation (high activity with low losses). [23-25] Moreover, this oxide is chemically stable and affordable. [23] Given these benefits, $BiVO_4$ is a material of interest for this research and it is important to fully understand its photochemical properties, with an aim of improving efficiency for practical applications.

To obtain a better understanding, this research is separated into 3 main studies.

Study 1: Orientation dependence of the reactivity of monoclinic $BiVO_4$

Following upon the reported facet-specific reactivity of polygonal particles, I first examined the influence of orientations on the surface reactivity of polished dense polycrystalline compacts, which expose many more surface orientations than faceted particles and which should allow us to propose an optimal geometry for a $BiVO_4$ photocatalytic microcrystal.

Study 2: Domain selectivity of photochemical reactions on monoclinic $BiVO_4$

In the course of investigating orientation dependent reactivity in Study 1, I observed an anomalous spatially-selective reactivity on $BiVO_4$, where the supposedly non-polar ferroelastic domains appeared to influence reactivity. This is explored in detail in Study 2, a possible explanation is proposed, and implications of this anomalous reactivity are described.

Study 3: Effect of the ferroelastic domain structure on photochemical properties of monoclinic $BiVO_4$

In Study 2, ferroelastic domains are shown to separate reaction products on $BiVO_4$, likely owing to the separation of charges in these domains. In Study 3, I determine the role of the ferroelastic domains, such as domain existence, on the overall level of reactivity, by comparing absolute reactivity of similar ferroelastic and non-ferroelastic compounds in the $BiVO_4$ family.

The following is an overview of each study.

Study 1: Orientation dependence of the reactivity of monoclinic $BiVO_4$

Many factors, such as orientation and residual strain, can affect photochemical properties of materials. [19,26] $BiVO_4$ is one material where the surface orientation is known to significantly impact its photocatalytic properties.[20,21] Such orientation dependence was also discovered in other metal oxides, such as TiO_2[19] and $SrTiO_3$.[27] In particular to $BiVO_4$, the spatial separation of photochemical reactions was found in a faceted microcrystal: the reduction reaction mainly occurred on (001) facets, while the oxidation reaction mainly occurred on (011) facets.[20] This result also implied that photogenerated electrons were preferentially driven to (001) facets, while photogenerated holes were preferentially driven to (011) facets. Additionally, it proposed that the potential difference of facets may be a mechanism leading to a separation of photogenerated carriers.[20] This knowledge of orientation-dependent reactivity allows researchers to design an efficient photocatalyst. For example, the ideal photocatalyst should be comprised of a combination of the orientations that provide the highest reactivity for both reduction and oxidation. To determine an ideal design, it is necessary to understand the relationship between orientations and reactivity. However, the orientation-dependent photocatalytic properties in $BiVO_4$ have not been fully explored. Previous $BiVO_4$ studies, which concentrated on single crystal and micro- or nano-crystalline structures, offer limited information on the correlation between all possible orientations and reactivity.[20,21,28] Specifically, only the reactivities of the {001} and {101} surfaces could be obtained.[20] To completely understand the orientation-reactivity relationship, a sintered polycrystalline $BiVO_4$ should be studied because it can offer all possible orientations on the surface so that an effective design for a highly efficient photcatalyst can be suggested.

The previous study of polygonal $BiVO_4$ led to the conclusion that the {001} surface is the most favorable orientation for reduction and the {011} surface is the most favorable orientation for oxidation. The preference of reactions possibly occurs to meet the requirement of photocatalytic processes; specifically, both reduction and oxidation need to happen to complete the process. However, because there were only two choices, these particular surfaces may simply be the best available for the two reactions. In other words, if electrons are preferentially driven to {001} surface, such a surface will favor reduction and thus make the only other available surface (which is {011}) favorable for oxidation. This is always a limitation of samples with a small number of surfaces. In this study, a polycrystalline ceramic is used, which exposes all orientations, and thus makes it possible to determine the complete orientation-reactivity relationship.

Research Question

Based on this abovementioned knowledge, the main question to address in this study is:

What are the most favorable orientations for reduction and oxidation reactions for $BiVO_4$?

Hypothesis: The orientation-dependent photochemical properties of a monoclinic $BiVO_4$ ceramic will differ from that of polygonal $BiVO_4$ crystals because the availability of all orientations will allow for a more complete determination of reaction preferences.

To test this hypothesis, a polycrystalline monoclinic $BiVO_4$ sample was prepared by solid-state reaction. Then, the orientations of many grains at the sample surface were measured by electron backscatter diffraction (EBSD). After the photochemical experiment, insoluble products were found on the surface, which were imaged by atomic force microscopy (AFM). A correlation between the orientation and reactivity was analyzed and compared to the result of faceted $BiVO_4$ particles studied by Li *et al.*[20]

Study 2: Domain selectivity of photochemical reactions on monoclinic $BiVO_4$

Study 2 first reports anomalous reactivity observed on the surfaces of monoclinic $BiVO_4$ in Study 1. This anomaly has never been demonstrated in $BiVO_4$ or any ferroelastic material.

While investigating the orientation dependence of the photochemical reactivity, I observed domain-selectivity of the photochemical reactivity, similar to that observed in ferroelectrics. Specifically, the photochemical reduction was selective on some domains, while the photochemical oxidation was selective on some domains. The domain-selective reactivity in ferroelectric materials is caused by their internal polarization, which can drive electrons and holes to separate domains. Thus, it is speculated that a similar effect may happen in $BiVO_4$, leading to a separation of reactions by ferroelastic domains. In following up on this observation, it was shown that they occurred on complementary domains. In addition, the surface of bulk $BiVO_4$ had a piezoresponse under piezoresponse force microscopy (PFM), indicating the polarity of the surface. Finally, the reactivity was shown to correlate with the piezoresponsive domains. These results are similar to the photochemical behavior of ferroelectrics. However, because $BiVO_4$ is centrosymmetric, its surface should not be polar and, therefore, have neither domain-selective reactivity nor piezoresponsive surfaces.

The piezoelectric effect that resulted in a response in PFM measurement was thought to be restricted to non-centrosymmetric materials and, previously, only been observed in those materials. However, a similar effect can occur in centrosymmetric materials, called the flexoelectric effect, which describes a linear relationship between electric polarization and a gradient in the strain. The spontaneous polarization arising from flexoelectricity is caused by the symmetry-breaking effects of the surface and microstructure. The broken symmetry may originate from an inhomogeneous strain and result in a local dipole moment. Hypothetically, flexoelectricity can lead to ferroelectric-like behavior in centrosymmetric materials.

The concept of flexoelectricity is not new, but it has not been thoroughly investigated because it is believed to have a small effect, especially in bulk materials. Recently, however, there has been much excitement about flexoelectricity because it shows a surprising impact on nanoscale materials.[29] Even though it can play a significant role in small-scale materials, the effect of flexoelectricity on ferroelastic domains with submicron dimensions is unknown. Thus, it is also possible that this effect can be significantly strong in ferroelastic domains.

Flexoelectricity, or a strain-gradient induced polarization, seems promising for many applications, such as flexoelectric nano-generators.[30] Photocatalytic applications, including photocatalytic water splitting, are also a potential research area that can utilize flexoelectricity to improve performance. Induced polarization can promote the separation of electrons and holes, and thus enhance efficiency. However, flexoelectrcity has not been studied in the context of photocatalysts. Thus, the objective of this Study 2 is to demonstrate the implications of surface polarity in centric materials, leading to domain-selective reactivity in monoclinic $BiVO_4$ as well as improved charge separation. These notable results can provide an alternative approach to improve charge separation and open up material choices for photocatalytic applications. Plus, because of induced surface polarity, centric materials can potentially be expanded into more functionality.

Study 3: Effect of the ferroelastic domain structure on photochemical properties of monoclinic $BiVO_4$

Our previous results showed that photochemical reactions could occur on any orientation although they preferentially occurred on a particular orientation. This result is distinct from the results from polygonal $BiVO_4$, which suggests that the reactions only happen on specific facets. The dissimilarity of the results may be caused by polarity on our monoclinic $BiVO_4$ surfaces which lead to domain selectivity of photochemical reactivity. Thus, it is likely that ferroelastic domains can improve photochemical properties in $BiVO_4$. Therefore, the objective of this study is to better understand the effect of ferroelastic domains on photochemical properties.

It is hypothesized that residual transformation strain can induce polarization in monoclinic $BiVO_4$ and result in an improved charge separation as well as enhanced reactivity. Monoclinic $BiVO_4$ is a ferroelastic material which undergoes a phase transition at 255 °C. As a result of a symmetry reduction from the phase transition, ferroelastic domains are formed upon cooling. This transition leaves a residual strain in the material. Such a residual transformation strain can break centrosymmetric symmetry, leading to surface domain polarization and the domain-selective reactivity. In other words, the structural transition can induce a local dipole moment that drives the photogenerated charge carriers in opposite directions, according to their charge. Importantly, this phenomenon can help separate electron-hole pairs and consequently improve photochemical reactivity. In addition to the charge separation, ferroelastic domains are appealing for photocatalytic applications because they can ideally serve as active sites for reduction and oxidation, allowing both reactions to occur simultaneously on the same surface orientation.

Research questions

Study 3 attempts to answer the following questions to achieve a thorough understanding of the influence of ferroelasticity on the photochemical properties in monoclinic $BiVO_4$.

1. What is the effect of the ferroelastic transformation on the photochemical properties of monoclinic $BiVO_4$?

a. Can the transition lead to different surface properties? Specifically, will the monoclinic-structured and tetragonal-structured samples of $BiVO_4$ have the same surface properties (surface topography, surface polarity)?
b. Does the ferroelastic domain structure improve the reactivity of $BiVO_4$?

Hypotheses: The formation of ferroelastic domains results in the appearance of piezoresponsive surface domains, which can promote charge separation and improve the photochemical reactivity of monoclinic $BiVO_4$.

To test this hypothesis, the orientation dependence of reactivity of the tetragonal-structured sample was compared to that of the monoclinic-structured sample. However, to obtain tetragonal scheelite $BiVO_4$, the ferroelastic transformation has to be suppressed: doping was used to stabilize a tetragonally structured solid solution phase of $BiVO_4$. This suppression can be accomplished by substituting other ions on A sites and B sites of $BiVO_4$. For example, a substitution of Na and Mo on Bi and V sites, respectively, can inhibit the transition and maintain the structure of tetragonal scheelite at room temperature.[31]

It should be noted that, by varying x in $Na_{0.5x}Bi_{1-0.5x}Mo_xV_{1-x}O_4$, the temperature of the tetragonal-to-monoclinic transformation changes. For a composition (x) of 0.1, the transition temperature is approximately room temperature. In other words, at room temperature, monoclinic and tetragonal phases are obtained at $x < 0.1$ and $x > 0.1$, respectively.[31] For this particular study, $Na_{0.5x}Bi_{1-0.5x}Mo_xV_{1-x}O_4$ with $x = 0.05$ and $x = 0.175$ were investigated.

By investigating the surface structure and properties with PFM, the images of the monoclinic-structured sample should show a contrast indicating piezoresponsive surfaces. On the contrary, the tetragonal-structured sample, which does not undergo the phase transition, should not show a piezoresponse. Similarly, only topographic images of the monoclinic-structured sample should exhibit domain-selective photochemical reactions. Hypothetically, if the orientation-dependent reactivity of these differently structured samples is compared, the monoclinic one should have higher reactivity.

In summary, the goal is to understand how the ferroelastic domain structure is related to the photochemical properties. These three studies could lead to a strategy to improve the photochemical properties in ferroelastic $BiVO_4$ as well as other ferroelastic materials. Plus, this knowledge potentially broadens the functionality of ferroelasticity into other practical applications.

1.3 Organization

This document contains seven chapters. It starts with this introductory chapter, and the remaining chapters are:

- Chapter 2 reviews the relevant literature and background information including photocatalytic water splitting, the concept of flexoelectricity, and properties of bismuth vanadate ($BiVO_4$), such as structure and ferroelasticity, will be explained.
- Chapter 3 introduces the details of the experimental techniques used to test the hypotheses.
- In Chapter 4, I discuss the orientation-dependent photochemical reactivity in a sintered polycrystalline $BiVO_4$ (Study 1).

- Chapter 5 demonstrates the anomalous domain-selectivity of photochemical reactions (Study 2).
- Chapter 6 addresses the effect of the ferroelastic nature on surface properties and photochemical properties (Study 3).
- Chapter 7 summarizes all the results and key findings. Also, the future direction of the research will be suggested.

Chapter 2

BACKGROUND

This chapter provides supporting background information that is related to this dissertation. First, the basic idea of water splitting processes is discussed along with a literature review of the photocatalytic developments associated to bismuth vanadate. Second, a brief explanation of both flexoelectricity and piezoelectricity is provided as well as a comparison of the similarities and differences between the flexoelectric and the piezoelectric effects. Lastly, understanding $BiVO_4$ properties is essential because it is related to the articulation of the observed phenomena. These topics are important to understand the basis of this research.

2.1 Photocatalytic water splitting

2.1.1 Principle

A photocatalytic water splitting mechanism involves harvesting solar energy and then turning water into chemical fuel with an assistance of a photocatalyst material.[32] The concept of water splitting is simple. Basically, the process requires abundant supplies of sunlight and water in addition to a photocatalytic material. This process produces clean H_2 and O_2 gases, which is one of its advantages over a fossil fuel combustion that generates greenhouse gases, primarily CO_2. This technology is promising for mitigating environmental problems. Given these advantages, photocatalytic water splitting has enormous potential as a clean and cost-effective alternative for H_2 fuel production.[1]

In general, the overall process of water splitting consists of three crucial steps as illustrated in Fig. 2.1.[4]

(i) Light absorption: a photocatalyst absorbs sunlight resulting in the generation of electrons and holes. The solar energy required for the carrier excitation is determined by the energy of the band gap (E_g).

(ii) Charge separation and diffusion: after solar energy has been absorbed, an electron is excited from the valance band to the conduction band. This electronic excitation also results in the creation of a hole in the valence band. The photogenerated electrons and holes, then, diffuse to photocatalyst surfaces in contact with water (ii.1) to evolve H_2 and O_2 in the next step. Otherwise, electrons and holes can recombine (ii.2).

(iii) H_2/O_2 evolution: the water decomposition step involves two half reactions, namely reduction and oxidation. Electrons participate in the reduction reaction (iii.1), which evolves H_2 fuel, while holes participate in the oxidation reaction (iii.2), which evolves O_2 gas. The chemical reduction and oxidation reactions for water splitting are listed in Eq. (2.1) and (2.2), respectively:

$$2H^+ + 2e^- = H_{2(g)} \qquad (2.1)$$

$$H_2O + 2h^+ = 1/2O_{2(g)} + 2H^+ \qquad (2.2)$$

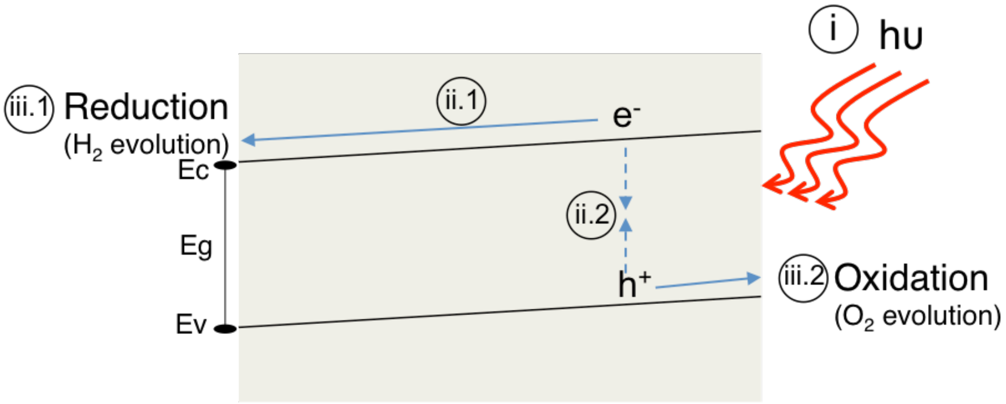

Figure 2.1. A photocatalytic water splitting mechanism. The diagram shows three main steps in photocatalytic water splitting. First, a photocatalyst absorbs light to generate charge carriers. Then, charge carriers diffuse to surface reaction sites to participate in the redox reactions.

The efficiency of each of the three steps affects the overall efficiency of photocatalytic water splitting, which is still relatively low for all practical materials. The inefficiency becomes a main obstacle that prevents this technology from becoming widespread.[8] As a result, selecting a proper material is a key step for designing an efficient photocatalyst.

Over decades, many materials have been explored as water splitting photocatalysts; however, metal oxides are the most commonly employed material in this technology since it was first discovered in TiO_2 by Fujishima and Honda in 1972.[33,34] The popularity of oxide photocatalysts is because of their cost-effectiveness and water-stability.[8,35] However, there are still many concerns with using oxide photocatalysts, including their light-absorbing and charge-separating abilities.

2.1.2 Challenges and recent developments in photocatalyst materials

It will not be possible to achieve high water-splitting efficiency without the design and optimization of photocatalytic materials. For example, a photocatalyst needs to have a band structure with the appropriate band gap energy and band-edge positions, as well as ability to separate electron-hole pairs.[35] This section emphasizes three primary challenges that affect photocatalytic efficiency: (1) band structure optimization, (2) charge separation enhancement and (3) active site promotion. Also, strategies to improve efficiency will be discussed including the ones for $BiVO_4$, which is the material of interest for this thesis work.

(1) Band structure optimization

In general, to optimize a band structure, two key characteristics associated with materials properties need to be considered: the band gap width (E_g) and band edge locations (E_c and E_v). A band gap width determines the amount of light being absorbed, or the light-harvesting efficiency. Band edge positions of the conduction and valence bands allow the H_2 and O_2 evolution and determine if the reactions can occur or not. Clearly, a desirable band gap width and appropriate potentials of the conduction and valence bands are essential for efficiently water-splitting photocatalysts.

(i) Band gap width

A band gap width limits the amount of light being absorbed by a material. Specifically, a photocatalyst can only absorb light with energy larger than the band gap. If more light is absorbed with an energy greater than the energy needed to split water, then the efficiency is higher. Across the entire range of the solar spectrum, visible light offers the most significant fraction (~32% of the solar spectrum).[36] Consequently, an ideal photocatalyst should be able to absorb the light in a visible light range.

Visible light absorption is one of the major challenges. Many oxides have been intensively investigated for photocatalytic applications.[15] However, the options of visible-light responsive materials are limited. Some examples of visible-light responsive oxide photocatalysts include Fe_2O_3,[37] Cu_2O,[38] WO_3[39] and $BiVO_4$.[40] As a result, researchers are attempting to improve the light-absorbing ability of existing wide-band gap photocatalysts to increase the number of material choices as well as efficiency.

Band gap engineering becomes especially valuable when altering the band structure, which is one strategy to increase efficiency. Such band gap engineering results in a change in electronic properties of materials.[41] In general, a simple method to change the band structure is doping impurity atoms. Dopants provide an excess charge carrier concentration, which causes a change in electronic structure, for example, a shift in a Fermi level and a formation of a donor level within the band gap.[42] These changes may cause changes in absorption ability as well.

In particular to $BiVO_4$, an investigation of the effect of metal doping on photoelectrocatalytic properties was carried out by H.S Park *et al*.[43] The study focused on molybdenum (Mo) and tungsten (W) dopants which are commonly used for $BiVO_4$ doping. The experimental result showed that the photooxidation current measured from Mo-doped $BiVO_4$ is three times greater than undoped $BiVO_4$. Additionally, doping with 4-8 at%W can enhance the photocurrent about 7 – 9 times depending on the dopant concentration. Furthermore, 25% additional photocurrent increment from the W-doped $BiVO_4$ can be obtained from co-doping with both Mo and W. In Park's study,[43] a simulation based on a first-principles density-functional calculation was also conducted to explain the effect of doping on the increased photocatalytic properties. The result of the simulated electronic structure revealed that the carrier density was enhanced because the impurity elements substituted at V sites, namely Mo and W, have an extra electron compared to the host atom of vadanium. Moreover, the Fermi level was shifted to inside the conduction band. Besides, there also was a formation of a localized state in the band gap. These changes in the band structure could lead to lower energy needed to generate charge carriers as a consequence of band engineering.

In addition to the change in band structure, doping can affect a charge separation in $BiVO_4$. The study of Park *et al.*[43] pointed out that the increased carrier concentration may result in an increase of an electric field in the space charge region, which can promote charge separation. The agreement of the increased charge separation was also demonstrated by other studies[44,45] revealing that the improvement of the charge separation resulted from the nature of W and Mo dopants that had a shallow-donor behavior and low formation energies. As a result, the photocatalytic properties of doped $BiVO_4$ were enhanced. Although increasing dopant concentrations may give rise to an increase in photocatalytic activity, adding dopants exceeding the optimum point could decrease the performance because excess impurities become scattering centers, which increase recombination.

Doping can also help improve conductivity and thereby efficiency.[46] Abdi *et al.* revealed that $BiVO_4$'s photocatalytic efficiency was limited by its carrier transport, specifically poor carrier mobility.[47] In fact, compared with other photocatalytic materials, namely Fe_2O_3 (0.5 cm^2 V^{-1} s^{-1}),[48] Cu_2O (6 cm^2 V^{-1} s^{-1}),[49] and WO_3 (10 cm^2 V^{-1} s^{-1}),[50] an electron mobility of $BiVO_4$ (0.04 – 0.2 cm^2 V^{-1} s^{-1})[47,51] is significantly lower. As a result, doping with W can increase carrier mobility resulting in enhanced efficiency.

(ii) Band edge positions

Besides the band gap, the position of the band edge should be considered for its effect on the reaction. Specifically, photogenerated charge carriers that are transferred to the surface need to participate in a redox catalytic reaction at the solid-solution interface. Consequently, the conduction band edge should be more positive than the energy level of a reduction reaction so that electrons can participate in the redox reduction. Similarly, for holes to participate in a redox oxidation, the valence band edge has to be more negative than the energy level of the oxidation reaction. In the case of water splitting processes, as shown in Fig. 2.2, the band edge positions have to straddle the energy level of H+/H_2 at 0 eV and the energy level of O_2/H_2O at +1.23 eV.[32,36] This requirement also relates to the minimum band gap needed to split water. Specifically, the ideal minimum band gap that can split water is 1.23 eV. However, in practice, the minimum required energy is ~1.7 eV because the overpotential should be taken into account to compensate energy losses through the process.[52]

Unfortunately, not many materials, especially for visible-light absorbing materials, can meet the requirement of the energy levels for both reactions. In the case of $BiVO_4$, its valance band aligns below the O_2 evolution level, meaning that $BiVO_4$ can oxidize water; however, the conduction band edge of $BiVO_4$ is slightly lower than the H_2 evolution level. Therefore, $BiVO_4$ cannot reduce protons to hydrogen gas.

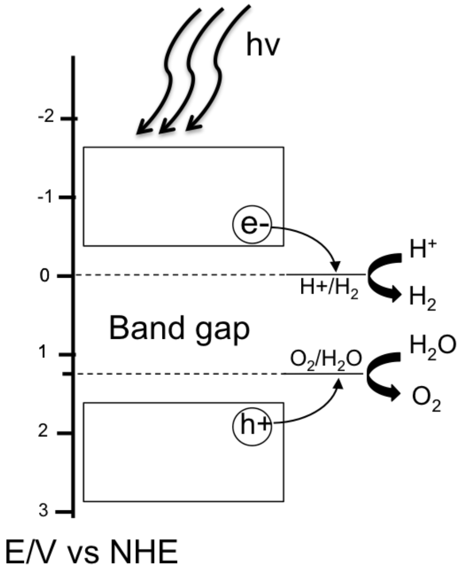

Figure 2.2. The appropriate band edge level for water splitting (modified from Ref. 36)

One of the strategic modifications to obtain both H_2 and O_2 evolution is to construct a composite photocatalyst.[36] Fig. 2.3 displays the mechanism of a composite structure composed of dual-photocatalyst system: one for H_2 evolution and another one for O_2 evolution. An electron mediator, aligning between two photocatalysts, accepts charge carriers from the photocatalysts that do not participate in the reactions. These carriers usually recombine in a layer of the electron mediator. An advantage of this system is that each photocatalyst only needs to overcome the thermodynamic requirement of one redox reaction, so it opens up more material choices. Additionally, the heterogeneous structure can also promote charge separation. The potential offset at the interface will be an internal force assisting a separation of electrons and holes, which can increase photocatalytic activity.[53]

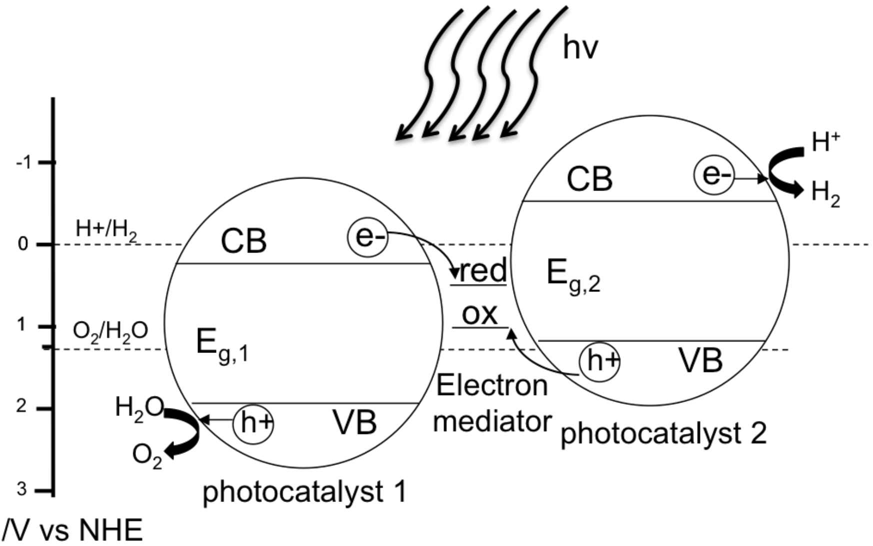

Figure 2.3. The mechanism of a composite structure or the so-called Z-scheme method (modified from Ref. 36)

Fig. 2.4(a) demonstrates a heterogeneous system of $BiVO_4$ and $SrTiO_3$:Rh particles. In this system, because $BiVO_4$ can only oxidize water, $SrTiO_3$:Rh particles attached on $BiVO_4$ act as a reaction site for water reduction. Previous studies[54,55] observed the H_2 and O_2 evolution from a $BiVO_4$-$SrTiO_3$:Rh composite photocatalyst. It should be also noted that for this particular system an electron mediator is not needed. In other words, electrons can be injected from $BiVO_4$ photocatalyst to $SrTiO_3$:Rh photacatalyst across the interface without an electron mediator. The result showed that water can be split to H_2 and O_2 with this composite catalyst.

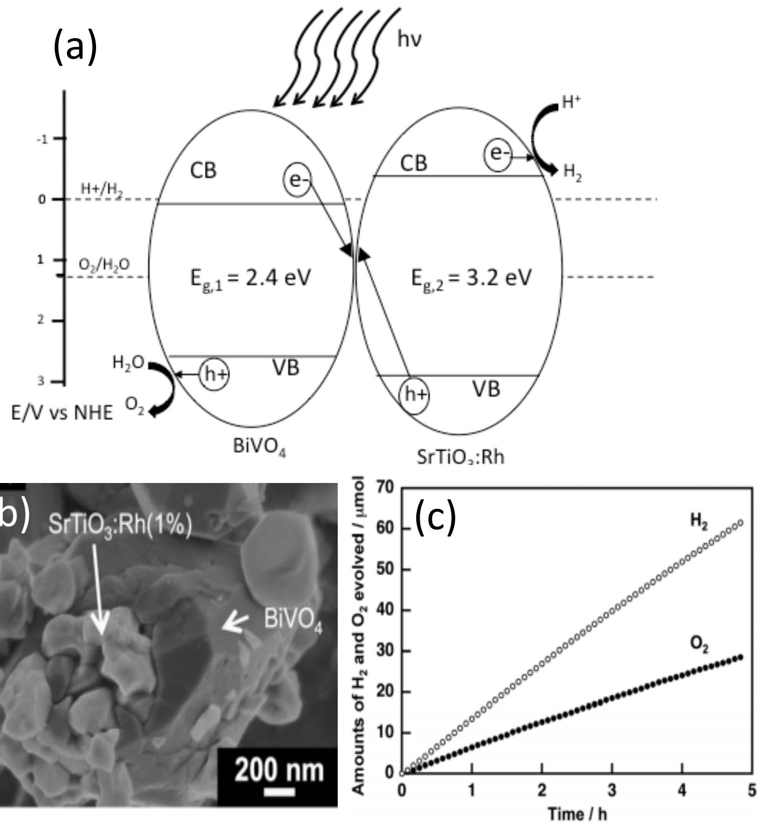

Figure 2.4. (a) The mechanism, (b) morphology[14], and (c) H_2 and O_2 produced of a heterogeneous $BiVO_4$/ $SrTiO_3$:Rh photocatalyst.[55]

Even though the band structure modifications can improve photocatalytic water splitting efficiency, there still are some other issues that should be addressed, namely a separation of electrons and holes, and availability and accessibility of active sites.

(2) Charge separation enhancement

Charge separation is a crucial characteristic that mainly restricts the efficiency of photocatalysts. Various methods can be employed to increase charge separation, such as tandem-structured photocatalysts. Even though a built-in potential at the interface of the heterogeneous photocatalysts can facilitate charge separation, an efficiency loss due to interfacial defects could also happen. Another strategy to improve the charge separation is to use ferroelectric materials. Unlike the heterogeneous structure, limited efficiency at the interface is not a concern in a homogeneous structure of ferroelectrics. Due to this advantage, the present discussion will thus mainly focus on ferroelectric photocatalysts.

Ferroelectrics have a spontaneously internal electric field that can drive electrons and holes to opposite directions. The internal dipole moment is only possible if the crystal structure is non-centrosymmetric.[16] In other words, an off-centered atom induces a local charge as well as an internal polarity. As a result, the ferroelectric effect is restricted to certain non-centrosymmetric crystallographic structures. Furthermore, the directions of the atomic displacements determine the orientation of polarization or dipole moment. As shown in Fig. 2.5, if the central atom is shifted off its position, the dipole moment or polarization is induced due to the unbalanced charge with respect to the centered position. If the atom shifts up relative to the center of the structure, a dipole moment is generated in this direction. Conversely, the opposite shift of the centered atom produces an opposite sign of the polarization. Because of the internal polarization, charge carriers are driven in a certain direction corresponding to the orientation of polarization. Such carriers can also result in a surface charge, or surface polarity. A region where the polarization is uniformly oriented is called a domain. Such domains are a common feature in ferroic materials including ferroelectrics. Different ferroelectric domains can possess distinctive directions of polarizations which drive the charge carriers to certain directions. Ferroelectric materials that have been used for photocatalytic water splitting are $BaTiO_3$, $PbTiO_3$, $Pb(Zr, Ti)O_3$ (PZT) and $BiFeO_3$.[15,16,56]

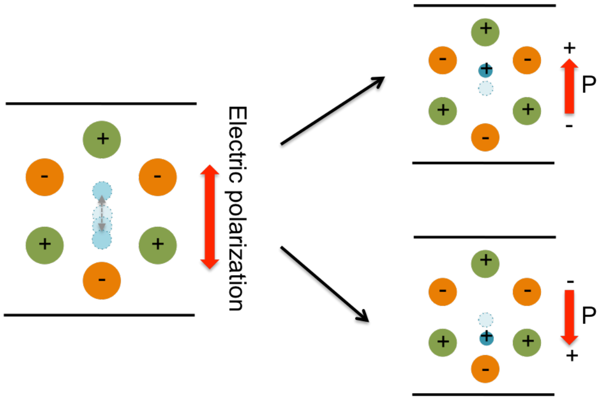

Figure 2.5. Schematic description of an internal dipole moment induced due to a lack of centrosymmetry

Previous studies show a promising result of spatial separation of redox reactions by internal polarization of ferroelectrics. For instance, Fig. 2.6 displays the surface of {001} $BaTiO_3$ single crystal after the reduction of silver (Fig. 2.6(a)) and the oxidation of lead (Fig. 2.6(b)).[57] It is clear that the reactions were spatially selective. In other words, only some certain domains would reduce silver ions, while some other domains would oxidize lead ions. The spatial selectivity of the reactions was also complementary. Further experiments revealed that the reducing domains and the oxidizing domains possessed a positively charged and a negatively charged surface, respectively. This spatial separation also implies a mitigation of carrier recombination, leading to an increase in photocatalytic activity. Despite their effective charge separation, ferroelectrics mostly have wide band gaps resulting in poor light absorption. As a result, developing visible-light absorbing photocatalyst materials with an internal dipole moment would be promising.

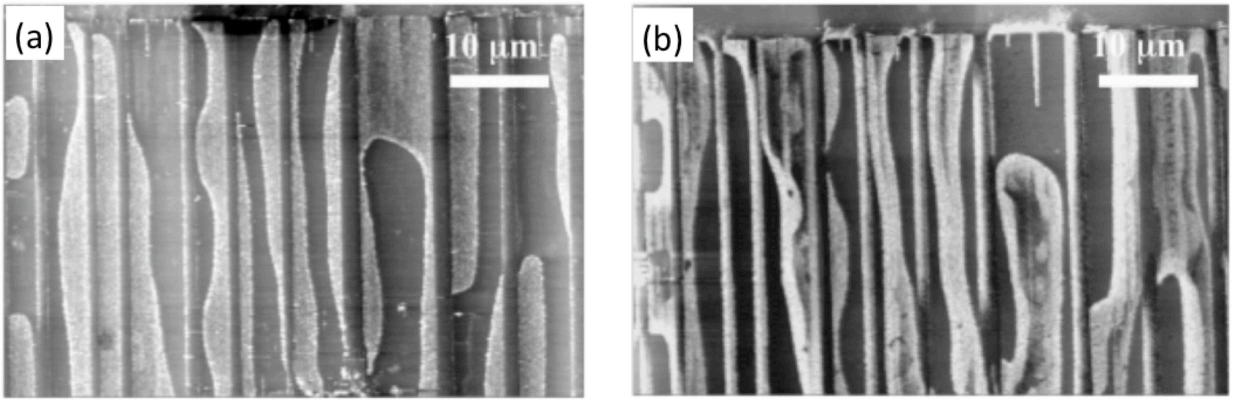

Figure 2.6. The surface of {001} $BaTiO_3$ single crystal after (a) the reduction of silver and (b) the oxidation of lead.[57]

In recent years, there have been many attempts to improve the performance of photocatalysts including band engineering by doping, composite formation, and the use of ferroelectrics. The above-mentioned methods are some potential strategies that are widely used. Other developments also include, for example, surface and morphology modifications. In this study, a novel strategy is proposed to enhance charge separation in a narrow band gap semiconductor. Flexoelectricity can result in a surface polarity that, when present in a narrow-band gap $BiVO_4$, may result in improved charge separation in a visible-light absorbing non-ferroelectric. As a result, this narrow band gap material will have a suitable band gap as well as internal charge separation.

(3) Active site promotion

To activate chemical reactions, charge carriers need to reach the solid-solution interface. When electrons and holes are photogenerated, if active sites are neither provided nor accessible at the interface, the charge carriers will not be able to react and will, instead, recombine. Therefore, availability and accessibility of active sites at the interface are essential for photocatalytic water splitting.

Co-catalysts are commonly used to promote active reaction sites for photocatalysts. Also, co-catalysts can improve the kinetics of surface reactions so that the surface reactions are not a limiting step. The main drawback of co-catalysts is that the materials often used as co-catalysts are expensive noble metals, such as Pt and Au. In particular for $BiVO_4$, IrO_x, Co_3O_4, Co-Pi and Pt have been used to modify $BiVO_4$.[25] Among the aforementioned co-catalysts, Ye *et al*.[58] showed that a Pt-loaded $BiVO_4$ photoanode obtained the highest enhanced photocurrent. Even though it can improve the performance, this method is not cost-effective.

In this research, I demonstrate a practical and cost-effective strategy that can be accommodated by inexpensive ferroelastic materials. Available sites are promoted using the ferroelastic domain structure. Specifically, ferroelastic domains, which are naturally formed as a result of symmetry reduction as part of a phase transition to the ferroelastic state, can potentially serve as active sites at the surface so that reduction and oxidation reactions can occur simultaneously, but at spatially distinct locations.

2.2 Flexoelectricity in solids

The terminology of 'flexoelectricity' is assigned to describe a linear coupling between a mechanical strain gradient and an electric polarization. This electromechanical coupling can arise in liquid crystals and dielectric solids.[59] However, in this research, I am focusing on flexoelectricity in solid materials, especially in ferroelastics. I will discuss the conceptual basis as well as relevant theoretical and experimental studies.

2.2.1 The contributions to flexoelectricity

The flexoelectric effect in solid was discovered in the 1950s-1960s;[59,60] however, it is not well studied especially in bulk materials because the effect has been shown by theoretical and experimental studies to have a small magnitude in bulk materials.[59] Recently, much attention has been paid since its strong impact was found in nanoscale materials and ferroelectrics.[61–64] The strong flexoelectric effect at the nanoscale is related to the reduction in sample size. In other words, the flexoelectric effect is enhanced by size reduction. Previous studies have demonstrated that if the sample size is decreased to the nanoscale, strain gradients can be relatively large and thus leads to a strong flexoelectric effect. Such a strong flexoelectric effect is also found in high-κ materials, such as ferroelectrics. Even though the magnitude of flexoelectricity is proportional to a dielectric permittivity, it is possible that flexoelectric polarization adds to an existing internal dipole moment in ferroelectrics and consequently increases the magnitude of the overall polarization.[61,64,65] Importantly, because flexoelectricity is not restricted by crystal symmetry, it can induce polarization in non-piezoelectric materials. This phenomenon leads to recent developments of piezoelectric metamaterials, which have piezoelectric properties without piezoelectric components.[29] These previous investigations demonstrated that the flexoelectric effect can play a significant role in a broad class of materials including both non-centrosymmetric and centrosymmetric materials,[65] opening up more material choices that can be used for piezoelectric- or ferroelectric-related applications. As a result, a fundamental understanding of this effect is vital to exploit flexoelectricity to practical technologies.

In general, flexoelectricity is composed of four contributions: (1) static bulk flexoelectricity, (2) dynamic bulk flexoelectricity, (3) surface piezoelectricity, and (4) surface flexoelectricity.[59,66] The following will discuss each contribution in detail.

(1) Static bulk flexoelectricity

Static bulk flexoelectricity describes a polarization response to a static uniform strain gradient. Considering a rigid-ion model, in the presence of a uniform strain gradient, an atom at position *R* is shifted with a distance *r*, making a final position equivalent to *R*+*r*. This movement of atoms can cause a change of the polarization in the crystal. Hypothetically, one could say that the static bulk effect is caused by an inhomogeneity of atomic displacements, which leads to local polarization in a unit cell.

Generally, the coupling between a polarization and a strain in crystalline dielectrics can be described by Eq. (2.3):

$$P_i = d_{ijk}\varepsilon_{jk} + \mu_{ijkl}\frac{\partial \varepsilon_{jk}}{\partial x_l} \qquad (2.3)$$

where P_i is the polarization, ε_{jk} is the uniform mechanical strain, d_{ijk} is a third-rank piezoelectric tensor, $\partial\varepsilon_{kl}/\partial x_j$ is a strain gradient, and μ_{ijkl} is a fourth-rank flexoelectric tensor. Equation 2.3 expresses the direct effect. The first term on the right hand side of the equation describes a linear polarization response to a homogeneous deformation. Such a term is related to the direct piezoelectric effect belonging to piezoelectric or non-centrosymmetric materials. For non-piezoelectric materials, the components of the piezoelectric tensor are zero, which makes this first term become zero. The second term on the right-hand side of the equation introduces a linear coupling between a polarization and a strain gradient with the absence of electric field known as the direct flexoelectric effect. Such a relationship is a basic description of flexoelectricity and indicates that an inhomogeneous deformation can create a polarization.

In addition to the direct effect, for any crystalline dielectric, the converse effect can be expressed as Eq. (2.4):

$$T_{ij} = d_{ijk}E_k + \mu_{ijkl}\frac{\partial E_k}{\partial x_l} \tag{2.4}$$

where T_{ij} denotes a mechanical stress, d_{ijk} is a piezoelectric constant. E_k is an electrical field, and μ_{ijkl} is a flexoelectric tensor. Please note that $d_{ijk}$is the counterpart of the piezoelectric tensor in the direct effect.

The converse effect mainly defines the linear relationship between the applied electric field (or electric field gradient) and the induced elastic stress. Similar to the direct effect, the first right-hand-side term describes the converse piezoelectric effect, while the second term is the converse flexoelectric effect. Please note that the converse piezoelectric effect is also a principle effect of piezoelectric force microscopy; a voltage is applied to measure a piezoelectric response of a material.

From the equation, in principle, an inhomogeneity of a polarization (or an electric field) is needed to induce the converse flexoelectric effect. As a result, the application of a uniform electric field should not lead to the crystal deformation. However, in practice, Tagantsev and Yurkov[60] demonstrated that a homogenous polarization can possibly lead to a stress or strain similar to a bending effect. They pointed out that even if the homogeneous polarization is applied in the bulk crystal, there is a change of polarization happening from the bulk value to zero on the boundary (at the sample surface). This change can lead to a deformation.[60]

It should be noted that these abovementioned flexoelectric terms (the second right-hand-side terms of both Eq (2.3) and (2.4)) only consider the static bulk flexoelectricity contribution, which particularly involves in a situation where a strain gradient is stationary. This contribution is proportional to dielectric susceptibility. Thus, high-κ materials are thought to have large static bulk flexoelectric contributions.

The estimate of the flexoelectric tensor for this contribution was first proposed by Kogan.[67] In the estimation, he simply used a point-charge approximation with a lattice model containing point charges q (or e when considering an electronic charge) with an interatomic distance or a lattice parameter a. When these point charges are distorted, the strain gradient scales as $\frac{1}{a}$ and, for all dielectrics, the lower bound for the static bulk flexoelectric coefficient is approximately $\frac{e}{a}$, where e is the electronic charge.[68] This is roughly equivalent to a flexocoupling coefficient f of $\frac{q}{(4\pi\varepsilon_0 a)}$, or quantitatively 1-10V.[59]

(2) Dynamic Bulk flexoelectricity

In contrast to a static bulk flexoelectric, which is considered for the uniform static strain case, dynamic bulk flexoelectricity gives contributes when materials respond to a sound wave.[59] Dynamic bulk flexoelectric response basically describes a polarization and a strain gradient in response to an acoustic displacement.

The origin of the strain gradient in the dynamic case is distinctive from the static case. The strain gradient under the dynamic condition is generated by a sinusoidal wave of an elastic deformation with a wavelength greater than an interatomic distance. Figure 2.7 demonstrates the dynamic flexoelectric response. When the acoustic wave of inhomogeneous deformation propagates into a crystal, it generates a strain-gradient wave causing an atomic displacement $\delta_{d,}$ in addition to δ_s, a static strain-induced displacement, and a polarization wave with the amplitude proportional to the strain-gradient. In other words, while the inhomogeneity of lattice dispersion gives rise to static bulk flexoelectricity contribution, the frequency dispersion results in dynamic bulk flexoelectricity. Additionally, both the polarization and strain gradient waves are time-dependent.[59]

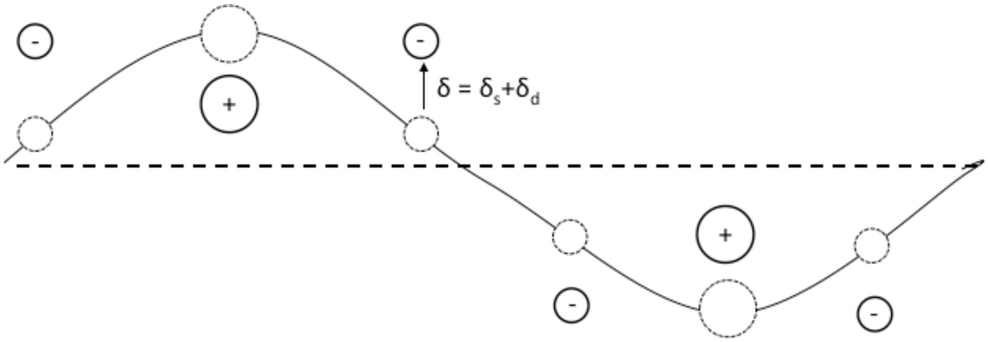

Figure 2.7: Dynamic bulk flexoelectricity in a moving medium. The resultant ionic displacement δ includes both a displacement from the static contribution δ_s and a displacement from the dynamic contribution δ_d (modified from Ref. 59).

This dynamic contribution is valid when the spatial scale is microscopic. It is based on lattice dynamics theory of ionic crystals, which can be considered as an extra term in the static response equation. If the dynamic response is added to the expression of static bulk flexoelectricity, the polarization response can be re-written as:

$$P_i = d_{ijk}\varepsilon_{jk} + (\mu_{ijkl} + \mu_d)\frac{\partial \varepsilon_{jk}}{\partial x_l} \tag{2.5}$$

where μ_d is the dynamic flexoelectric coefficient. The dynamic response is not only related to the acceleration of the medium, but also the masses of the ions in the crystal and can be given by Eq. (2.6):

$$\mu_d = -c_{ijkl}\chi\frac{M_{ij}}{\rho} \tag{2.6}$$

where c_{ijkl} denotes an elastic constant at a fixed electric field, ρ is a density and M_{ij} can be given as

$$M_{ij} = \delta_{ij} \frac{m_2 - m_1}{2Q} \tag{2.7}$$

with δ_{ij} is defined as the ionic contribution to the dielectric susceptibility of the crystal, and m_1 and m_2 are the masses of ions with opposite charges, Q.

Thus, the difference in ionic masses can lead to a dynamic bulk flexoelectricity contribution.[66] On the other hand, this contribution will vanish if the masses of all atoms have no difference or a crystal is made up from the same atoms. The anticipated magnitude of the flexoelectric dynamic response is ~ *M/e* or ~1 - 10 V, which is the same order of magnitude as static bulk flexoelectricity. It should be noted that the flexoelectric coefficients in both the static and dynamic response do not depend on frequency; however, the magnitude of the resultant polarization is frequency-dependent.[59]

(3) Surface piezoelectricity

For a finite sample, thin surface layers of non-piezoelectric materials can exhibit a piezoelectric behavior. The piezoelectric effect is induced by the presence of the free surfaces, which causes a distortion of the lattices adjacent to the surface. Such a distortion happens due to broken bonds at the surface. In other words, the atoms at the surface have fewer bonds than the ones in the bulk. The broken bonds result in a symmetry-breaking of the surface.

Fig. 2.8 depicts the mechanism of polarization-induced surface piezoelectricity. One could also relate the occurrence of broken bonds to surface stresses, which can extend to a few atomic layers from the surface. Such surface stresses lead to the relaxation of the surface associated with atomic displacements. In addition, the surface relaxation can result in an inhomogeneity of residual surface strain. Consequently, the inhomogeneously deformed surface layer can generate a polarization, resulting in an internal electric field. Ultimately, the surface of non-piezoelectrics can exhibit piezoelectricity known as the surface piezoelectric effect.

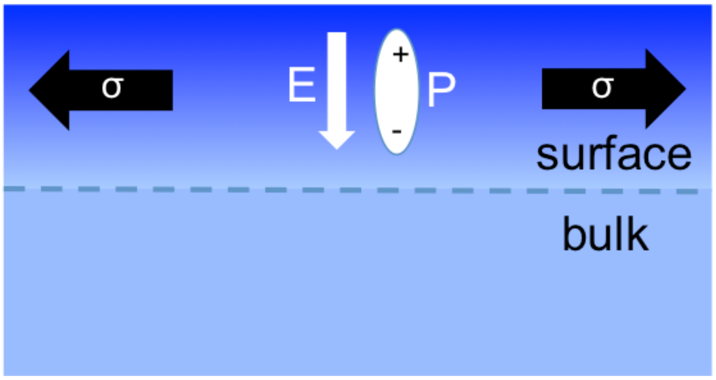

Figure 2.8. A stress induces a polarization near the surface causing the surface piezoelectric effect

In practice, the manifestation of surface piezoelectricity can be seen in bent or truncated pyramid samples.[62] Bending a plate or compressing a non-uniform geometry can create an inhomogeneous strain, which is a symmetry-breaking effect. The broken symmetry leads to a local dipole moment of the near-surface layers.

Consider a bent sample as an example, the surface layers exhibit a piezoelectric effect due to a gradient of the internal stress. Thus, the sample structure can be simply represented by a composite model comprised of 3 layers: two piezoelectric thin layers adjacent to the surface, with a thickness of λ, and a non-piezoelectric bulk layer, with a thickness of h, between the piezoelectric surface layers as illustrated in Fig. 2.9(a). The top layer has a tensile strain, while the bottom layer has a compressive strain. Such stresses induce polarization P_h with the same magnitude in the surface layers. However, due to the different directions of the stresses, the dipole moments on the opposite side of the sample have opposite signs at the surfaces. Specifically, the tensile layer contains a positive dipole moment at the surface, whereas the compressive layer contains a negative dipole moment at the surface. The induced polarizations also result in electric displacements in the sample indicated as a jump of the potential near the surface. However, the total electric displacements have to be conserved. Thus, to compensate the electric displacements in the surface layers, the presence of the polarization in the bulk layer is stimulated. The electric displacement profile along the cross-section of the sample is displayed in Fig. 2.9(b).

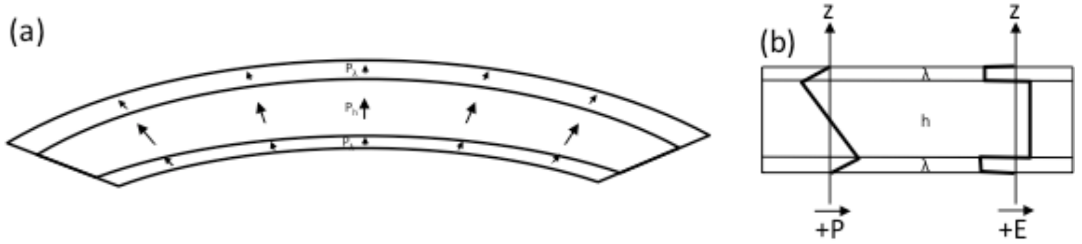

Figure 2.9. Surface piezoelectricity by the bending effect (duplicated from P. Zubko, 2013[59])

Similar to other contributions, the effective flexoelectric coefficient attributed to the surface piezoelectricity can also be calculated as Eq. (2.8):[69]

$$\mu_{13}^{eff} = e\lambda \frac{\varepsilon_f}{\varepsilon_\lambda} \tag{2.8}$$

when *e* is a piezoelectric modulus, λ is the surface thickness, ε_f is the bulk dielectric permittivity and $\varepsilon_\lambda = \varepsilon_0 + \chi_\lambda$; ε_0 is the dielectric constant of the free space and χ_λ is the dielectric susceptibility tensor of the piezoelectric surface layer.

According to the equation, the effect is not dependent of the ratio of surface to volume, but is sensitive to the dielectric constants of the piezoelectric surface layers ε_λ and of the bulk ε_f.[59] As a result, the flexoelectric coefficient for this contribution is relatively high in high-K materials. Tagantsev[70] evaluated the magnitude of this contribution by setting e = 1 C m^2 and $\frac{\varepsilon_f}{\varepsilon_\lambda}$ = 10, and thus obtained the effective flexoelectric coefficient of 1–10 V, showing it to be as significant as the bulk flexoelectricity. It is also worth mentioning that the magnitude of this contribution is influenced by crystal orientations. It is known that the piezoelectric constant of thin layers strongly depends on the surface structure.[70] Therefore, different surfaces of a polycrystalline crystal may have varied magnitudes of surface piezoelectricity.

(4) Surface flexoelectricity

Similar to the bulk flexoelectricity, surface flexoelectricity is a polarization response to a strain gradient; however, the effect is considered only in the near-surface layers of a finite sample. Additionally, surface flexoelectrcity, analogous to surface piezoelectricity, is strongly influenced by surface properties, such as surface structures and compositions. Despite the similarity, the difference from surface piezoelectricity is that this contribution is dependent on the ratio of surface to volume. In addition, this effect is not sensitive to the dielectric permittivity. In other words, the surface flexoelectric coefficient is not enhanced in high-K materials. As a result, this contribution is relatively small and may be negligible in ferroelectrics, compared with the other contributions.[64]

Using a simple model of a point-charge approximation, this contribution can be calculated using Eq. (2.9) describing the induced dipole-moment density as followed:

$$\delta P_i^{SF} = I\left(2\frac{\partial u_{ij}}{\partial x_j} - \frac{\partial u_{jj}}{\partial x_i}\right) \tag{2.9}$$

where **I** is a trace of a multipole electric moment tensor and $\frac{\partial u}{\partial x}$ is a strain gradient tensor corresponding to the direction of the vector *x*. From the definition of **I**, surface flexoelectricity is especially sensitive to the electronic structure of the surface.[70]

To estimate the magnitude of this effect in ordinary solids, it is assumed that the flexoelectric coefficient *f* ~ *I*. The estimate of *I* is approximately *e/a*. As a result, in ordinary dielectrics, this contribution has about the same order of magnitude as the others.[66] It should be noted that this is true for only ordinary solids. This contribution is relatively small in high-*K* materials.

In conclusion, these four mechanisms with different physical origins can contribute to the flexoelectric effect. For a finite crystal, in the case of a static strain gradient, static bulk flexoelectricity, surface piezoelectricity and surface flexoelectricity contribute to the flexoelectric effect. In the case that the sample responds to acoustic excitation, only two contributions from static bulk flexoelectricity and dynamic bulk flexoelectricity are considered. In principle, all contributions exhibit about the same order of magnitude.[59,70]

2.2.2 Flexoelectricity vs Piezoelectricity: similarities and differences

The analogy of the flexoelectric effect is close to that of the piezoelectric effect. Similar to piezoelectricity, flexoelectricity is an electromechanical coupling. Besides this similarity, the key differences that distinguish flexoelectricity from piezoelectricity are described as follows[25].

(1) Origin of the effect

The central dissimilarity is the cause of the effect. The flexoelectric effect originates from a strain gradient, while the piezoelectric effect is caused by a uniform strain or homogeneous deformation. Such a strain gradient can break the inversion symmetry of a material, which is a crucial requirement that leads it to appear like piezoelectricity in non-centrosymmetric materials. Specifically, the symmetry-breaking effect, which results from atomic displacements, can induce a polarization in centrosymmetric crystals. Figure 2.10 demonstrates this difference between piezoelectricity and flexoelectricity. In piezoelectric materials (Fig. 2.10(a)), the crystal is non-centrosymmetric, so upon the application of an external stress, a central atom is shifted leading to a net dipole moment in the crystal. By contrast, in centrosymmetric materials, a uniform strain generates equal atomic displacements in the structure, which results in a zero net dipole moment. To induce a polarization, the symmetry needs to be broken by a strain gradient. Thus, upon inhomogeneous deformation as illustrated in Fig. 2.10(b), such as under a bending scenario, the net dipole moment is non-zero. One may refer flexoelectricity induced by this bending effect as a contribution of surface piezoelectricity.[59]

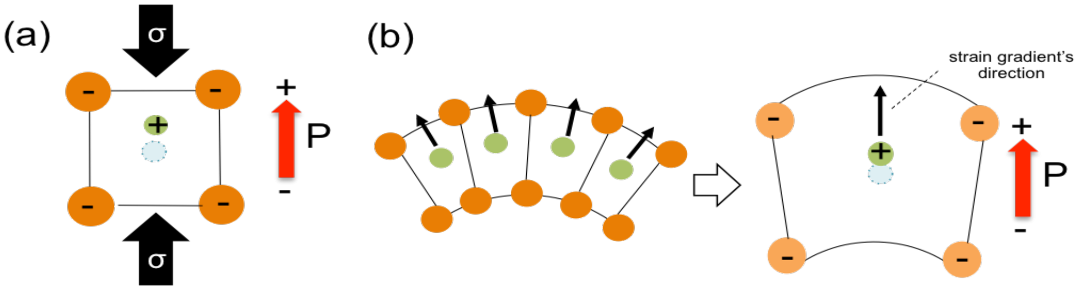

Figure 2.10. The difference of the symmetry consideration between (a) piezoelectricity and (b) flexoelectricity

In addition, even though piezoelectricity and flexoelectricity are both tensors, the orders of the tensors are different. On one hand, piezoelectricity is a third rank tensor, and thus it is restricted by a crystallographic consideration: only 20 noncentrosymmetric crystalline point groups can exhibit this effect. On the other hand, the tensor of flexoelectricity is fourth-order, so any materials can display the flexoelectric effect regardless of the symmetry. [59,71]

(2) Direct and Converse effect

The symmetry between the direct and converse effects in flexoelectricity differs from the one in piezoelectricity. In piezoelectric materials, the direct and converse effects are symmetric. When no electric field is applied ($E = 0$), a strain can induce a polarization. This phenomenon validates the occurrence of the direct piezoelectric effect. Moreover, the converse piezoelectric effect is also possible: in a mechanically free sample, an electric field can induce a stress. In contrast to piezoelectricity, flexoelectricity has asymmetry between the direct and converse effects. Specifically, under the absence of electric field, a strain gradient can induce a polarization; however, for the converse flexoelectric effect, a polarization cannot generate a strain gradient.[70]

(3) Dynamic bulk flexoelectricity

In an oscillating medium, an additional term for dynamic bulk flexoelectricity can be incorporated into bulk flexoelectricity. Thus, a dynamic flexoelectric coefficient is included in the equation of static bulk flexoelectrcity to express this contribution. As a result, in the case of flexoelectricity, the expressions of a polarization response to a strain gradient under static and dynamic situations are different. In other words, the proportionality factor between a polarization and a strain gradient in the dynamic contribution are distinctive from the one in the static contribution. However, this contribution to the dynamic bulk response doesn't exist in piezoelectricity. Specifically, the relations of the polarization and strain under static and dynamic situations are identical. Thus, the dynamic bulk effect differentiates flexoelectricity from piezoelectricity.

(4) Surface contributions

In general, the surface contributions are proportional to the surface to volume ratio. Thus, they are negligible in bulk materials. However, in the case of a finite sample, the surface contributions can have a strong impact to flexoelectricity. The presence of the surface can cause exceptional effects, such as an atomic polarization due to a local symmetry-breaking or surface relaxation. Moreover, as the flexoelectric effect is size-dependent, a very thin layer near the surface (~ few atomic layers equivalent to a few angstroms) can exhibit pronounced flexoelectricity if the total size of the crystal is small in comparison. The surface contributions in flexoelectricity can be classified into two mechanisms: (1) surface piezoelectricity and (2) surface flexoelectricity.

For the first mechanism of the surface contributions: surface piezoelectricity, thin surface layers of non-piezoelectric materials exhibit a piezoelectric behavior, which is induced by a distortion of lattices adjacent to the surface. Such a distortion arises due to the broken bonds at the surface. In other words, the atoms at the surface have fewer bonds than the ones in the bulk, and this also causes asymmetry of strains of surface atoms.

In the case of surface flexoelectricity, the effect is associated with a trace of quadrupolar electric moments. Surface flexoelectricity is strongly influenced by surface characteristics, such as surface charges and structures. When stresses or strains are generated in the surface layer, the surface charges are redistributed, which can lead to a linear coupling between a polarization and a strain gradient within a few layers from the outermost surface. It should also be noted that the effect is independent to dielectric permittivity. Thus, the effect is not supposed to exhibit differently in different-*K* materials.

While flexoelectricity has surface contributions, piezoelectricity is a bulk property. In other words, the change in surface properties does not significantly affect the piezoelectric effect. As a result, the surface contributions are usually neglected in piezoelectricity because of the relatively small magnitude.

2.2.3 Theoretical and experimental studies

To gain a better understanding of the significance of the flexoelectric effect in materials, estimates of flexoelectricity is essential. The estimates are also useful for quantitative comparisons. To evaluate the flexoelectric effect in ordinary dielectric materials, many computational models having been developed. Most of them are typically based on microscopic approaches. Such techniques, for example, include ab-initio calculations, first-principle calculations and Monte Carlo simulations.[59,72,73]

Flexoelecric coefficients of most materials are not readily available. The first calculation of flexoelectricity was made by Kogan.[67] A simple rigid-ion model of periodic lattices with interatomic spacing *a* was used. From this approximation, the typical values of the flexocoupling coefficients in dielectrics were quantified to be in a range of 1-10 V. Because of the simplicity of the approximation, later more complicated models based on Kogan's have been developed to improve the accuracy.

Nevertheless, all computational methods cannot address all contributions or have some limitations. For instance, Ponomareva *et al.*[74] proposed an approach based on an ab-initio integrated Monte Carlo simulation. This method can used to calculate flexoelectric and flexocoupling tensors of ferroelectric films; however, the model is short of the bulk effect consideration because the simulation was considered under a unit-cell environment and this leads to the inappropriate approximation for a larger scale, such as in macroscopic scale.

The accuracy of modeling is a crucial issue in flexoelectricity calculations. Studies using different numerical techniques reveal controversial predictions of the flexoelectrcity estimates. Hypothetically, some studies pointed out that the differences of the computational results arose because different contributions were considered in simulations. Not only are there disagreements between the calculated estimates using different techniques, the variations between the calculated and measured values are also found. The previous studies revealed that the flexoelectric coefficient from the experiment is much larger than the theoretical or calculated ones. This may be caused by the fact that many factors can contribute in the experimental response and some theoretical approaches didn't consider all the contributions, namely bulk flexoelectricity, surface piezoelectricity and surface flexoelectricity.[59,68]

In addition to the theoretical approximations, experimental investigations of the flexoelectric effect are essential to validate the fidelity of the calculations. Two experimental techniques are mainly used to evaluate flexoelectricity: (1) a phonon spectra and (2) macroscopic investigations.[59] These two methods can examine different contributions of flexoelectricity.

Specifically, the static and dynamic bulk flexoelectric effects are obtained from phonon spectra analyses, while the contribution of static bulk flexoelectricity and surface piezoelectricity are yielded via macroscopic analyses.

The former method uses a neutron scattering technique to measure the long-wavelength low energy phonon spectrum.[75] Transverse acoustic phonons propagate into a crystal and then result in a spectrum of inelastic scattering or Brillouin scattering. Such a spectrum is examined based on the continuum Landau-theory to determine the interaction between the optical soft mode and the acoustic mode. A comparison between the obtained spectrum and the predicted equation of flexoelectricity is made to determine the flexoelectric tensor. The major disadvantage of this technique is that some key information, such as the sign of the effect, cannot be acquired.

Besides the phonon spectrum analysis, macroscopic analyses are also widely used. The common techniques used in this particular measurement are: (1) bending a beam sample and (2) compressing a truncated pyramidal sample.[59,62] Basically, the bending method generates a transverse strain gradient in a beam or cantilever sample. Such a strain gradient also generates a polarization response, which can be measured in a form of current signal through the sample. In case of the pyramid-shaped compression, a force is applied on the surface of the sample. Due to different cross-sectional areas of the truncated pyramid, a strain gradient is created. Unlike the bending method, the compression method gives rise to a longitudinal strain gradient. Additionally, the compression setting can acquire the converse flexoelectricity measurement by applying a voltage across the sample. The application of the voltage results in a creation of an inhomogeneous polarization response, which can induce a strain in the sample.

The experimental measurements also have restrictions and face a challenge of quantifying the analysis to get an accurate measurement. For example, using the bending method, the three components cannot be all obtained. Thus, to yield the estimates for all components, an additional technique is needed. Moreover, the flexoelectric estimates obtained from experiment studies are significantly deviated from the simulated prediction. Typically, the experimental values are greater about two or three orders of magnitude. So far, the explanation behind the mismatch of the calculated and measured values is still mysterious, but it is possible that the difference occurs because all contributions are not incorporated into the simulations. As a result, the calculation result may be valid in only some certain systems. Also, another challenge that experimental studies face is to isolate the measured response from all contributions. The measured response usually included all possible mechanisms, so it is difficult to quantify the magnitude of just one contributor.

Due to many contributions, theoretical and experimental studies for flexoelectricity are challenging. Additionally, the comprehensive explanation for the effect is still ambiguous. Thus, models and experimental techniques that can give more accurate estimates and validate the postulations are in need.

2.2.4. Other manifestations of the flexoelectric effect

(1) Manifestations in domain structures

In the literature related to flexoelectricity, most domain structures refer to ferroelectric domains. Flexoelectricity can significantly alter the ferroelectric effect in ferroelectric materials, especially for thin film structures. Flexoelectricity-induced internal field enhances the magnitude of the polarization in ferroelectric materials.[61,76] Interestingly, flexoelectricity not only can affect the magnitude, but also influence the formation of ferroelectric domains.[61,76–78] Specifically, it can change domain configuration which alters the alignment of the field. By mechanically modulating a magnitude of a strain gradient, an increased flexoelectricity can alter the rotation of the spontaneous polarization.[77,78] Even though a mechanical deformation can cause a piezoelectricity-induced polarization, the domain-switching mechanism of ferroelectric thin films is manipulated by a flexoelectricity-induced polarization.[78] This indicates that the flexoelectric contribution to domain-switching overwhelms other contributions, such as piezoelectricity.

(2) Manifestations of polar behaviors in centrosymmetric materials

Typically, polar behaviors are restricted by crystal structures, specifically, only exhibited in non-centrosymmetric materials. However, polar behaviors can be induced in centrosymmetric materials by flexoelectricity. For example, anomalously polar states were found at grain boundaries of ferroelastic $CaTiO_3$.[79,80] In particular to $CaTiO_3$, a large strain gradient is generated by the lattice distortion. Such a strain gradient breaks the symmetry and leads to a ferroelectric polarization at the interface where the structural distortion occurs (in principle, this could be twin walls, interface and surface). Similarly, the polar nature was also found in paraelectric $SrTiO_3$. However, in contrast to $CaTiO_3$ in which the wall polarity is induced by structural distortion, the polarity in $SrTiO_3$ is induced by temperature.[81]

The significance of anomalously polar behaviors in centrosymmetric materials is a possibility to develop multifunctional materials and also to broaden choices of materials for piezoelectric- or ferroelectric- related applications.[82] This also leads to numerous interests to quantify this effect as well as to explore investigations in non-piezoelectric materials where I can engineer materials properties in many potential applications, such as nano-generators.[30]

2.3 Bismuth Vanadate ($BiVO_4$)

2.3.1 Structure

Bismuth vanadate exhibits three main phases: tetragonal zircon, tetragonal scheelite and monoclinic fergusonite (which is often called monoclinic scheelite).[83,84]All phases can be isolated in the bulk through variations in the synthesis techniques, such as solid-state reaction, the sol-gel method and the hydrothermal route.[84] Fig. 2.11 schematically describes all possible transformations of $BiVO_4$. Tetragonal zircon structure can be obtained through low-temperature processes. This structure possesses a space group of $\mathbf{I}4_1/\mathbf{a}$ with a = b = 7.303 Å and c = 6.584 Å.[85,86] Monoclinic fergusonite $BiVO_4$ is usually obtained from high-temperature processes, such as solid-state syntheses. By heating up to 397-497 °C and then cooling down to room temperature, the tetragonal zircon phase irreversibly becomes the monoclinic fergusonite phase. The monoclinic fergusonite structure (ferroelastic) can also transform to tetragonal scheelite (paraelastic) via a ferroelastic transition at 255°C. This paraelastic-to-ferroelastic transition is reversible and belongs to a group of 4/mF2/m.[86] The monoclinic fergusonite belong to a space group of $\mathbf{I}2/\mathbf{b}$ with $\mathbf{a}$ = 5.1935 Å, $\mathbf{b}$ = 5.0898 Å, $\mathbf{c}$ = 11.6972 Å, and γ = 90.3871° (or a complementary angle of 89.613°), while the tetragonal scheelite belongs to a space group of $I4_1/a$ with $\mathbf{a}$ = $\mathbf{b}$ = 5.1470 Å, $\mathbf{c}$ = 11.7216.[87] It should be noted that the abovementioned monoclinic setting defines 2_1 along [001], which is a convenient way to compare parameters directly to tetragonal scheelite; however, such indices of the monoclinic $BiVO_4$ structure are non-conventional. The standard convention has the b-axis as the longest axis and identifies as the C-centered structure (C2/c) with lattice parameters **a'** = 7.223, **b'** =11.702, **c'** =5.170, and β' = 134.23°.[85] However, in this study, the convention of **I**2/**b** is used to correspond to the parameters of tetragonal scheelite, which is used for OIM analysis. The structural conversion between the non-conventional and standard convention of monoclinic $BiVO_4$ is depicted in Fig. 2.12.

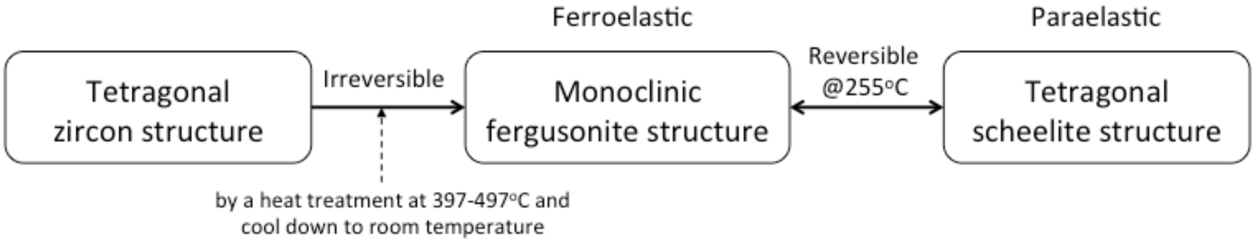

Figure 2.11. Phase transformation in $BiVO_4$ (modified from Ref. 83)

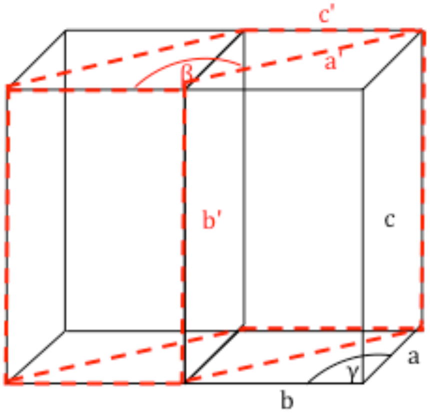

Figure 2.12. Structural conversion of $BiVO_4$
(black = non-conventional I-centered structure, red = modern C-centered structure)
(modified from Ref. 85)

Fig 2.13 shows the scheelite structure of $BiVO_4$. The structures of monoclinic fergusonite and tetragonal scheelite are comparable. In fact, monoclinic fergusonite can be considered as a distorted structure of tetragonal scheelite. Both structures are composed of four-coordinated V atoms forming a tetrahedron of VO_4 and eight-coordinated Bi atoms surrounded by O atoms. The isolated VO_4 tetrahedron has $\bar{4}2m$ symmetry and is aligned along the $\bar{4}$ axis. A Bi atom forms a dodehedron of BO_8 and is located at the middle of eight VO_4 tetrahedra.[86] In case of tetragonal zircon, V and O atoms have the same coordination as that in the scheelite structure. However, Bi atoms are connected with six VO_4 tetrahedra instead of eight VO_4 tetrahedra in the scheelite structure.

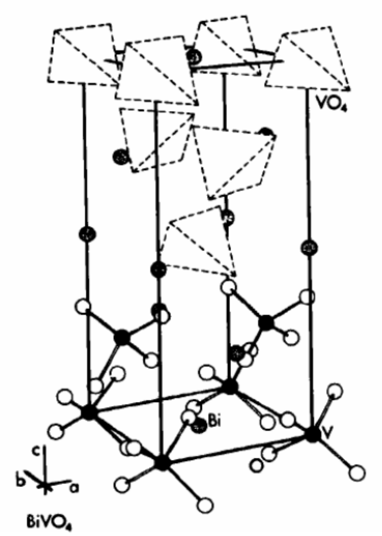

Figure 2.13. Scheelite structured $BiVO_4$.[86]

Even though the atom arrangements in monoclinic fergusonite and tetragonal scheelite are very similar, the significant difference of the structures is the distorted environment of V and Bi atoms. The structural environment in each structure is illustrated in Fig. 2.14. The local environments in tetragonal zircon (Fig. 2.14(a)) and tetragonal scheelite (Fig. 2.14(b)) are undistorted. In other word, the bond lengths of polyhedrons in these two structures are symmetrical. Conversely, in monoclinic fergusonite (Fig. 2.14(c)), the displacements of V and Bi atoms vanish the locally symmetry and also lead to a structural distortion. The distortion results in a symmetry reduction of monoclinic fergusonite by losing symmetry elements of $\bar{4}$ and 4_1 in tetragonal scheelite.

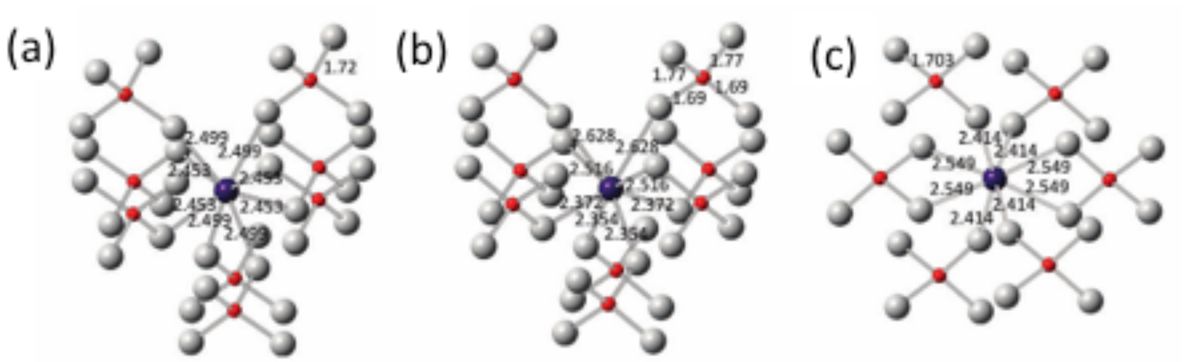

Figure 2.14. The bond lengths of (a) tetragonal scheelite, (b) monoclinic scheelite and (c) tetragonal zircon [85]

2.3.2 Ferroelastic transition in $BiVO_4$

$BiVO_4$ possesses a ferroelastic transition between monoclinic fergusonite (ferroelastic) and tetragonal scheelite (paraelastic) at 255°C. Monoclinic fergusonite stably exists at room temperature. This structural change is described as a displacive transition, which is driven by spontaneous strain. Conclusively, the major structural changes leading to the transition are listed below.

(1) The atoms on (001) shift along the [001] direction and the directions of the displacements are alternating as illustrated in Fig. 2.15.

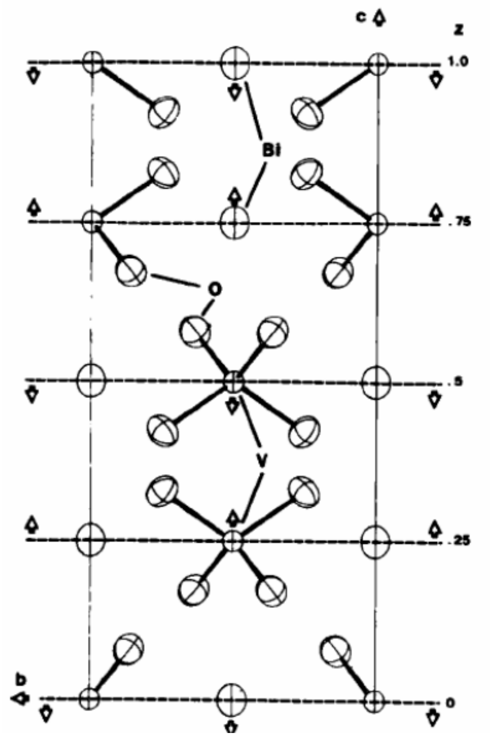

Figure 2.15. Schematic illustration of the displacements leading to the structural distortion in monoclinic $BiVO_4$.[86]

(2) Among all displacements, Bi atoms have the largest. The displacement of atoms in the structure is summarized in Table 2.1.

Table 2.1: The atomic displacements in monoclinic BiVO4.[35]

	Δ_{xy}	Δ_z	$\lvert\Delta\rvert$
Bi	0.039	-0.207	0.21
V	0.039	-0.06	0.07
O1	0.125	-0.111	0.168
O2	-0.125	0.111	0.168

Note: Δ_{xy} and Δ_z is a diaplacement in the (001) plane, and along the z-axis, respectively. $\lvert\Delta\rvert$ represents the total displacement.

Overall, the ferroelastic switching process occurs on the 4_1 axis and during the transition, the parameter *a* shortens, while *b* increases. The summarized changes in the parameters are demonstrated in Fig. 2.16.

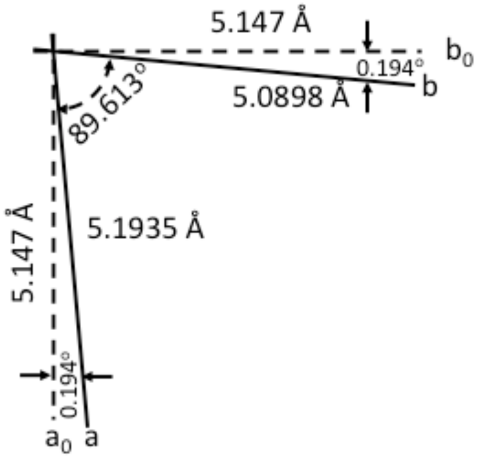

Figure 2.16. The changes in the structural parameters of tetragonal scheelite (with parameters on the a_o and b_o axes) to monoclinic fergusonite (with parameters on the a and b axes which are rotated with respect to the a_o and b_o axes). (modified from Ref. 87)

Domain structure is commonly observed in ferroic materials, including ferroelastics. Ferroelastic domains are formed as a consequence of a reduction of symmetry. In $BiVO_4$, during the transition, the symmetry elements of $\bar{4}$ and 4_1 are lost. The ratio of the order of the point group in high symmetry structure and that in low symmetry group equals the number of orientation states (permissible domains) that can exist in the system. As a result, in the $BiVO_4$ system, two orientation variants can exist. In other words, these two domain states are energetically equivalent. These variants are rotated ~90° around the c axis across domain boundary. In ferroelastic materials, according to Sapriel's classification, domain walls can be classified into two types: W wall and W' wall. W wall is restricted by symmetry and W' wall is determined by strains.[88] Fig. 2.17 schematically illustrates unit cell alignments across W and W' walls (please note that the defined axes of twin domains are different across domain wall.) Lim *et al.* [89] reported the calculated and experimental values of orientations of W' and W walls in $BiVO_4$ which are summarized in Table 2.2 and 2.3, respectively.

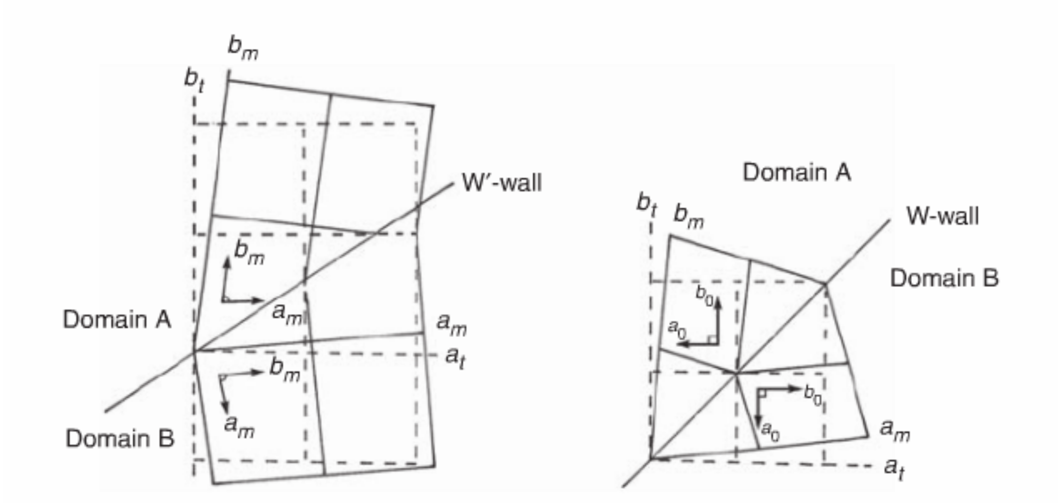

Figure 2.17. W' and W wall in ferroelastic $BiVO_4$.[137]

Table 2.2. The values of the W' wall orientation with respect to the a-axis in monoclinic $BiVO_4$ from the calculation and from the measurements using various techniques[89]

Reference	θ observation (degree)	θ calculation (degree)	Experimental method
1. Sawada A. & Ishibashi Y., 1979	39		Polarizing microscope
2. Manolih C. & Amelinckx S., 1980	32	31.4	TEM, Electron diffraction
3. Wainer L. S. et al., 1981	37.4	36	TEM, Electron diffraction

Ref: 1. Sawada, A. and Ishibashi, Y., *Kotai Butsuri* **14**, 464 (1979).
2. Manolikas, C. and Amelinckx, S., *Phys. Status Solidi a* **60**, 167 (1980).
3. Wainer, L. S. et al., *Ferroelectrics* **31**, 121 (1981).

Table 2.3. The values of the W wall orientation with respect to the a-axis in monoclinic $BiVO_4$ from the calculation and from the measurements using various techniques[89]

Reference	$\theta_{\text{observation}}$ (degree)	$\theta_{\text{calculation}}$ (degree)	Experimental method
1. Moon E. Y. et al., 1987	44.25		X-ray diffraction, ^{51}V NMR
2. Lim A. R. et al., 1989		45	
3. Lim A. R. et al., 1990	44		^{51}V NMR, polarizing microscope
4. Lim A. R. et al., 1992	44		TEM, electron diffraction
5. Yeom T. H. et al., 1994	44.2		Mn^{2+} EPR
6. Lim A. R. et al., 1995	44.25		^{209}Bi NMR

Ref:
1. Moon, E. Y. et al., *J. Phys. C: Solid State Phys*. **20**, 1867 (1987).
2. Lim, A. R. et al., *J. Phys.: Condens. Matter* **1**, 1571 (1989).
3. Lim, A. R. et al., *J. Korean Phys. Soc.* **23**, 162 (1990).
4. Lim, A. R. et al., *Solid State Commun*. **83**, 185 (1992).
5. Yeom, T. H. et al., *J. Phys.: Condens. Matter* **6,** 383 (1994).
6. Lim, A. R. et al., J. Phys.: Condens. Matter **7**, 7309 (1995).

The predicted and the measured values of the orientations of the W' domain walls are inconsistent. The values are in the range of 36° -39° with respect to the a-axis. Because W' walls is controlled by spontaneous strain, the deviation may arise from the variation of the magnitude of the strain. Despite the variation of wall orientations, all walls are aligned with an acute angle with respect to the a-axis. The angle of W' wall corresponds to the plane of (1**p**0), where

p≈0.78. On the other hand, the alignments of the W wall from many observations and calculations seem to agree due to its symmetry restriction. Specifically, the W wall is rotated ~44° with respect to the a-axis which corresponds to (110) plane. It is important to note that two sets of the permissible orientations of domain walls are about perpendicular, specifically 91+/-0.5° to each other.[88] Typically, domains need to compatibly align to minimize strain energy. Specifically, each domain state needs to rotate with the same angle to be in mutual contact. Plus, the rotation should be in the opposite direction. Regarding compatibility, two types of domain are classified: (1) full-strain compatible and (2) incompatible. The former type forms a parallel alignment of domain walls, while the latter one comprises of sets of quasi-perpendicular domain walls.

The elastic tensor of the spontaneous strain can be predicted using lattice parameters of tetragonal and monoclinic structures. The tensor can be calculated using the following equation:[90]

$$\varepsilon_{ij}^{s}(S_1) = \begin{bmatrix} -\varepsilon_{11}^{s} & \varepsilon_{12}^{s} & 0 \\ \varepsilon_{12}^{s} & \varepsilon_{11}^{s} & 0 \\ 0 & 0 & 0 \end{bmatrix} = \begin{bmatrix} (\varepsilon_{11} - \varepsilon_{22})/2 & \varepsilon_{12} & 0 \\ \varepsilon_{12} & -(\varepsilon_{11} - \varepsilon_{22})/2 & 0 \\ 0 & 0 & 0 \end{bmatrix}$$

where (S$_1$) indicates a single ferroelastic orientation state, $\varepsilon_{11}, \varepsilon_{22}$ and ε_{12} are lattice strain related to the structural changes and can be computed by

$$\varepsilon_{11}(T) = (a_m(T) - a_t(T))/a_m(T)$$

$$\varepsilon_{22}(T) = (b_m(T) - b_t(T))/b_m(T)$$

$$\varepsilon_{12}(T) = \tan\left[\frac{\gamma_m - 90^o}{2}\right]$$

and the magnitude of the spontaneous strain is equal to $[2(\varepsilon_{11}^{s})^2 + 2(\varepsilon_{12}^{s})^2]^{1/2}$. Fig. 2.18 shows the temperature-dependent spontaneous strain.

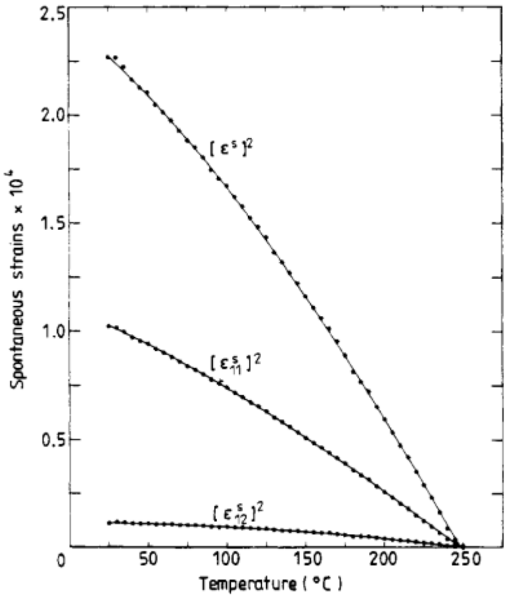

Figure 2.18. Temperature-dependent spontaneous strain[91]

Based on the lattice parameter defined by Sleight *et al.*[87] (**a**$_m$ = 5.1935 Å, **b**$_m$ = 5.0898 Å, **c**$_m$ = 11.6972 Å, and γ_m = 89.613° and **a**$_t$ = **b**$_t$ = 5.1470 Å, **c**$_t$ = 11.7216). The obtained ε_{11}^{s} and ε_{12}^{s} are $10.07\text{x}10^{-3}$ and $-3.38\text{x}10^{-3}$ respectively, which causes a spontaneous strain with the magnitude of $15.02\text{x}10^{-3}$. This strain tensor also describes the distortion of $BiVO_4$ monoclinic structure and anisotropy of the spontaneous strain; for example, the longitudinal strain is larger than the transverse (shear) strain.

In addition to strain, temperatures and rates can influence domain formation. In general, the formation of domain walls starts at high local stress area and then propagates. The propagation rate depends on temperature and heating rate. For example, if either temperature is below 235°C or heating rate is low (~1°C/min), domain walls will propagate slowly with the approximate rate of 0.2 mm/s. The occurrence of domain walls is also influenced by temperatures.[91] Quasi-perpendicular domain walls do not appear until temperature reaches 239°C. Considered the influence of temperature and rate, the orientation of domain walls may be reproducible during re-annealing processes if the annealing parameters remain the same.

2.3.3 Photocatalytic properties of $BiVO_4$

Crystal structure strongly influences photocatalytic properties of materials. In particular to $BiVO_4$ phases, Kudo *et al.*[92] reported that fergusonite shows the highest catalytic activity among all three possible structures. The higher photocatalytic performance of monoclinic fergusonite over tetragonal zircon could be due to the band gaps. The band gaps of monoclinic and tetragonal zircon are 2.4 and 2.9 eV, respectively.[93] Thus, with the smaller band gap, the monoclinic phase would be expected to have higher photocatalytic activity.

In the case of monoclinic fergusonite and tetragonal scheelite whose structures are almost identical, the band gaps are just slightly different (2.41 eV for monoclinic and 2.34 eV for tetragonal).[94] Despite the smaller band gap of tetragonal scheelite, monoclinic fergusonite still obtain higher photocatalytic activity. Fig. 2.19 shows the photocatalytic activity obtained from monoclinic (a line denoted with a) and tetragonal (a line denoted with b) phases under visible light (i) and UV light (ii) iraadiation. It is conclusive that monoclinic has a better performance in both visible-light and UV light regions.

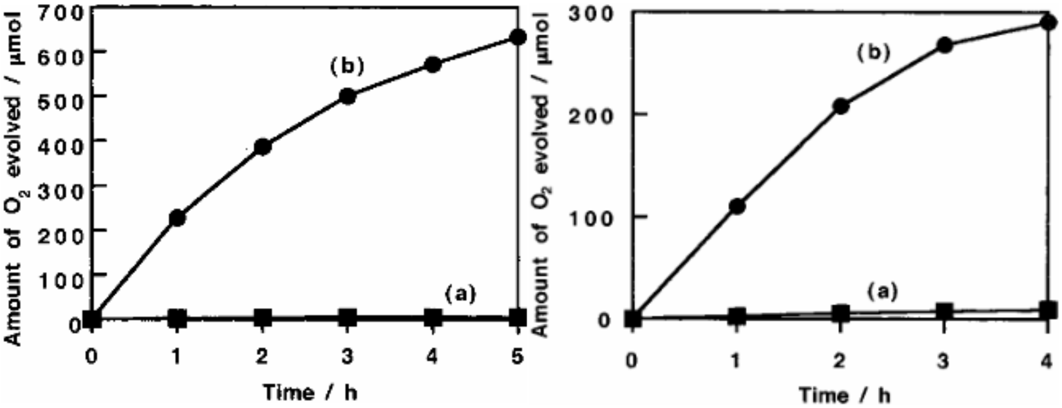

Figure 2.19. The comparison of the photocatalytic performance of (a) scheelite and (b) monoclinic in visible light (left) and UV light (right)[94]

The main reason for higher reactivity in monoclinic phase is because of the distortion of the structure. The distortion of each atom in the monoclinic fergusonite structure is summarized in Table 2.1. Overall, the considerable distortion belongs to a Bi site in a Bi-O polyhedron. The distortion happens due to two main factors: (1) asymmetry of the bond lengths[86] and (2) the electron lone pairs of Bi atoms.[95] The distortion could promote the charge separation as well as the delocalization of charge carrier. Similarly, Tokunaga *et al.*[94] pointed out that the enhanced photocatalytic performance in monoclinic could be resulted from the variations of the local structure. Such variations can affect electron transport in the structure. For example, the distortion can induce a local polarization that can increase a charge separation leading to the high photocatalytic activity.

Additionally, the variation of the local structures can alter the electronic structure affecting the photocatalytic properties of monoclinic $BiVO_4$. Walsh *et al.*[22] simulated the band structure of monoclinic $BiVO_4$ and found that the Bi 6s state and the O 2p state in the valence band was hybridized, which does not exist in the tetragonal phase. This hybridization can control the valence band edge position and the carrier transport. The calculation of the band structure by Walsh *et al.* is in agreement with the experimental studies by Kudo *et al.*[93] and Payne *et al.*[96]

They also emphasized the role of Bi 6s lone pair electrons to increase the activity. Explicitly, the lone pair electrons alter the isotropic optical properties in tetragonal to become anisotropic.[97]

Chapter 3

METHODOLOGY

This chapter explains the sample preparation method and characterization techniques used in the study. In this research, $BiVO_4$ with different compositions was synthesized via a solid solution and solid-state reaction route: the details of the processes are provided in this chapter. Also, the details of all characterization techniques are described. These techniques include X-ray diffraction, photochemical experiments, electron backscatter diffraction (EBSD), atomic force microscopy (AFM), piezoresponse force microscopy (PFM), and electrical conductivity measurement.

3.1 Sample preparation

Monoclinic ($x = 0$ and 0.05) and tetragonal ($x = 0.175$) phases of $Na_{0.5x}Bi_{1-0.5x}Mo_xV_{1-x}O_4$ powders used in this research were synthesized by a conventional solid-state reaction route.[31] These compositions were chosen based on the previous study of Zhou *et al*.[31] and aim to attain the targeted monoclinic and tetragonal structures with $x = 0$ and 0.05, and $x = 0.175$, respectively.

Initially, stoichiometric ratios of the starting materials (Bi_2O_3 (99.9999% purity, Acros organic), V_2O_5 (99.999% purity, Alfa Aesar), $NaCO_3$ (99.5%, Acros organic), and MoO_3 (≥99.5%, Sigma-Aldrich)) were mixed. The mixture was ball-milled overnight using yttria stabilized zirconia grinding media and ethanol as a dispersant. After ball milling, the mixture was dried at 85 °C and then heated to 650 °C in air for 3 hours to complete the reaction.[98] The reacted powder was then manually ground to reduce the particle size. The calcined powders were characterized by X-ray diffraction to confirm full reaction to the targeted structures.

Next, the powder was sintered to form a dense ceramic. Prior to sintering, 1g of fine calcined powder was mixed with a few drops of 5 wt% of PVA binder in ethanol and pressed into a 1 cm-diameter cylindrical-shaped pellet using a hydraulic press with a uniaxial pressure of 6 metric tons. The green pellets were heated at 500 °C for couple hours, to remove the added PVA, then underwent a sintering step. The optimal sintering temperatures were found by trial and error. The undoped samples were annealed at 600°C, while the co-doped samples were annealed at 780 °C. All samples were annealed for 20 hours. The heating and cooling processes were set to have the same rate of 5 °C/min. All of the heat treatments were carried out in an alumina crucible with an air atmosphere. Note that, at the sintering step, to minimize contamination and reduce a loss from volatile components, excess reacted powder was placed on the bottom and the top of the pellets.

The sintered samples were mechanically lapped and polished. The samples were first lapped using SiC grinding papers to get a flat surface, followed by polishing with successively finer Al_2O_3 polishing suspensions (consecutively 1 μm, 0.3 μm and 0.05 μm) on a polishing cloth until mirror-like surfaces were obtained. Afterwards, the samples were annealed at 300 °C for 2 hours to heal surface damage from the polishing at a temperature above the ferroelastic transition temperature.[99] After preparation, the samples were characterized by X-ray diffraction and EBSD (described below). These steps resulted in (essentially) single-phase polycrystalline pellets having the targeted symmetry with a random orientation texture. These samples were used to determine the relationship between photochemical reactivity and orientation.

3.2. Characterization techniques

3.2.1. X-ray diffraction

X-ray diffraction was used to identify the phases of the synthesized powders, the sintered pellets, and the annealed samples. Besides the identified phase, the crystallographic structure and orientation were also obtained.[100]

The XRD analysis was performed using Panalytical X'Pert Pro MPD diffractometer. CuK**α** (lambda = 1.5406 **Å**) radiation with no filter was used as the incident beam. The accelerating voltage and the operating beam current were set to be 45 kV and 45 mA, respectively. The scans were run over a 15°-90° range of the incident angle (2θ) at a scan rate of 3°/min with a step size of 0.05°. Based on Bragg's law ($2d\sin\theta = n\lambda$), diffracted peaks are detected when lattice planes with a particular *d*-spacing are oriented with an angle of θ with respect to the beam. Thus, the diffraction pattern of a material is unique and can be used to determine the phase and the structure.[101] The diffraction pattern was first collected from the powder after the synthesis to confirm that the reaction was complete and no impurity phases were present. The phases of the samples after sintering and annealing were also examined to demonstrate that the desired phases remained.

3.2.2. Electron backscatter diffraction

Electron backscatter diffraction (EBSD) analysis was carried out using a Quanta 200 scanning electron microscope equipped with an EBSD detector. TSL software (EDAX, Mahwah) was used to acquire and index electron backscatter patterns. This characterization technique is a powerful tool to obtain crystallographic and microstructure analyses, such as crystal orientation mapping, phase identification and grain boundaries investigation.[102,103] EBSD was used in this work to determine the local crystallographic orientation of the polycrystalline samples, specifically the local surface normal of grains.

The surface orientations of grains were quantified using EBSD. The sample was prepared by mounting a stub with a sticky carbon tape. The measurements were set up with the working distance of 10 mm and an accelerating voltage of 15 kV with a spot size of 5. To conduct a measurement, the sample was tilted at 70°. When the incident electron beam interacts with the sample, some electrons diffract and travel out of the sample. The pattern of these diffracted electrons, which consists of Kikuchi bands, is captured on a phosphor screen. Each band originates from a set of parallel planes. The angles between the bands correspond to the angles between planes and the width is related to the *d*-spacing. Successfully determining the orientation of the crystal amounts to correctly assigning the identity of the bands.[104] In practice, commercial software compares known interplanar angles with those observed in the pattern and chooses an orientation solution that best explains the pattern. Note that, while this process has been shown to be highly reliable, the obtained solution only represents the orientation that the software determines to fit the pattern with the highest confidence.

EBSD patterns were automatically collected and indexed by the TSL software.[105] It should be noted that, to simplify the indexing processes, the monoclinic samples were indexed in the tetragonal Laue group 4/m because the parameters of **a** and **b** in the monoclinic structure are almost identical (only 2 % difference) and the angle is almost 90°.[99] From the point of view of EBSD, monoclinic fergusonite and tetragonal scheelite are basically identical. Monoclinic fergusonite $BiVO_4$ with space group space group **I**2/**b** has lattice parameters of **a** = 5.1956 Å, **b** = 5.0935 Å, **c** = 11.704 Å, and **γ** = 90.383. Tetragonal scheelite $BiVO_4$ with space group **I**4_1/**a** has lattice parameters of **a** = 5.147 Å and **c** = 11.7216 Å.[99]_Using the higher symmetry tetragonal group simplifies the analysis and the reactivity results are not impacted by this approximation.[106]

To produce grain orientation maps, an electron beam is scanned over a particular area of the sample in a stepwise fashion and the diffraction patterns from each point are indexed automatically to determine the orientation. The orientation is denoted on a map by a unique color. A grain is formed by a group of nearby points whose orientations are the same within a certain tolerance. The orientation data can be used to quantify the crystallographic texture of the sample. The samples studied here all had random textures. The step size of the scan is 0.1 μm. The raw orientation data was cleaned using typical algorithms,[105] including a dilation algorithm (using 5 ° tolerance angle and a 10 pixel minimum grain size), a grain orientation averaging algorithm (using 5 °), and a pseudo-symmetry correction algorithm. To verify that this simplification of the symmetry did not impact the results, several experiments were conducted using the monoclinic cell and point symmetry 2/m. Examples of these results are included in Appendix 3. Both tetragonal and monoclinic indexing schemes yield consistent orientations for all grains. Also, there were no detectable differences between the reactivities of the (100) and (010) surfaces. As such, use of the simpler tetragonal system is appropriate. After classifying the extent of reactivity, the orientations of grains with high and low reactivity were plotted in an orientation distribution diagram.

3.2.3 Photochemical experiment (Marker reaction)

In this study, I used the reduction of silver and the oxidation of lead oxide and manganese oxide to evaluate the reactivity of a surface. These marker reactions have been well established by previous researchers. For example, the reduction of silver ($Ag^+ + e- \rightarrow Ag_{(s)}$) is widely used to observe the reduction site.[107,108] The silver metal product is insoluble and forms deposits on the surface. As a result, the deposition of the reaction product can be investigated by microscopic techniques.

For the reduction experiment, Ag^+ from an aqueous solution of 0.115 M $AgNO_3$ was photochemically reduced to an insoluble Ag product on the sample's surface. The deposits create topographic contrast in AFM images, so they can be observed. Similarly, Pb^{2+} from an aqueous solution of 0.115 M $Pb(NO_3)_2$ and Mn^{2+} from an aqueous solution of 0.115M $MnSO_4$ were photochemically oxidized to Pb^{4+} and Mn^{3+}/Mn^{4+} ions yielding an oxide of PbO_2 and MnO_x, respectively.[109,110] Both PbO_2 and MnO_x are also insoluble and the oxidation products can be observed by AFM. It should be noted that because the conduction band edge of $BiVO_4$ is below the redox potential of H_2, $NaIO_3$ was added as an electron acceptor when the oxidation reactions were being carried out. To conduct the photochemical experiment, an O-ring was placed on the surface of the specimen and then filled with the aqueous solution. A quartz slip was put on top of the O-ring(s) to create a flat and uniform surface for illumination. Then, the samples were illuminated from the topside using a blue LED (λ_{peak} = 470 nm). Three experimental setup parameters were adjusted to be suitable for each study, specifically the power of the light source, the distance between the light source and the sample, and the exposure time. The setups of the photochemical experiments for each study will be described separated in detail in the chapter of each study.

After the photochemical experiments, the samples were then imaged by atomic force microscopy (AFM). In addition, the phase and the compound of the reaction products were examined by x-ray diffraction and energy dispersive x-ray spectroscopy (EDS). Because of the sensitivity of XRD and EBSD, the sample needs to be overexposed for 30 minutes for each experiment. Otherwise, the reaction products cannot be detected by the characterization technique. It should also be noted that the reduction product from $AgNO_3$ solution could be identified; however, neither EDS nor XRD could examine the oxidation products from $Pb(NO_3)_2$ and $MnSO_4$ solution because the highest intensity peak and the EDS spectrum of PbO_2/MnO_x is overlapped with that of $BiVO_4$, which is the matrix phase.

3.2.4 Atomic Force microscopy (AFM)

Atomic force microscopy (AFM) was used to investigate the surface topography of ferroelastic domains before and after the reactions. AFM is a scanning probe microscopy (SPM) technique.[111] This technique scans a probe across a sample's surface to acquire images. The images show some material property, such as topography or friction, as a function of position. Fig. 3.1 schematically shows the principle of AFM. A cantilever is moved along the surface, and the sharp probe tip on the cantilever is sensitive to atomic forces between it and the sample's surface. Changes in these forces act to deflect the cantilever vertically or laterally. By measuring a vertical or lateral deflection with an optical lever, which is an array of photodiodes detecting a laser reflection from the cantilever, a physical property can be obtained.

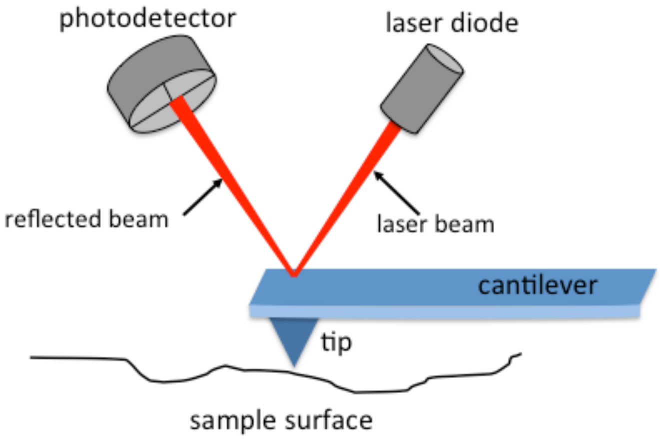

Figure 3.1. Atomic Force Microscopy measurement shows the basic components of AFM system: cantilever, laser diode and photodetector.

The sample topography was imaged using the AFM in a tapping mode. This mode is carried using amplitude modulation detection with a lock-in amplifier. In this operating mode, the cantilever was oscillated at near the resonance frequency (300Hz) and was tapping near the surface. The change in heights causes a change in the original oscillation of the cantilever. In other words, the changes of topography cause deflections in the cantilever resulting in a change of the cantilever amplitude. The reduced amplitude was detected and was interpreted to obtain the topography of the sample. The obtained topographic AFM images can reveal the appearance of ferroelastic domains on the samples.

The most important information extracted from the images are the heights of the reaction products. The heights of deposits were used for qualitative analysis of determining photochemical reactivity on each surface orientation. To analyze the reactivity, the sample topographic images before and after reaction were compared. After reaction, deposits increased the relative height (maximum height –minimum height) and could be seen as white contrast on the images. All AFM images were collected using a Solver Next AFM. An n-type silicon probe was used for the measurement with the resonance frequency of 300 Hz. The reactivity was determined by the relative height of the deposits. After image acquisition, image processing, such as flattening, was conducted to reduce the effect of surface defects (e.g. pores and scratches) on the quality of the topographic image.

3.2.5 Piezoresponse force microscopy (PFM)

Besides surface topography, the AFM can be used to measure the surface piezoresponse using a mode called piezoresponse force microscopy (PFM), as shown in Fig. 3.2. By applying a voltage to the conductive tip, PFM can measure the electromechanical coupling or piezoresponse of the sample's surface.[112–114] Principally, the magnitude of the applied voltage can be described by the following equation:

$$V_{tip} = V_{DC} + V_{AC} \cos(\omega t) \tag{3.1}$$

where V_{DC} is a switching bias that can be applied through a tip or a sample, and V_{AC} is the probing bias. Such a voltage can result in a deflection of the cantilever, which can be defined as:

$$A = A_0 + A_1\omega \cos(\omega t + \varphi) \tag{3.2}$$

The two parameters in Eq. 3.2, the amplitude ($A_1\omega$) and phase (φ), can be used to create images. The amplitude signal is correlated to the magnitude of surface polarity, while the phase signal is associated with the direction of polarization with respect to the surface. For example, in ferroelectrics, if a domain has a positive phase signal, there is a positive-ended dipole at the surface. Likewise, domains giving a negative phase signal have the opposite polarization at the surface. Thus, this technique is commonly used to image domain structures in ferroelectrics.[112,113]

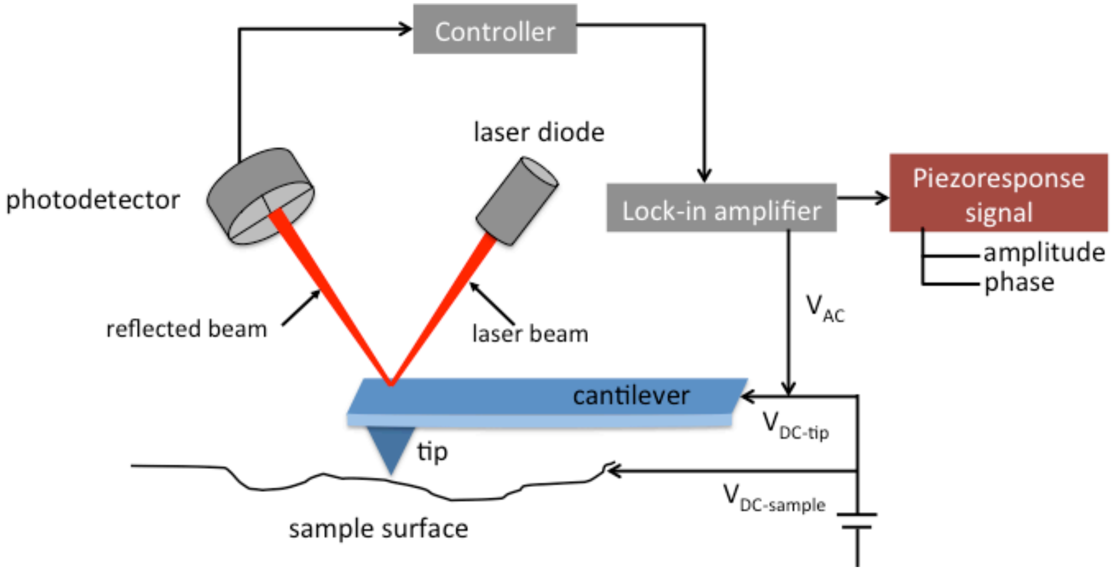

Figure 3.2. Piezoresponse Force Microscopy measurement demonstrates the system components. In addition to the basic components of the AFM system, PFM is connected to the bias supply.

PFM measures the contraction or expansion due to the piezoelectricity of the sample when electrical stimulus is applied. Specifically, a domain will expand if the applied bias is the same type as the surface polarization (+/+ or -/-), while a domain will contract if the applied bias is opposite to the surface polarization (+/- or -/+). The expansion and the contraction will give rise to contrast in PFM images.

In addition to ferroelectrics, previous studies surprisingly reported the use of PFM to demonstrate the surface's polarization of non-ferroelectric materials. Kholkin *et al*. applied PFM to study the polar phonomena of a centrosymmetric $SrTiO_3$ ceramic at room temperature and found the local piezoelectric contrast of the PFM images.[113] The obtained PFM images revealed the grain-sensitive piezorepsonse. Specifically, the image's contrast was varied by grain orientations. The phenomenon was speculated to be caused by surface piezoelectricity arising from the flexoelectric effect, which arises from a strain-gradient induced by a surface relaxation.

In this current study, PFM was used to image piezoresponsive domain structures at the surface of ferroelastic $BiVO_4$ samples. The measurement was conducted using Solver Next AFM. Such a measurement was operated under the contact mode using a N-doped Si probe. During the measurement, the voltage is applied to the sample, so it is necessary to ground the sample. Thus, the sample was grounded with a special sample holder or using a conductive carbon tape to attach the surface to the ground.

3.2.6 Conductivity measurement

The van der Pauw technique is a 4-point probe conductivity measurement technique that is used especially for arbitrarily shaped samples.[115] Other than resistivity, the van der Pauw measurement can determine carrier density, major carrier mobility and the Hall coefficient of a sample. Despite no restriction in sample shapes, homogeneity of thickness and composition of samples is required. Also, to eliminate the contact resistance, the contacts must be relatively very small in size on the perimeter of the sample structure. The error in measurement can be determined by the ratio of the average diameter of the contacts to the distance between contacts.

For a comparative study of photochemical reactivity in Study 3, the co-doped monoclinic and tetragonal samples should have a comparable conductivity. Thus, to verify the validity of the comparison, the resistivity of the polished samples was measured for the order-of-magnitude conductivity using this technique.

In the measurement, four contacts were made on the edge of the samples by connecting a copper wire with silver paint. Each contact is roughly equally spaced. After applying the silver paint, the contacts were left to harden. Eight configurations of the measurements (four configurations shown in Fig. 3.3 and their conjugates, in which the direction of the source current is reversed) were carried out.[116] Basically, to obtain the resistivity, the current is applied from one contact to another contact, and the resultant voltage across the remaining contacts is then measured.[117] The voltage and the current were used to calculate the resistivity. The resistivity can be calculated by Eq. (3.3) – (3.5).

$$\rho = \frac{\rho_A + \rho_B}{2} \tag{3.3}$$

$$\rho_A = \frac{\pi t}{ln2} R_A f_A \tag{3.4}$$

$$\rho_B = \frac{\pi t}{ln2} R_B f_B \tag{3.5}$$

where ρ is a volume resistivity (Ω-cm), t is thickness (cm), R_i is resistivity across the contacts (Ω), and f_i is a correction factor regarding the symmetry of sample geometry and related to the resistance ratios (Q_A and Q_B).

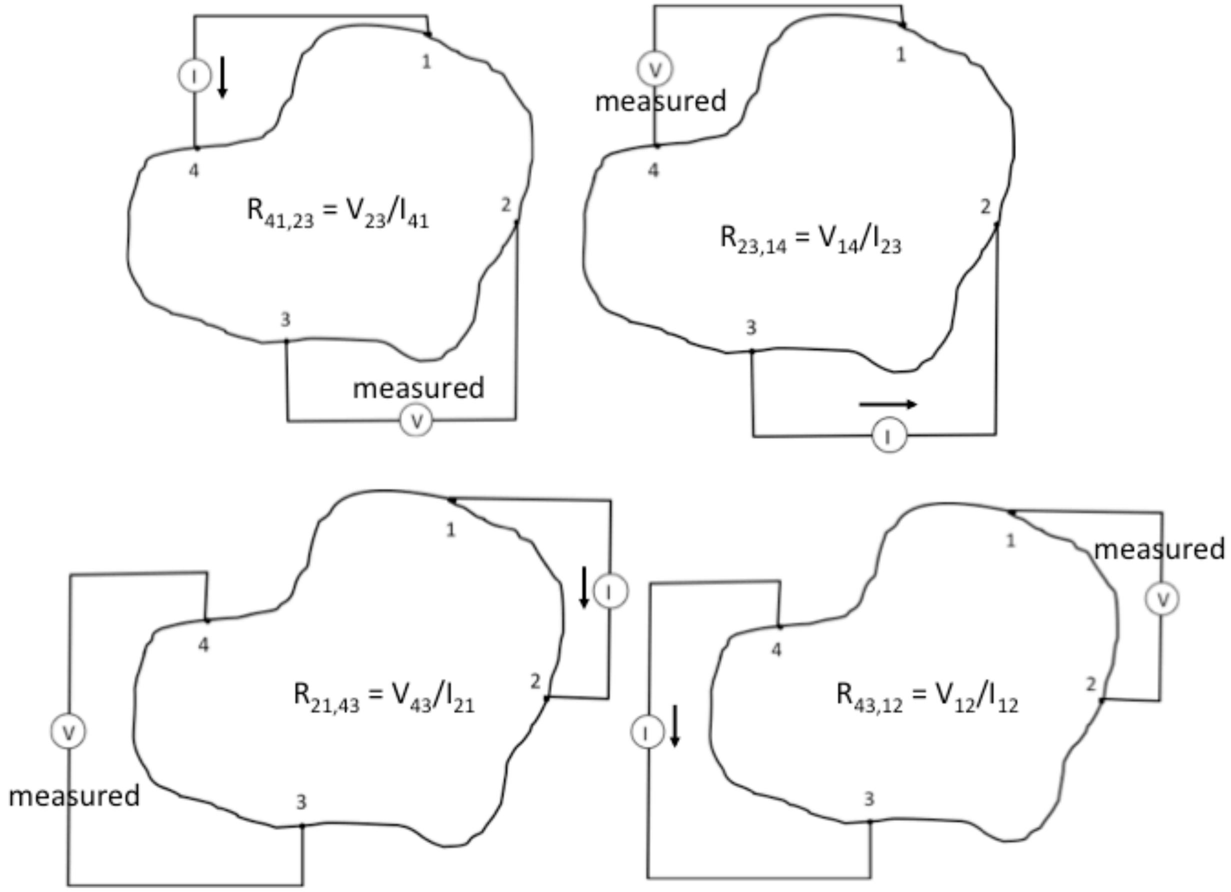

Figure 3.3. Resistivity measurement configurations

and R_A and R_B , and Q_A and Q_B are given as follows:

$$R_A = \frac{R_{41,23} - R_{14,23} + R_{21,43} - R_{12,43}}{4I} \tag{3.6}$$

$$R_B = \frac{R_{23,14} - R_{32,14} + R_{43,12} - R_{34,12}}{4I} \tag{3.7}$$

$$Q_A = \frac{R_{41,23} - R_{14,23}}{R_{21,43} - R_{12,43}} \tag{3.8}$$

$$Q_B = \frac{R_{23,14} - R_{32,14}}{R_{43,12} - R_{34,12}} \tag{3.9}$$

Then, Q_A and Q_B are used to estimate the f_A and f_B factors from the graph illustrated in Fig. 3.4.

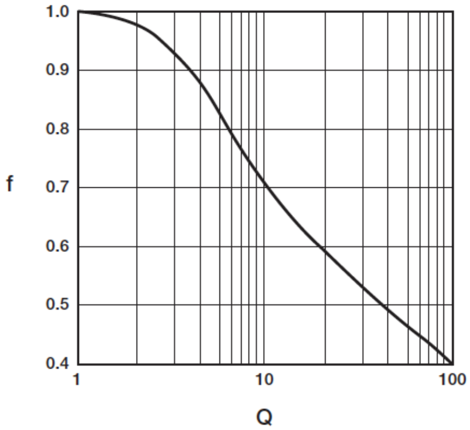

Figure 3.4. The relationship between Q and f factors[117]

Chapter 4

STUDY 1:

Orientation-Selectivity of Photochemical Reactions

4.1 Chapter overview

Bismuth vanadate, $BiVO_4$, is of interest for its high efficiency as a photoanode for water splitting.[85] With a band gap of approximately 2.4 eV and a valance band edge positioning at ~2.5 eV with respect to hydrogen reduction,[118] $BiVO_4$ has an ability to oxidize water using holes excited by visible light. Theoretically, $BiVO_4$ can obtain as high as 10% efficiency. However, $BiVO_4$ is not currently able to reach its predicted efficiency because of electron-hole recombination; quantitatively, 60-80% of the total photogenerated electrons and holes recombines before arriving at reaction sites.[118,119] This problem underscores the need to spatially separate electron-hole pairs effectively to prevent recombination.[15,16] Morphological control has been suggested to limit recombination in $BiVO_4$ crystals.[120–122] It is known that different surfaces of the same crystal are able to promote different reactions; the orientation-dependent reactivity, for example, was found in TiO_2 and $SrTiO_3$.[19,27,123] In the case that one surface promotes reduction and the other promotes oxidation, it would be possible to create photocatalysts that spatially separate the oxidation and reduction reactions.[21,120]

Previously, the orientation dependence of $BiVO_4$ reactivity was also presented.[20,120] Before discussing the prior results, it is necessary to make some comments about the crystallography used for $BiVO_4$ system. $BiVO_4$ can crystallize in three structures: a tetragonal zircon structure, a tetragonal scheelite structure, and a monoclinic fergusonite structure. Because of similar atomic arrangement of the tetragonal scheelite and monoclinic fergusonite structures, the latter structure is sometimes referred to as "monoclinic scheelite." Of these, the monoclinic structure has been reported to be the most photochemically active.[124] As a result, this study will focus on photochemical properties of the monoclinic fergusonite phase, which is the equilibrium structure at room temperature and pressure.[87] The monoclinic fergusonite structure ($I2/b$, $\mathbf{a}$ = 5.1935 Å, $\mathbf{b}$ = 5.0898 Å, $\mathbf{c}$ = 11.6972 Å, γ = 89.613°, or a complementary angle of 90.387°) can be obtained from the transformation of the tetragonal scheelite structure ($I4_1/a$, $\mathbf{a}$ = 5.147 Å $\mathbf{c}$ = 11.7216 Å) through a small distortion below 255 °C.[87] This transformation alters the cell parameters by less than 1% and creates a ferroelastic domain structure[125] that also affects the reactivity.[126] The effect of domains on reactivity is discussed in later chapters of this thesis.

$BiVO_4$ can be described using different conventions. Two different choices have been made in the past for monoclinic $BiVO_4$: modern and non-standard crystallographic conventions. If the unit cell is selected according to modern crystallographic conventions, then it should be consistent with group C2/c, making the longest axis b. However, the non-standard choice of space group I2/b makes the c-axis the longest, preserving the relationship with the more idealized tetragonal structure. The latter choice is used in this thesis for consistency with the approximation used in the electron backscatter diffraction (EBSD) experiments. In all comparisons to previous work, I shall use indices in I2/b, even when the previous authors indexed the cell in C2/c.

Many investigations have shown that the rate of photochemical evolution can differ with $BiVO_4$ surface orientations. Wang *et al*.[120] measured the amount of O_2 evolved from an aqueous solution of $AgNO_3$ and found that the oxygen-evolving rate (i.e., the oxidation reaction rate) on $BiVO_4$ during visible-light illumination increases with the area of the (001) facet. Later, the reactivity of polygonal $BiVO_4$ particles bounded almost entirely by (001), (101) and (011) facets was studied.[20,21] Marker reactions that leave insoluble products on the surface where oxidation and reduction occurs were used to show that reduction was promoted on (001) facets and oxidation was promoted on (101) and (011) facets. Hypothetically, this was attributed to small differences in the valance and conduction band edges at the two surfaces that promoted electron transfer to (001).[20] More detailed calculations suggest that there are several competitive factors and that a single simple parameter may not be sufficient to describe the orientation dependence of the reactions.[28]

The purpose of this chapter is to describe the complete orientation dependence of surface reactivity on $BiVO_4$. Whereas the previous work[20,21,120] concentrated on polygonal particles exposing only (001), (101), and (011) facets, this study employs a method that allows one to compare the reactivities of all possible orientations, which can indicate the preferences among the different oriented surfaces for reduction and oxidation. The results make it possible to propose an ideal particle shape to promote charge carrier separation.

4.2 Experimental method

Monoclinic $BiVO_4$ was prepared by a conventional solid-state reaction using a stoichiometric mixture of Bi_2O_3 and V_2O_5 powders. The mixture was ball-milled overnight using yttria stabilized zirconia grinding media and ethanol as a lubricant. After ball milling, the mixture was dried at 85 °C and then heated to 650 °C in air for 2 hours to complete the reaction. The reacted powder was then manually ground to reduce the particle size. The powder was mixed with 5 wt% of PVA in ethanol as a binder and compressed to form a 1-cm-diameter cylindrical specimen with a thickness of ~ 3 mm. The pellet was annealed at 500 °C for 6 hours to decompose the binder and any other organics, and then sintered at 800 °C for 12 hours. Powder x-ray diffraction was used to verify that the product had the structure of monoclinic fergusonite, as expected for $BiVO_4$ at room temperature.

The surface was prepared by lapping, polishing and annealing. First, the sample was lapped using SiC abrasive papers (initially with 320 grit and followed by 400, 600, 800 and 1200 grit, sequentially) to get a flat surface. Afterwards, it was consecutively polished with 1 μm, 0.3 μm and 0.05 μm alumina suspensions. Each lapping step required several minutes, while each polishing step took 30 – 60 min. Finally, the sample was annealed in air at 300 °C for an hour to repair surface damage accumulated during the polishing.

Electron backscatter diffraction (EBSD) was used to determine the orientations of the crystals at the surface of the sample. EBSD measurements were carried out in a Quanta200 scanning electron microscope (FEI company) equipped with an orientation imaging microscopy (OIM) system that used a Hikari charge coupled device (CCD)-based detector to collect the diffraction patterns. TSL software was used to analyze the surface orientations and generate an orientation map of the scanned area. As noted in the first section, the room temperature structure of $BiVO_4$ is monoclinic, with space group $I2/b$ and lattice parameters $a = 5.196$ Å, $b = 5.094$ Å, $c = 11.7045$ Å, and $\gamma = 90.38°$.[87] Because a and b differ by only 2%, and γ is nearly equal to 90°, the cell is approximately tetragonal, analogous to the higher temperature scheelite-structured parent phase. Therefore, to simplify the orientation measurements, we assumed that $BiVO_4$ has a tetragonal unit cell with lattice parameters a = 5.1509 Å and c = 11.73 Å and indexed the EBSD patterns in Laue group 4/m. The most important artifacts of this assignment are that the longest axis is [001] and the crystallographically distinct (100) and (010) monoclinic surfaces become indistinguishable. Orientation maps were recorded over 200 μm x 200 μm areas with a step size of 1 μm. Several 'clean-up' procedures were used to minimize the number of un-indexed or incorrectly indexed pixels. First, a grain dilation clean-up was applied using a 5° tolerance angle, a 10 pixel minimum grain size, and a so-called multiple row requirement. The fraction of points changed in this clean-up process was about 19%. Next, an average orientation was assigned to each grain, where a grain is defined with a tolerance angle of 5°. Finally, the use of tetragonal 4/m Laue group for the monoclinic system results in some grains having two different orientations (in different pixels within the same grain) that are related by a 90° rotation about the c-axis. This can create artificial apparent boundaries within single grains. Most of these could be (and were) removed using a psuedosymmetry clean-up with a 5° tolerance. Several experiments were also conducted using the monoclinic cell and point symmetry 2/m and examples are illustrated in the Appendix 3. The tetragonal and monoclinic indexation schemes are consistent for all grains. However, as no differences were found between the reactivity of the (100) and (010) surfaces, I choose to use the simpler tetragonal system to describe the results.

The photochemical reactivity of individual grains was evaluated using reactions that left a solid product on the surface, which could then be observed microscopically. Aqueous solutions of 0.115 M $AgNO_3$ were used for the photochemical reduction of Ag^+ to Ag^0.[107,108] Aqueous solutions of 0.115 M $Pb(NO_3)_2$ and of 0.115 M $MnSO_4$ were used for the photochemical oxidations of Pb^{2+} to Pb^{4+} and of Mn^{2+} to Mn^{3+}/Mn^{4+}, respectively.[127,128] For the case of the Pb^{2+} and Mn^{2+} bearing solutions, an electron acceptor (IO_3^-) was added as 0.23 M $NaIO_3$ to the solutions to promote the counter redox reaction of reduction. Because insoluble $Pb(IO_3)_2$ or $Pb(IO_3)$ or $Mn(IO_3)_2$ always formed after the addition of the $NaIO_3$, the mixture was filtered to remove the precipitate and the clear supernatant was further used in the experiment.

The same procedure was used for each photochemical experiment. An O-ring was placed on the sample surface to create a reservoir that was then filled with the metal-bearing solution. The top was sealed with a quartz cover slip that was held in place by capillarity. Illumination was provided by a blue light-emitting diode (LED, wavelength of 470 nm, 2.64 eV) placed just above the sample and in contact with the cover slip. The LED was operated at 5 V with a current of 750 mA. $BiVO_4$ has different activities for the different reactions, so the exposure time was optimized so that the reaction product was easy to detect in atomic force microscope images, but not so prevalent that the large topographic variations complicated the imaging. The exposure times were 1 min, 20 min, and 5 min for the $AgNO_3$, $Pb(NO_3)_2$, and $MnSO_4$ solutions, respectively. Reduction and oxidation reactions were carried out on the same sample, on the same areas. After Ag reduction, the sample surfaces were gently wiped off with methanol-wet cotton swabs and ultrasonically cleaned in acetone and methanol to remove silver deposits, before the oxidation reaction. To verify that the reaction products were formed through photochemical processes, control experiments were performed in which the sample was immersed in the metal bearing solutions for 30 min, but without illumination. In these cases, no reaction products were found on the surface.

The reaction products were characterized by energy dispersive x-ray spectroscopy (EDS) in an SEM equipped with an Octane Plus EDS detector and by x-ray diffraction. The products identified after the reduction and oxidation reactions were silver and lead oxide, respectively. The x-ray diffraction patterns of the products confirmed the EDS results.

The surface topography of the same areas in the orientation maps, before and after the reactions, was measured by atomic force microscopy (AFM) using a SolverNext NT-MDT scanning probe microscope operated in tapping mode. Features that appeared on the surface after the reaction were assumed to be the reaction product. Because it is topographically higher than the surrounding surface, the reaction products appear as bright contrast in the AFM images. The relative reactivities of different surfaces were determined by the relative heights of the deposits compared to the surface before the reaction. The effect of orientation on the reactivity was investigated by correlating the surface orientation with the measured reactivity.

4.3 Results

4.3.1 Orientation determination

Fig. 4.1 displays an inverse pole figure map obtained from EBSD analysis with color key from the tetragonal reference frame. It should be noted that the lattice parameters of the monoclinic fergusonite (**a** = 5.1935 Å, **b** = 5.0898 Å, **c** = 11.6972 Å, γ = 90.38°)[87] and ones of the tetragonal scheelite (**a** = **b** = 5.147 Å, **c** = 11.7216 Å)[87] are almost identical. Thus, the monoclinic fergusonite $BiVO_4$ can be considered as a distorted tetragonal scheelite $BiVO_4$. The similarity of the structures validate that our structural approximation for the EBSD analysis is reasonable. The colors in the map represent the orientations of grains regarding the standard stereographic triangle of the higher symmetry tetragonal reference frame. The figure is composed of a number of grains with distinguishable orientations. Grains with distinct orientation meet at grain boundaries where the orientation changes. The existence of all colors in this map with no obvious preference indicates that the sample has a random orientation (i.e., all orientations can be addressed for reactivity).

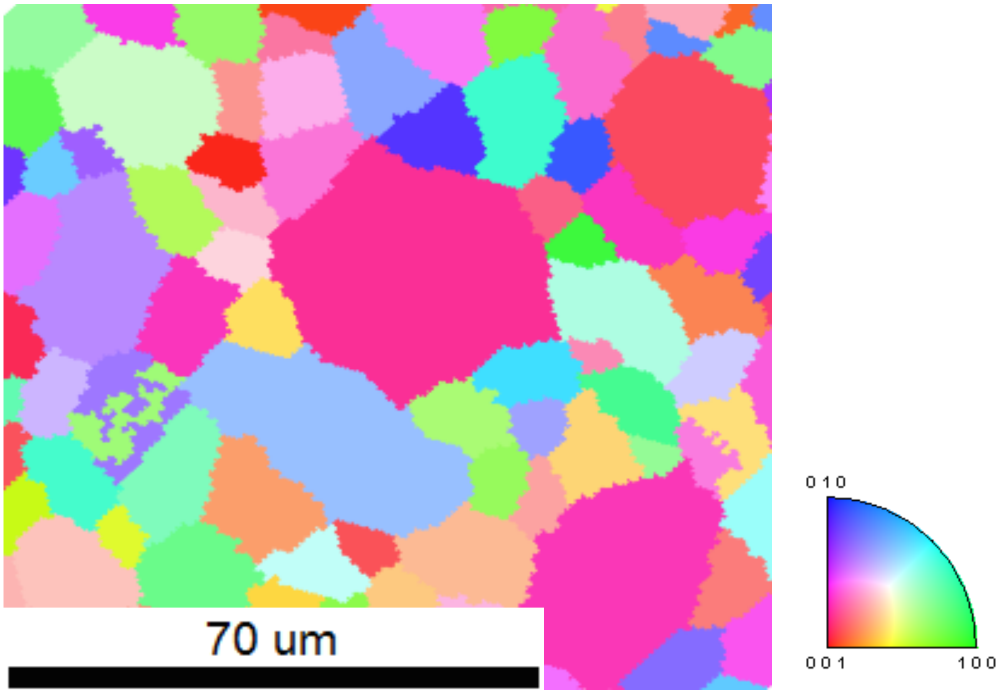

Figure 4.1. Color-coded inverse pole figure (IPF) map of bulk $BiVO_4$ sample

4.3.2 Preference of Silver Reduction

The effect of Ag reduction on the surface is illustrated in Fig. 4.2. The AFM images in Fig. 4.2(a) and Fig. 4.2(b) show the surface topography before and after reduction, respectively. In Fig. 4.2(b), the different heights of the grains lead to abrupt changes in contrast at the grain boundaries and the striped contrast within the grains corresponds to ferroelastic domains, which will be discussed in further chapter. While these domains obviously influence the reactivity, this chapter mainly focuses on the effect of grain orientation. By comparing the images in Fig. 4.2(a) and 4.2(b), it is clear that more silver deposits were found on some grains compared to others; this is confirmed by the topographic profiles in 4.2(c) and 4.2(d). On the surface of the grain with low reactivity (denoted with L), the silver deposits have an average height of ~ 12 nm, while the height of the reaction product on the highly reactive surface (denoted with H) is ~ 70 nm.

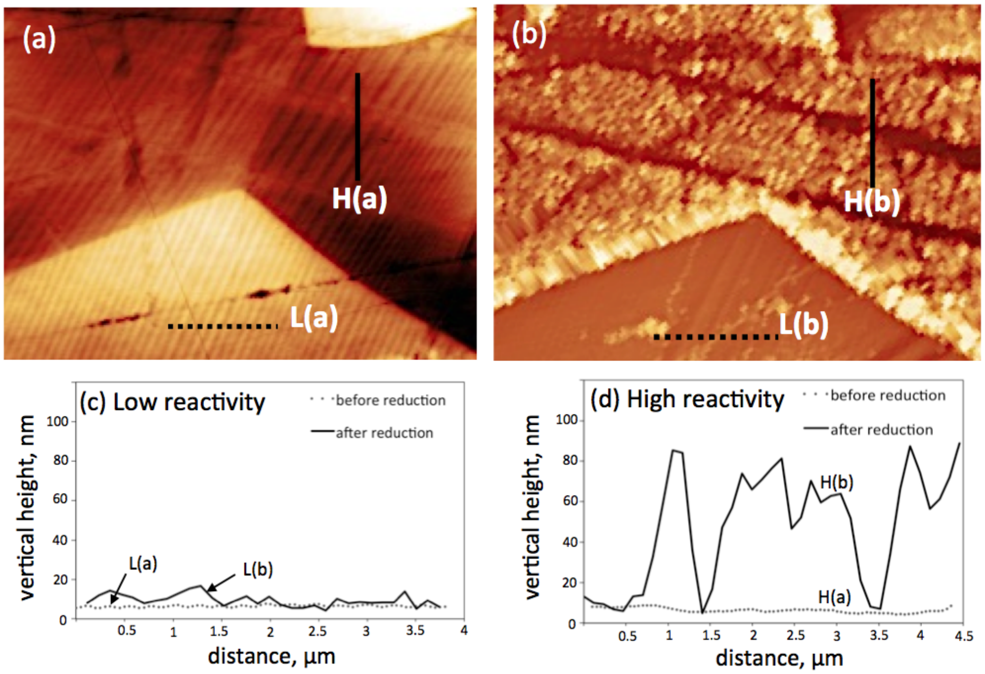

Figure 4.2. Silver reduction on the $BiVO_4$ surface (a) topography before reduction, (b) topography after reduction. The height profile of the low reactivity grain ('L' line) and one of the high reactivity grain ('H' line) are shown in (c) and (d), respectively. The black-to-white contrast is 12 nm in (a) and 90 nm in (b). The field of view is 10 µm x 15 µm.

.

The images in Fig. 4.3 compare the topography of the surface after the reduction of Ag to the grain orientations measured by EBSD. It should be noted that Fig. 4.3(a) is a montage of smaller images, so there are some discontinuities in the contrast. To illustrate the correspondence between the images, the same two grains are outlined with a white line. Based on the contrast in the AFM images, the reduction of silver is clearly heterogeneous. There are two types of heterogeneities. The first is a grain-by-grain reactivity that changes abruptly at the grain boundaries. The present chapter focuses on this grain-to-grain heterogeneous reactivity. Other heterogeneities arise from the presence of polishing scratches and ferroelastic domains. The polishing scratches are long straight features that traverse grains boundaries uninterrupted and one is labeled 'PS'. The ferroelastic domains are parallel stripes contained within grains. There are also occasional "islands" of higher reactivity that occur within grains (examples marked with an "x" in Fig. 4.3(a)). These features will not discussed here and I focus instead on the variations related to grain orientation, away from these islands. From a qualitative perspective, the trend in reactivity with orientation seems obvious. For instance, the grains with high reactivity in Fig. 4.3(a) have orientations near (001) in Fig. 4.3(b). Similarly, the grains with low reactivity have orientations that are closer to (*hk*0), roughly perpendicular to (001).

To quantify the orientation dependence of the reduction of silver, about a hundred grains were evaluated according to the heights of the silver deposited on the surface. To measure the height, a height profile was extracted from each grain, as illustrated in Fig. 4.2. Areas classified as highly reactive had silver particles higher than 20 nm. Areas classified with low reactivity had heights less than 20 nm. To illustrate how grains in Fig. 4.3 were classified, low reactivity grains are labeled 'L' and high reactivity grains are labeled 'H'. The orientation distribution of low- and high-reactivity grains is shown in Fig. 4.4. The plots show that there are no low-reactivity grains within 40° of (001). The high-reactivity grains appear to be clustered near (001), and fewer grains are found as the inclination from (001) is increased.

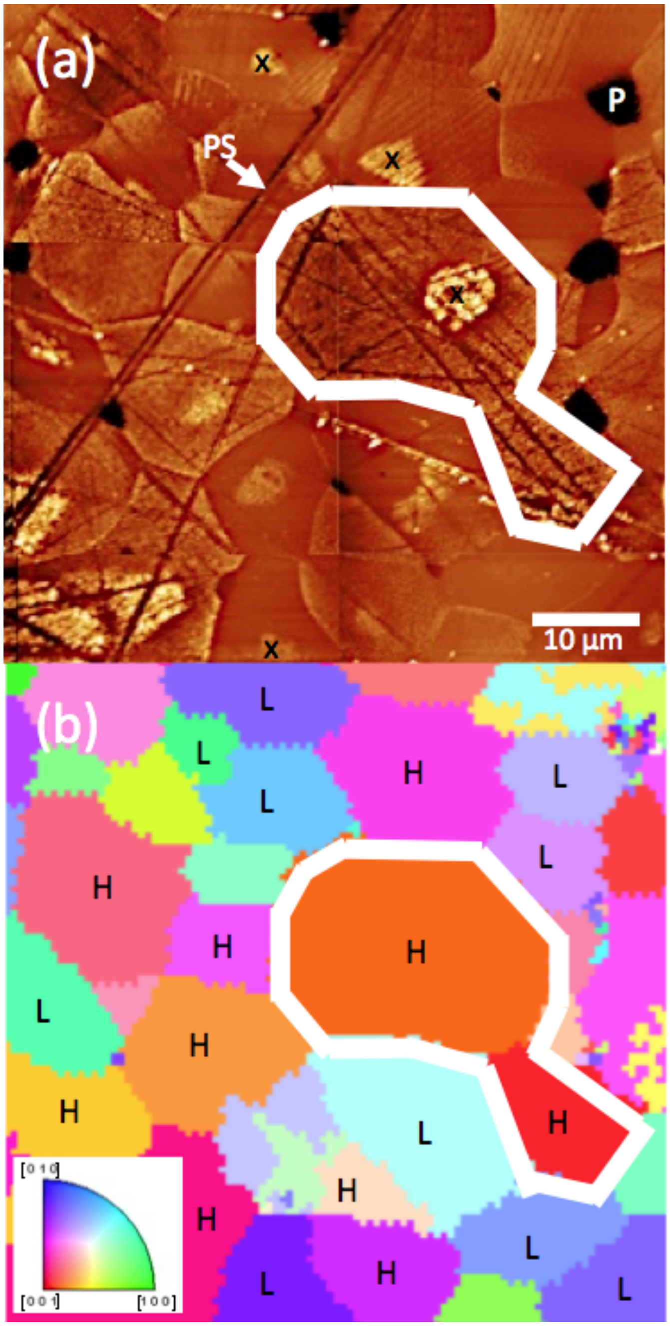

Figure 4.3. (a) Topographic AFM image after Ag reduction. The black-to-white vertical contrast is 196 nm. (b) Orientation map of the same area. The color key is shown in the inset. The field of view is 60 μm x 60 μm. In (a), and example of a polishing scratch is marked with "PS" and a surface pore with "P".

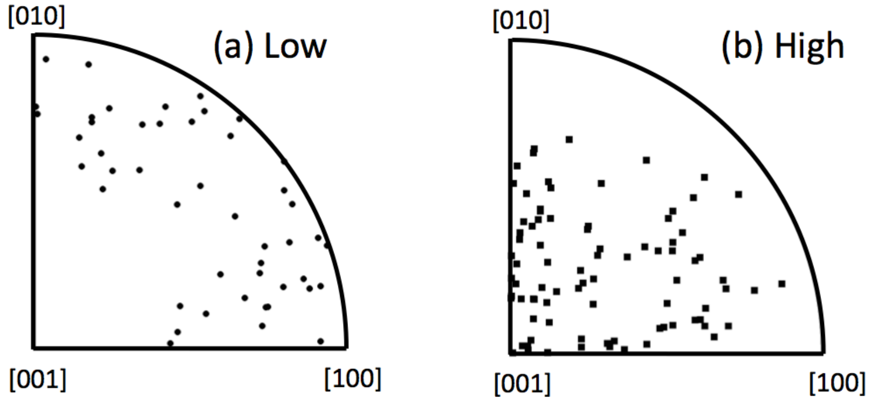

Figure 4.4. Orientations of grains on the $BiVO_4$ surface that were classified as low (a) and high (b) reactivity for the photochemical reduction of Ag. Each point corresponds to an observed grain and the points are plotted in stereographic projection.

To quantify the distribution of high and low reactivity grains, the orientations are compared to those expected in a random distribution. Specifically, the observations are divided in 10° ranges by the fraction that would be found in a random orientation distribution; the resulting units are multiples of a random distribution (MRD). The results are illustrated in Fig. 4.5. In the range between 0° and 10° from [001] (plotted as the bin average of 5°), grains that reduced silver are four times more likely than random and between 80° and 90° from [001] (plotted as the bin average of 85°), grains that reduced silver were five times less likely than expected at random. Similarly, there are no low reactivity grains within 40° of [001], but from 80° to 90° from [001], they are more than twice as likely as in a random distribution. So, while all grain orientations can reduce some silver, grains within 40° of [001] reduce much more in the same amount of time.

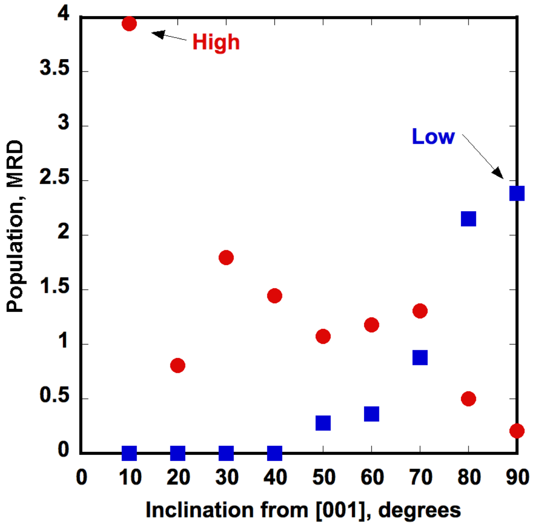

Figure 4.5. The orientation distribution of grains with high and low reactivity, as a multiple of the random fraction. The red circles are for the high reactivity grains and the blue squares are for the low reactivity grains.

4.3.3 Preference of Lead Oxidation

The orientation dependence of the oxidation of Pb^{2+} was determined the same way that the orientation dependence of the reduction reaction was determined. The topography of the $BiVO_4$ surface after illumination in an aqueous $Pb(NO_3)_2$ solution is shown in Fig. 4.6(a) and an orientation map of the same area is shown in Fig. 4.6(b). Overall, the oxidized reaction product (in Fig. 4.6(a)) appears as white contrast, representing features are that are 50-70 nm in height. Ignoring irregularities such as the polishing scratches, it is clear that there are sometimes abrupt changes in the amount of reaction product at grain boundaries, with some grains being reactive (having a large amount of oxidized material on the surface) and others being almost unreactive (very little reaction product on the surface, which is usually located at surface damages, such as scratches and pores). When one compares the orientation map with the distribution of reaction product, it is clear that grains with surface orientations near (001) are unreactive (see grains labeled L), while the more reactive grains (labeled H) are approximately perpendicular to (001).

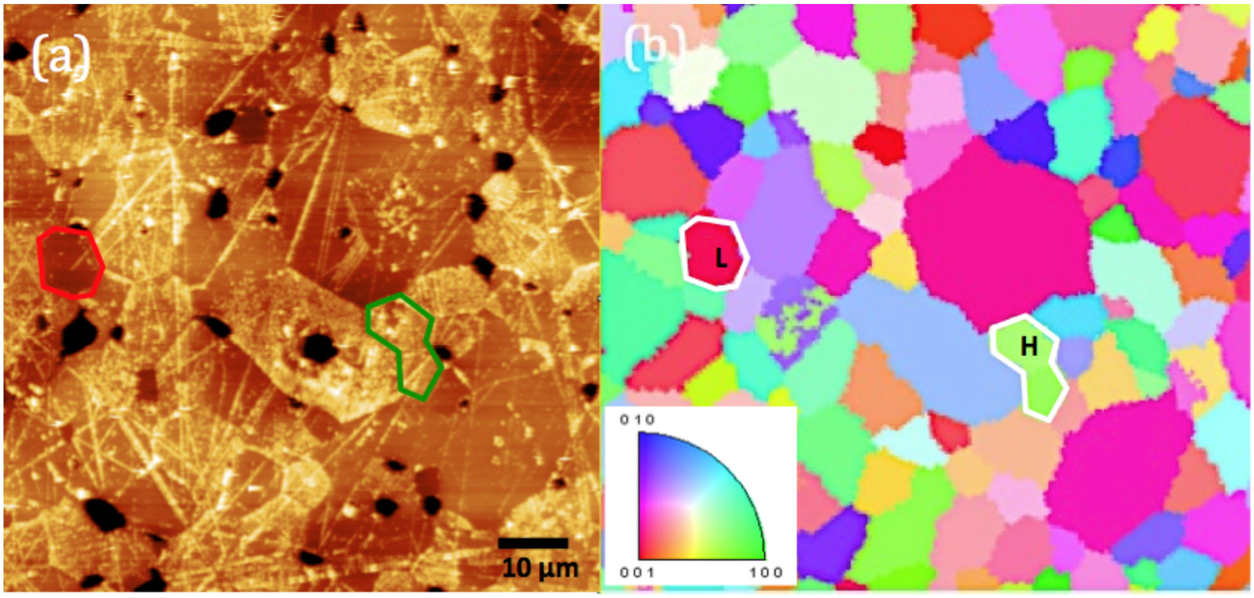

Figure 4.6. (a) Topographic AFM image of the $BiVO_4$ surface after a photochemical reaction in a $Pb(NO_3)_2$ solution. The vertical height from dark-to-light contrast is 220 nm. (b) Orientation map of the same area colored by orientation according to the inset. The field of view is 90 μm x 90 μm.

To demonstrate the orientation dependence of the reactivity, the orientations of 54 reactive and 36 unreactive grains are plotted on the stereographic projections in Fig. 4.7(a) and 4.7(b), respectively. From these observations, it is clear that all of the reactive grains have orientations that are at least 50° from [001] and all of the unreactive grains have orientation that are closer to [001]. Note that this is approximately the opposite of what was observed for the reduction reaction. In other words, grains close to (001) are more active for reduction and grains with orientations perpendicular to (*hk*0) are more active for oxidation.

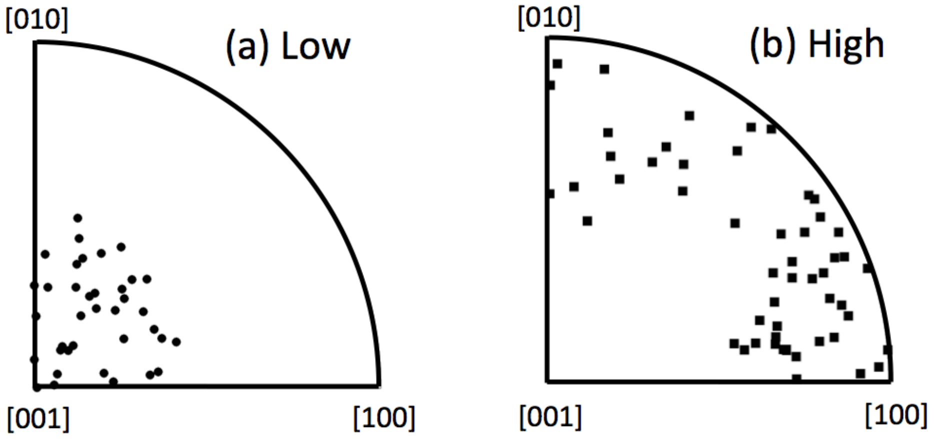

Figure 4.7. Orientations of grains on the $BiVO_4$ surface that were classified as low (a) and high (b) reactivity for the photochemical oxidation of Pb^{2+}. Each point corresponds to an observed grain and the points are plotted in stereographic projection.

4.3.4 Preference of Manganese Oxidation

In addition to the lead oxidation, a Mn^{2+} oxidation experiment was conducted using 0.115M aqueous $MnSO_4$ solution. The topographic images in Fig. 4.8 reveal that insoluble particles of manganese oxide disperse differently from lead oxide particles. In contrast to the lead oxidation, the product of manganese oxidation was deposited uniformly over every grain. This makes it difficult to measure the absolute height of MnO_x deposits on the surface; no non-reacted area can be used as a reference for reactivity measurement. Thus, the quantitative analysis of the preferential orientation for oxidation will be conducted using only data from the Pb^{2+} oxidation. Even though the Mn^{2+} oxidation will not be analyzed for the correlation, its orientation dependence will be observed by comparing contrast of few grains in the same image to approximate the effect of Mn^{2+} oxidation on the surface.

Compared with the Pb^{2+} oxidation result, manganese oxide particles are much finer than lead oxide particles. Specifically, the size of manganese oxide is approximately five times smaller than the size of PbO_2 particles. The size difference may lead to different particle coverage as the coverage of manganese oxide is smoother than that of lead oxide.

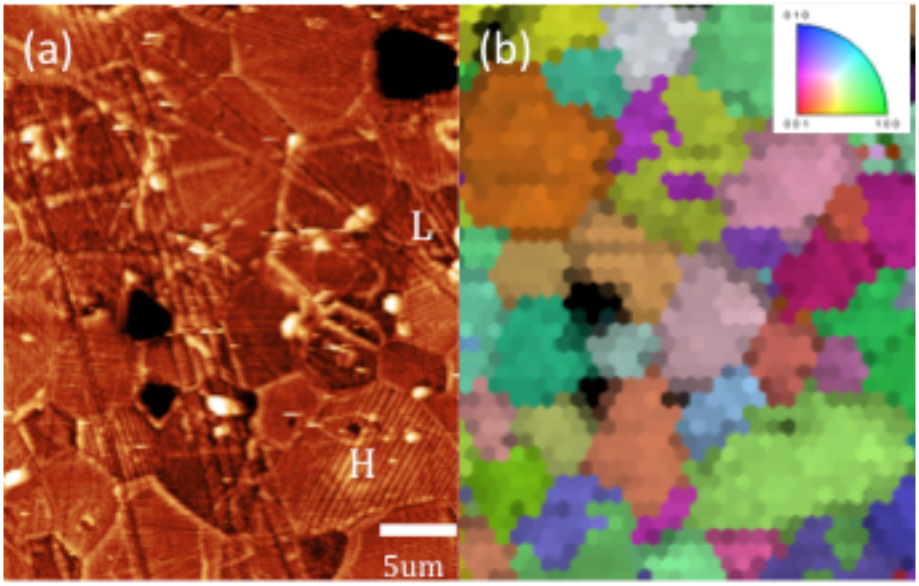

Figure 4.8. After oxidation with $MnSO_4$ solution (a) surface topography from AFM measurement. The vertical height from dark-to-light contrast is 230 nm. and (b) OIM map from EBSD of the same area in (a) colored by orientation according to the inset. The field of view is 30 μm x 40 μm.

Besides the different coverage, the distribution of both oxidation reactions in the orientation space is also dissimilar. In the case of the Pb^{2+} oxidation, the active grains have orientations that are at least 50° from [001], and all grains are equally active. On the contrary, all orientations are active for the Mn^{2+} oxidation, but show some degrees of difference in reactivity. For example, in Fig. 4.8, a grain that orient close to (001) (denoted with L) has some deposit, while grains with similar orientations show no reactivity for the Pb^{2+} oxidation. Also, the close-to-(001) oriented grain has the lowest contrast, which implies low reactivity for manganese oxidation. Conversely, a grain with the orientation that is nearly perpendicular to (100) (denoted with H) has the highest reactivity. Thus, it is likely that the reactivity gradually enhances from the lowest reactivity of near-(001) surfaces to the highest reactivity of perpendicular-(001)

surfaces. In other words, the reactivity for Mn^{2+} oxidation increases with an inclination of angles away from [001]. This is consistent with the result of the Pb^{2+} oxidation that the favorable orientation for oxidation is about perpendicular to [001].

4.3.5 Complementarity of the redox reactions

The topography of the same area of the $BiVO_4$ surface after silver reduction and after lead oxidation is compared in Fig. 4.9. The grains that reduce the most Ag are inactive for Pb oxidation, and those that oxidize Pb^{2+} are less active for Ag reduction, which indicated that (001) and (*hk*0) orientations have complementary reactivity. However, it should be noted that there is a range of orientations that have some activity for both reactions. In Fig. 4.10, the populations of grains that have high reactivity for oxidation and reduction are compared. The population of the grains that has high reactivity for reduction is centered at (001) and the population of grains that has high reactivity for oxidation is centered at (*hk*0). At the limiting ranges of the orientations, grain's reactivity is almost exclusively reduction or oxidation. However, for a range of orientations between these limits, both oxidation and reduction are possible.

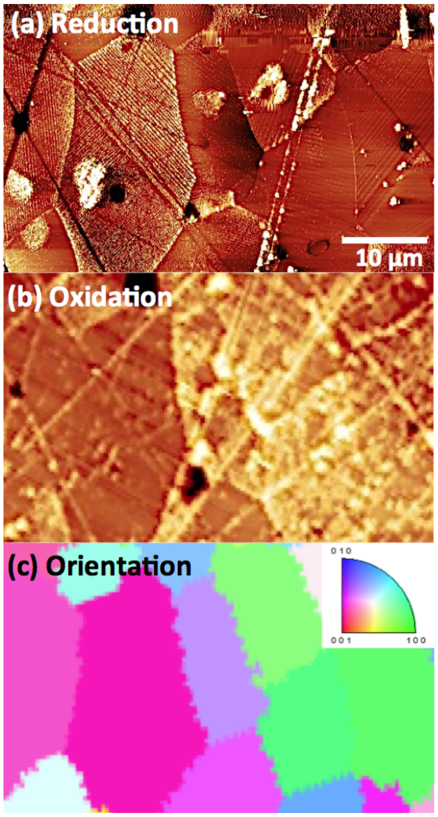

Figure 4.9. Topographic AFM image of the $BiVO_4$ surface after a photochemical reaction (a) after silver reduction, (b) after lead oxidation, and (c) orientation map of the same area colored by orientation. The topographic vertical contrasts of (a) and (b) are 110 and 220 nm, respectively. The field of view is 30 µm x 50 µm.

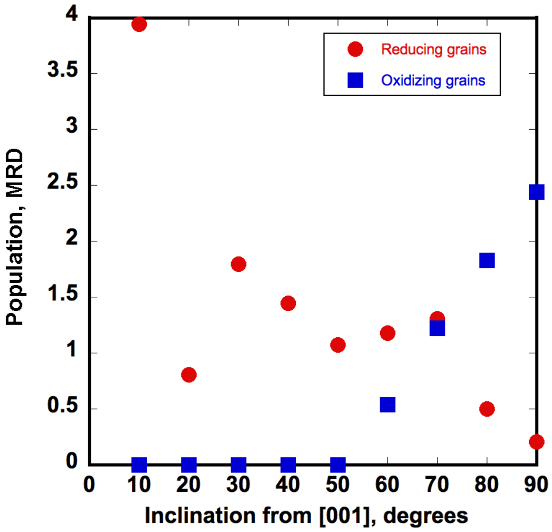

Figure 4.10. The orientation distribution of grains with high reactivity for reduction (red circles) and oxidation (blue squares), as multiples of the random fraction.

Overall, the present results are consistent with the results from the polygonal crystals studied by Li *et al.*[20], bearing in mind that the current experiment probes all orientations. For example, (001) is for silver reduction. In addition, while Li's result indicate that (101) is for oxidation (60° from [001]), the current results indicate that there are other surfaces 60° from [001] that also favor for lead oxidation. However, the current results also showed that it is possible for silver reduction and manganese oxidation to occur on any oriented surfaces.

4.4 Discussion

The reduction and oxidation results demonstrated that the photochemical reactions on sintered polycrystalline $BiVO_4$ surface under visible light were spatially selective. Under illumination, $BiVO_4$ absorbed light and then generated charge carriers of electrons and holes as shown in Eq. 4.1. The charge carriers travel to surfaces and participate in the redox reactions. Specifically, electrons are involved in a reduction reaction, while holes participate in an oxidation reaction. In the reduction experiment, Ag ion was reduced to insoluble Ag metal (Eq. 4.2) which was deposited on the surface. The Ag deposit would mark where the reduction reaction occurred, whereas O_2 gas, the product of water oxidation (Eq. 4.3) would not be characterized. In the oxidation experiments, electrons are used to reduce the sacrificial agent of IO_3- (Eq. 4.4), while holes contribute to the oxidation of Pb^{2+} (Eq. 4.5) or Mn^{2+} (Eq. 4.6) depending on the precursor solution.

$$BiVO_4 + h\nu \rightarrow h^+ + e^- \qquad (4.1)$$

$$Ag^+ + e- \rightarrow Ag \qquad (4.2)$$

$$2O^{2-} + 4h+ \rightarrow O_2 \tag{4.3}$$

$$IO_3- + 6e- \rightarrow I- + 3/2\ O_2 \tag{4.4}$$

$$Pb^{2+} + 2h+ \rightarrow PbO_2 \tag{4.5}$$

$$Mn^{2+} + xH_2O + (2x-2)h^+ \rightarrow MnO_x + 2xH+ \tag{4.6}$$

The energy level diagram of $BiVO_4$ including the redox potentials for the reduction and oxidation experiments is shown in Fig. 4.11.

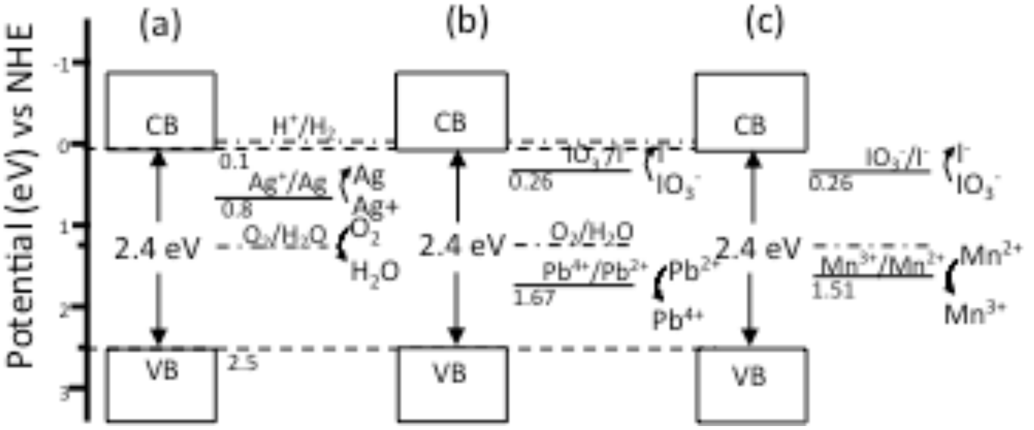

Figure 4.11. The energy level diagram showing the band edge positions compared with the redox potentials (a) in $AgNO_3$ solution, which Ag^+ accepts electrons for reduction (b) in $Pb(NO_3)_2$ solution coupling with IO_3^-, and (c) in $MnSO_4$ solution coupling with IO_3^-, which IO_3^- accepts electrons for reduction and Pb^{2+} and Mn^{2+} accepts holes for oxidation.

In particular to the oxidation experiments, the different dispersion of Pb^{2+} and Mn^{2+} oxidation products was observed. This may arise due to the difference of the overpotentials. The overpotential is an extra energy that can accommodate the carrier transport: higher overpotential drives holes to the O_2/H_2O potential more easily. Thus, it is likely that the Mn^{2+}oxidation will have a wider range of active orientations than the Pb^{2+} oxidation because of its higher overpotential.

The photochemical reactivity of $BiVO_4$ observed here is consistent with that observed by Li *et al.*[20] The prior work considered polygonal particles bounded by (001), (101), and (011) faces. The (101) and (011) faces were not discriminated in the previous work and appeared to have the same reactivity, an observation consistent with the current work. Li *et al.*[20] found reduction exclusively on the (001) surface and oxidation exclusively on the other two facets. Our results agree in the sense that (001) favors reduction of silver ions and surfaces inclined by more than 50° favor oxidation of lead (II) ions. However, the reactivity was not exclusive in our experiments. Surfaces close to (001) had the highest reactivity, but all surfaces could reduce some Ag (see Fig. 4.4), even if it was a small amount. By examining all possible orientations, it was found that surfaces perpendicular to (001), or those with indices of the type (*hk*0), have the highest photochemical reactivity for both lead and manganese oxidations.

There are a few possible experimental differences that should be mentioned. For example, the surfaces on the sintered polycrystalline specimen have much larger areas for each orientation than on the small particles; the ceramic grains are usually several tens of microns in diameter. It is difficult to imagine that photogenerated electron-hole pairs travel to different grains to react. It is more likely that a surface that reduces Ag is also oxidizing water at the same rate and a surface that oxidizes Pb^{2+} is also reducing IO_3^- at the same rate. This is made possible by the ferroelastic domains in the grains, which appear polar in PFM images, providing closely spaced sites for oxidation and reduction on all grains (see Chapter 5).[126] The more exclusive oxidation and reduction behavior on the small single crystals might be because the oxidation and reduction sites are separated by only a few hundred nanometers and the photogenerated carriers can traverse these distances.

The mechanism for the anisotropic reactivity is not known with certainty. Previous investigations on the anisotropic photochemical reactivity of oxides have suggested the importance of both bulk and surface properties. For example, Giocondi *et al.*[27] attributed the anisotropic photochemical activity of $SrTiO_3$ polycrystals to differences in the energies needed to create electron-hole pairs with momentum along different crystallographic directions. They also argued that surface polarity played a role.[129] Past studies of the anisotropic properties of hematite proposed that higher photocurrent densities on prismatic surfaces (in comparison to basal surfaces) was the results of greater electronic conductivity parallel to the basal plane. This factor could improve the electron-hole separation and therefore could decrease recombination, leading to greater photocurrent densities. The conductivity may also play a role in $BiVO_4$. Based on DFT calculations, it has been reported that electrons and holes have higher drift velocity for the (001) surface.[28] This would bring more of the majority carrier (electrons) to the (001) surface and promote reduction. Under these circumstances, the minority carrier (hole) population would be very low. The localization of oxidation reactions to perpendicular surfaces may be because the comparatively lower electron populations at these surfaces lead to higher hole lifetimes.

The findings described here make it possible to propose an ideal particle shape for a $BiVO_4$ catalyst. The particle would not have to be fully faceted. Instead, it could be cylindrical with two flat (001) faces (the best surfaces for reduction) and any combination of (*hk*0) surfaces, oriented perpendicular to (001) faces, which are all active for oxidation. The relative areas of the surfaces would be adjusted so that one half of the reaction would not limit the other. For example, if reduction were fast compared to oxidation, the particle would be acicular and, if reduction were sluggish compared to oxidation, a flatter disc shaped particle would be desirable.

4.5 Conclusions

The photochemical reduction of Ag^+ is strongly favored on $BiVO_4$ (001) surfaces. However, Ag^+ can be reduced on all orientations, with the rate of reduction decreasing with increasing inclination from the (001) surface. The oxidation of Pb^{2+} and Mn^{2+} are strongly favored on (*hk*0) surfaces that are perpendicular to (001). Surfaces within 50° of (001) have a much lower activity for the oxidation of Pb^{2+}, which is in agreement with the oxidation of Mn^{2+} as the surfaces became more active when the inclined angle of the surface increased. As a result, the ideal $BiVO_4$ particle to promote photochemical reactions would be comprised of (001) faces and any combination of (*hk*0) surfaces, oriented perpendicular to (001) faces.

Chapter 5

STUDY 2:

Domain-Selectivity of Photochemical Reactions

5.1 Chapter overview

Other than the effect of orientation reported in the previous chapter, the ferroelastic domain structure was also observed to affect the reactivity. Recently, semiconductors with polar domains have received significant attention because their internal fields effectively separate photogenerated electron-hole pairs and thereby reduce recombination.[15,16,130,131] Domains of opposite polarization create unbalanced charges in spatially localized areas where the domains intersect the surface. As a result, electrons are attracted to positively terminated domains where they promote reduction reactions and holes are attracted to negatively charged domains where they promote oxidation.[57,132] The separation of photogenerated carriers and redox products increases reactivity by limiting recombination and back reactions; the spatial localization can also be used to create well-defined nanostructures through site specific reactions.[133] So far, this phenomenon has been observed only in materials that have polarity deriving from their non-centrosymmetric structures, such as ferroelectrics. One survey identified just over 500 oxide compounds that met the symmetry requirements for polar behavior,[134] a relatively small number considering the possible ternary, quaternary and more complex stoichiometries that might be formulated.

Herein, a novel charge-separation method that arises from charged surfaces of centrosymmetric $BiVO_4$ is uncovered. Surprisingly while investigating orientation-dependent reactivity, an anomalously domain-dependent reactivity was observed in sintered polycrystalline $BiVO_4$, whose domains are supposedly non-polar. This anomaly has never been found in materials with a centrosymmetric structure. There are, however, polar phenomena that can occur in any materials, including centrosymmetric oxides. Such polar phenomena are known collectively as flexoelectric effects, which couple a strain gradient and internal polarization.[59,69,70] While thin film ferroelectrics have been reported to have large flexoelectric effects,[61] the effect is thought to be small in bulk materials and especially in centrosymmetric materials.[59] Because symmetry is broken by surfaces, they provide a mechanism for the relaxation of internal stress that arises both from microstructural discontinuities and from the discontinuous bonding at the surface.[29,135] In general, any relaxation of stress at the free surface might create a strain gradient and impart flexoelectricity in an otherwise non-polar material.

$BiVO_4$, when cooled below 255 °C, undergoes a ferroelastic transition from the tetragonal scheelite structure to the monoclinic fergusonite structure (I_2/b, $\mathbf{a}$ = 5.1935 Å, $\mathbf{b}$ = 5.0898 Å, $\mathbf{c}$ = 11.6972 Å, γ = 89.613°).[87,136] This ferroelastic transformation leads to two permissible domains that form to partially compensate for the transformation strain that occurs when the crystal changes shape.[89,136,137] As a result, such a transformation strain may cause flexoelectricity in monoclinic $BiVO_4$, resulting in the heterogeneity of the photochemical reactions by domains.

This chapter will mainly present the heterogeneity of the photochemical reactions affected by ferroelastic domain structure. Specifically, some ferroelastic domains are more active for reduction than others. Similarly, this domain-selectivity can also be found for oxidation reaction as well. These findings are promising and exceptional for centrosymmetric materials because they indicate improved spatial separation of the reactions and charge carriers. This could potentially open up more material choices for efficient photocatalysts, plus a possibility to expand centric materials into more practical applications. Thus, a possible explanation and implications of this anomalous reactivity will be discussed in this chapter.

5.2 Experimental method

The sintered polycrystalline $BiVO_4$ sample prepared for the study in Chapter 4 was also used in this study. The topography of the sample's clean surface was first examined by atomic force microscopy (AFM), recorded using SolverNext NT-MDT AFM under tapping mode. Piezoresponse force microscopy (PFM) was used to evaluate the piezoresponse of the surface.

The marker reactions were carried out to determine the locations of the reactions using an aqueous solution of $AgNO_3$ and of $MnSO_4$ for reduction and oxidation experiment, respectively. For the photochemical reduction of Ag, the surface was covered with a 0.115 M aqueous $AgNO_3$ solution. The solution was contained in a viton o-ring and closed at the top surface with a glass cover slip. The sample was then exposed under a blue LED (emission wavelength centered at 470 nm) for times ranging from 1 to 30 min. The LED was driven by a DC power supply at a fixed current of 750 mA, corresponding to a power of about 3 W. The shorter times were used for AFM experiments, which are very sensitive to reaction product on the surface, and longer times were used for the XRD and EDS experiments, which are less sensitive. A control experiment was conducted under the same conditions, but without illumination, and no silver deposits formed on the surface. Then, the reactivity was observed by imaging surface topography after reduction using AFM. Afterwards, the sample surface was gently wiped off with methanol-wet cotton swabs and ultrasonically cleaned in acetone and methanol to remove silver deposits prior to the oxidation experiment.

Similarly, the photochemical oxidation experiment was conducted using the same setup of the reduction experiment. However, the solution was changed to 0.115 M aqueous $MnSO_4$ solution with the addition of 0.23 M $NaIO_3$ as an electron acceptor. It should be noted that $MnSO_4$ and $NaIO_3$ can react and result in insoluble $Mn(IO_3)_2$, so the mixture solution of $MnSO_4$ and $NaIO_3$ was filtered to get clear supernatant before used in the oxidation experiment. The reaction time for the oxidation is also different from the reduction; the sample was exposed under blue LED for 5 mins. Then, after reduction and oxidation experiment, the surface topography of the same area was imaged by AFM for comparison.

5.3 Results

5.3.1 Ferroelastic domain investigation

Fig. 5.1 is an example of AFM images showing a common surface topography obtained from the sintered polycrystalline $BiVO_4$ sample after annealing. When the polished surface was examined microscopically, the previously reported parallel lamellar structures, which correspond to ferroelastic domains, were obvious.[137,138] The AFM image in Fig. 5.1 shows portions of three misoriented crystals, separated by grain boundaries, each with lamellar contrast corresponding to the domain microstructure. The orientation of domain patterns usually changes across grain boundaries. Typically, each grain would contain a set of apparent domains in AFM images;

however, there were some grains or area of a grain that had a complicated domain structure. Specifically, some grains may comprise multiple domain structures or cross-hatched patterns of domains as shown in a dashed box in Fig. 5.1. Also, it is possible to find grains with no observable domain contrast. Similarly, parallel lamellar patterns of the domains were able to observe via scanning electron microscopy (SEM) with backscatter electron (BSE) mode as shown in Fig. 5.2. It should be noted that the widths of observable domains are in a range of submicrons.

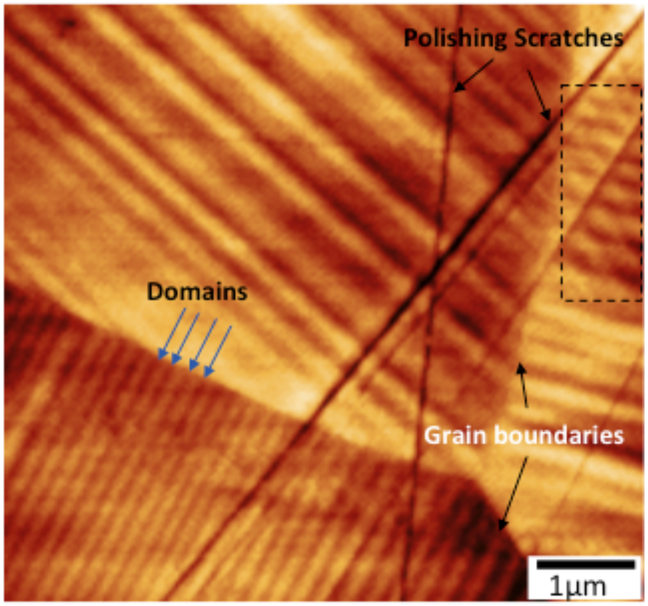

Figure 5.1. AFM topography of the clean surface of bulk $BiVO_4$. Arrows point at some common surface features: polishing scratches, grain boundaries and domains. The vertical bright to dark contrast is 15 nm.

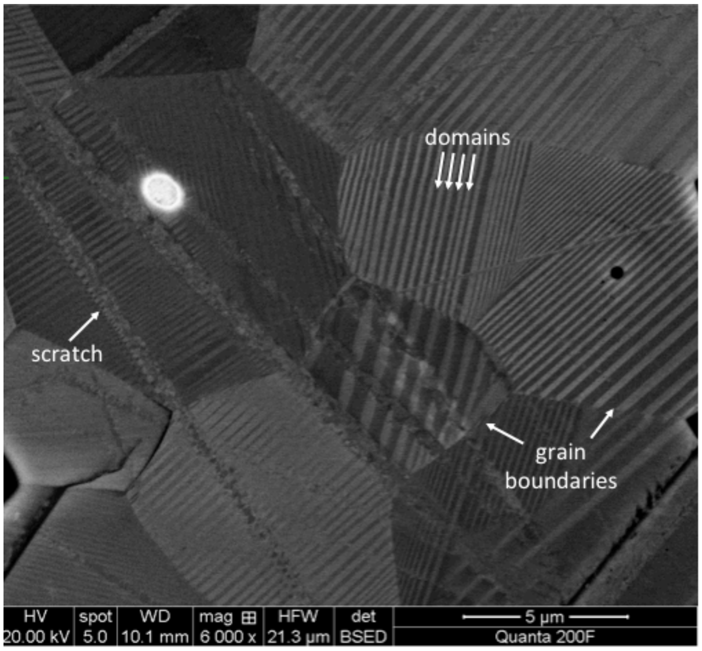

Figure 5.2. SEM image (BSE contrast) reveals the existence and alignments of ferroelastic domains.

5.3.2 Domain-selectivity of photochemical reactions

When silver cations from solution are photochemically reduced to silver metal on the surface,[139] the silver preferentially forms only on certain domains; this is illustrated by the image in Fig. 5.3(b). Compared with the surface topography before reduction shown in Fig. 5.3(a), the silver deposits, which are the large topographic features in Fig. 5.3(b), appear white. In the central grain with contrast from multiple domains, only one parallel set of domains (the wider ones) has reduced silver and the reduction occurs only on every other domain. This is a characteristic of all observations: when domains photochemically reduce silver, it is every other domain that is active for reduction.

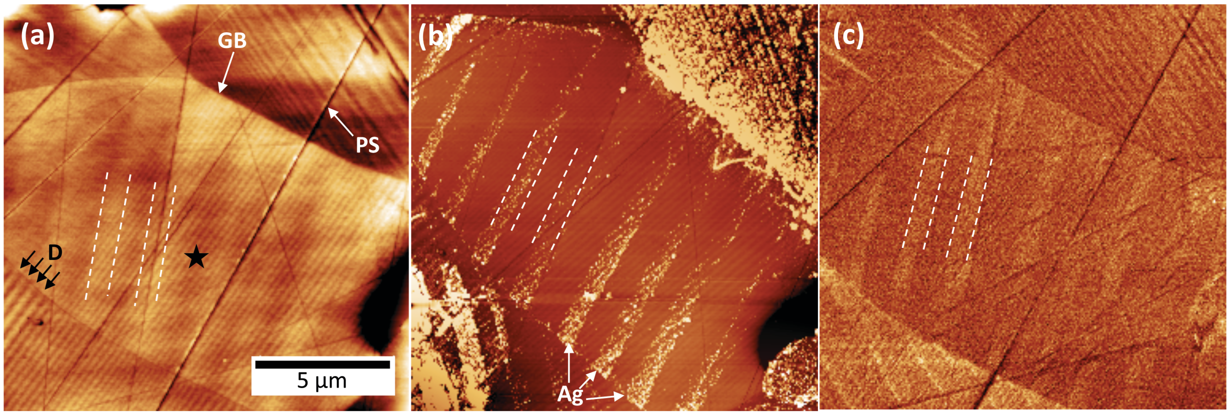

Figure 5.3. (a) AFM topographic image before reaction (b) topography after photochemical reaction and (c) out-of-plane PFM magnitude before reaction. The vertical bright to dark contrast is 30 nm (a), 50 nm (b), and 180 pA (c). The dashed white lines indicate the same domain walls (domains) in each image, D illustrates domain contrast, GB a grain boundary, and PS a polishing scratch. In (b), the locations of three domains that reduce silver are indicated by the label Ag.

The PFM image in Fig. 5.3(c) shows clear contrast from the ferroelastic domains. When multiple sets of parallel domains are present, it is typically only one set preferentially reduces silver. Piezoresponse from a polycrystalline (centric) $SrTiO_3$ surface has previously been reported, but in that case it was a grain-by-grain response.[135] The correlation observed here between the piezoresponse of ferroelastic domains and photochemical reactions in a centric material is unique. Similar behavior was observed on dozens of additional grains that were examined. Two additional examples (illustrated in Fig. 5.4) show common phenomena: inhomogeneous Ag reduction in Fig. 5.4(c) and 5.4(f), even though the piezoresponse in Fig. 5.4(b) and 5.4(e) appears to be relatively homogeneous.

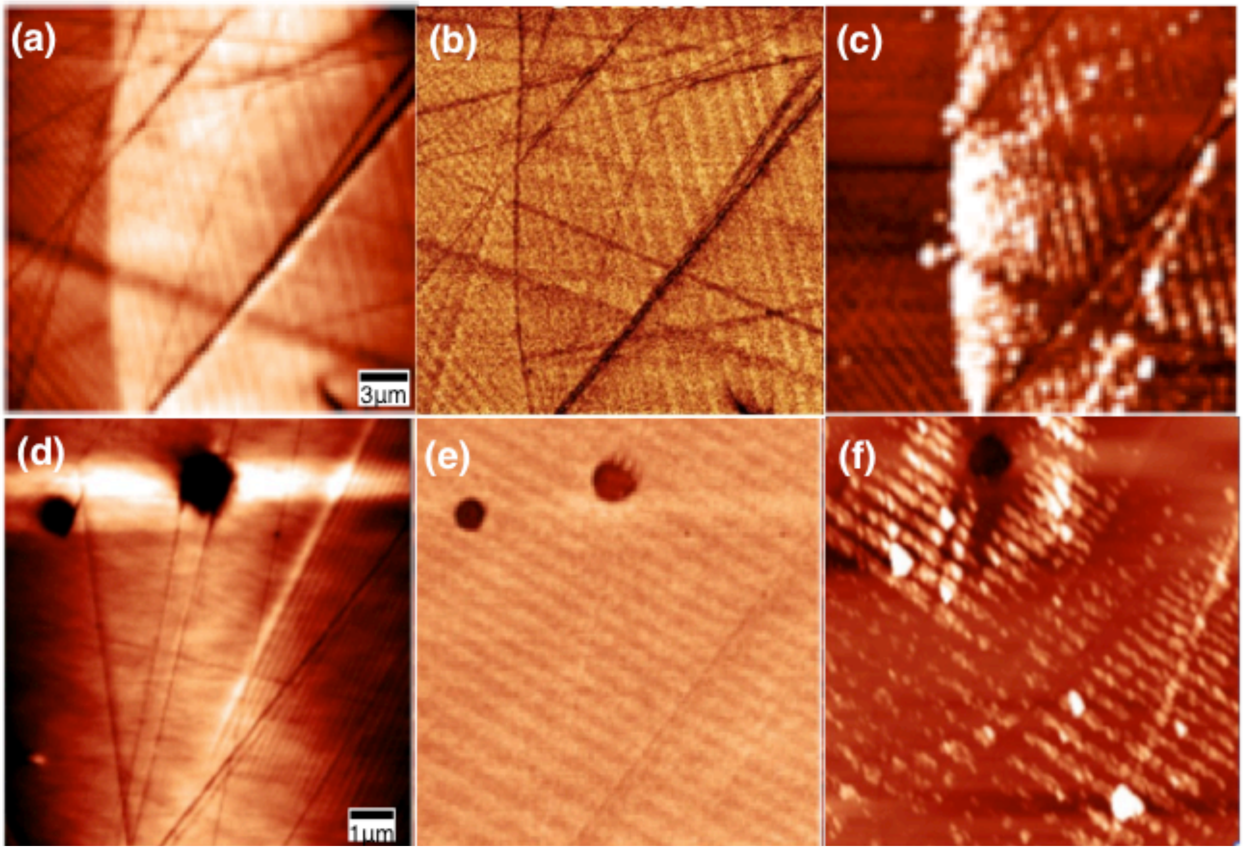

Figure 5.4. (a), (d) Topographic images of different areas before reaction. (b) and (e) are out-of-plane PFM images of the areas in (a) and (d) respectively, before the reduction reaction. (c), (f) Topographic images of different areas after a 1 min photochemical reaction of the areas in (a) and (d) respectively. Labels indicate reactive (R) grains and non-reactive (NR) grains. The vertical scales are (b) = 66.5 pA, ((c) = 40 nm, (e) = 120 pA, f) = 65 nm.

Fig. 5.5 shows the effect of silver reduction on a sintered polycrystalline $BiVO_4$ surface that has no apparent domains. Even though a grain has no apparent topographic domains (Fig 5.5(a)), the domain-selectivity of photochemical reduction can still be observed. After reduction (Fig. 5.5(b)), silver was also formed in patterns of lamellar strips similar to the domain pattern.

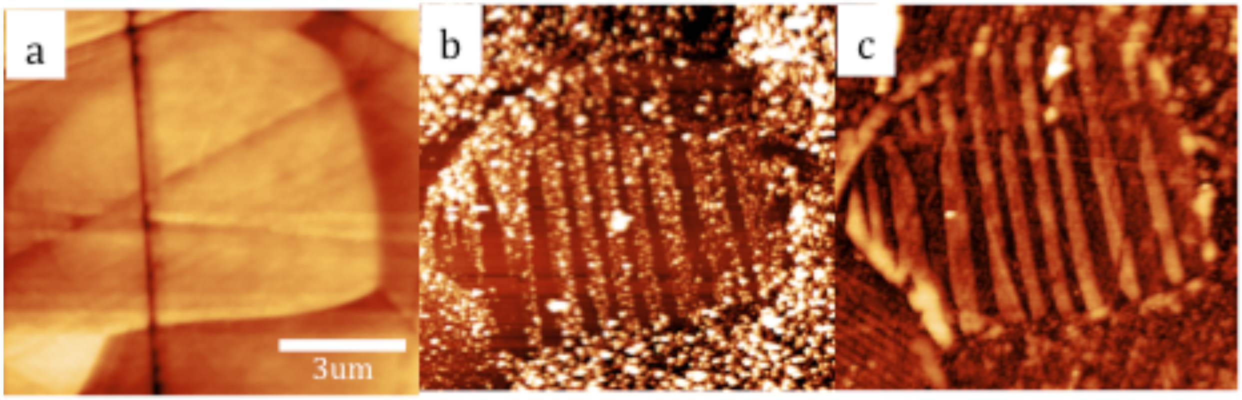

Figure 5.5. Domain selectivity of photochemical reduction (a) surface topography before reactions, (b) the surface after reduction, and (c) the surface after oxidation. The image regions in (a), (b) and (c) are the same. The vertical scale are (a) = 20 nm, (b) = 80 nm, and (c) = 110 nm.

Just as domain selectivity was apparent in reduction, Figure 5.5(c) shows that it was also apparent in oxidation. It should be noted that because the Pb^{2+} oxidation did not occur on every grain, while the Mn^{2+} oxidation occurred on every grains. Thus, in this study, the result of the Mn^{2+} oxidation was used to show the domain selectivity. After oxidation, Mn^{2+} ions from an aqueous $MnSO_4$ solution were oxidized to MnO_x particles. The reactivity in oxidation has similar patterns as the one in reduction: only one set of domains was reacted and it happened on every other domain.

When compared the surface topography after reduction (Fig. 5.4(b)) and after oxidation (Fig. 5.4(c)), interestingly the domain selectivity in reduction and oxidation was complementary to each other. This complementarity is strong evidence that implies the existence of an internal force which can drive electrons and holes to different domains, and lead to domain-selectivity of the reactions. The domain selectivity and the complementary reactions are essentially the same as what has been observed in non-centrosymmetric ferroelectrics including $BaTiO_3$,[140] $BiFeO_3$,[141] $(Ba_xSr_{1-x})TiO_3$,[18] and PZT,[142,143] but for $BiVO_4$, the crystal structure is centrosymmetric. It should be also noted that although bulk $BiVO_4$ is centric and non-piezoelectric, the ferroelastic domains at the surface are piezoresponsive.

5.4 Discussion

The domain-specific photochemical reduction of silver on ferroelectric structures, such as $BaTiO_3$[140] and $BiFeO_3$,[141] has been explained as a natural consequence of unscreened dipolar charge in each domain.[57,132] As illustrated in Fig. 5.6, the surface, of which a positive polarization oriented toward, can reduce the energy of the conduction band edge at the surface, making it easier for electrons to reach the surface and reduce cations in solution.[18,144] Conversely, a negative polarization oriented toward the surface increases the energy of the conduction band edge at the surface, making it less likely that electrons will reach the surface.

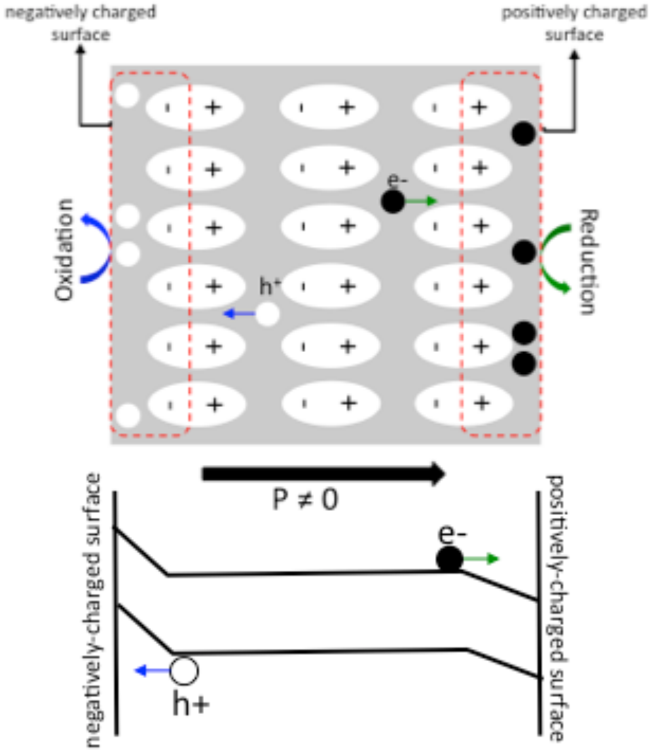

Figure 5.6. Dipole moments lead to the polarity of the surfaces. The dipole moments also affect the bending of the band structure at the interface; the lower schematic shows the corresponding band structure.

Based on the observed results, it is speculated that an internal polarization would be induced in the sample and lead centric materials to behave like non-centrosymmetric polar materials. While this effect, known as a ferroelectric effect, is commonly seen in non-centrosymmetric ferroelectric materials, this effect would be crystallographically prohibited in centric $BiVO_4$ due to the crystal restriction. One theory that can explain this piezoelectric or ferroelectric-like behavior in centric materials is the so-called flexoelectricity.[59] Flexoelectricity is an electromechanical coupling similar to piezoelectricity. However, instead of associated with a strain, flexoelectricity needs a strain gradient to break the symmetry. As a result, there is no crystallographic constraint for the flexoelectric effect.

An inhomogeneous strain is a key component that leads to the flexoelectric effect. Such a strain gradient can arise from many mechanisms, but here two main contributions, which are particularly related to a sintered polycrystalline structure, will be deliberated as follows:

(1) A strain gradient is caused by a relaxation of undercoordinated atoms at the surface.

The first contribution is the relaxation of atomic positions because of the broken bonds at the free surface. The existence of a free surface allows stresses in a sintered polycrystalline ceramic to relax. Ions near the surface will relax by different amounts, depending upon their proximity to the surface, with those that are closest to the surface moving the most and those further away moving the least, schematically illustrated in Fig. 5.7. To the extent that these relaxations lead to gradients in the strain, this can be considered the flexoelectric effect. In other words, as long as these movements are non-uniform, it is possible to develop a net dipole moment in the near surface region. As a result, this likely contributes to the observed pattern of surface polarization and causes $BiVO_4$ to behave (in the near surface region) just as a ferroelectric would. This behavior can be referred to as a contribution of surface piezoelectricity.[59,60]

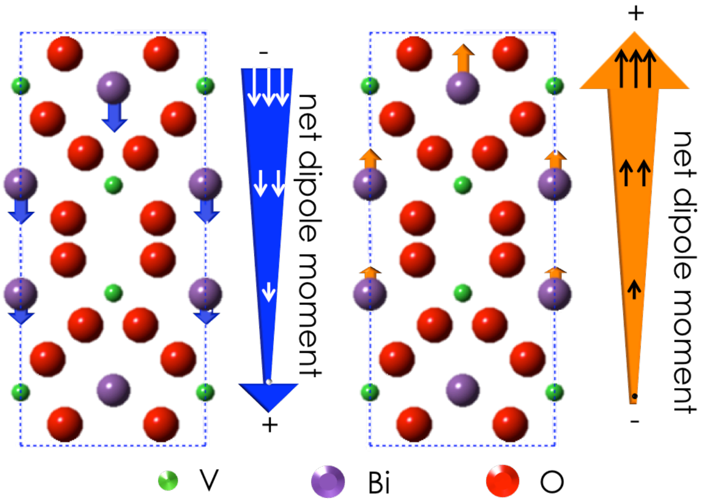

Figure 5.7. Strain-gradient-induced symmetry-breaking effect by the free surface, leading to an inhomogeneity of atomic displacements

(2) A strain gradient arises from the relaxation of the transformation strain associated with domains in the ferroelastic microstructure.[59,69,70]

The second mechanism is contributed to static flexoelectricity. This contribution should be considered additive rather than independent. The tetragonal-to-monoclinic phase transformation leads to shape changes within each grain of the sintered polycrystalline sample. Because each grain has a different orientation, it changes shape by different amounts in different directions, while still being constrained to maintain continuity at all of the interfaces, except the free surface. The domain structure forms to reduce the transformation strains, but does not completely eliminate them. In fact, the relief of elastic strain will be inhomogeneous because of the free boundary condition. Some domains possess tension and some possess compression, and this will cause gradients in strain and, therefore, a polarization. Evidence for this strain relief is found in the observed surface topography.

One can speculate about the relative influence of the two contributions. The relaxation of undercoordinated atoms at the surface would be expected to be relatively uniform for a given orientation and not reverse itself in neighboring domains. However, the inhomogeneous strains that arise from the domain microstructure will change polarity when the stress changes from tensile to compressive across neighboring domain boundaries as shown in Fig. 5.8. This is the likely origin of the observed alternation in the photochemical reactivity and the contrast in the PFM images. In the cases where positive polarization is pointed toward the domain surface, the conduction band edge is bent downward and electrons can be transported to the surface where they can reduce silver. In domains with weak or opposite polarization, electrons cannot reach the surface and the oxidation reaction is observed, illustrated schematically in Fig. 5.9.

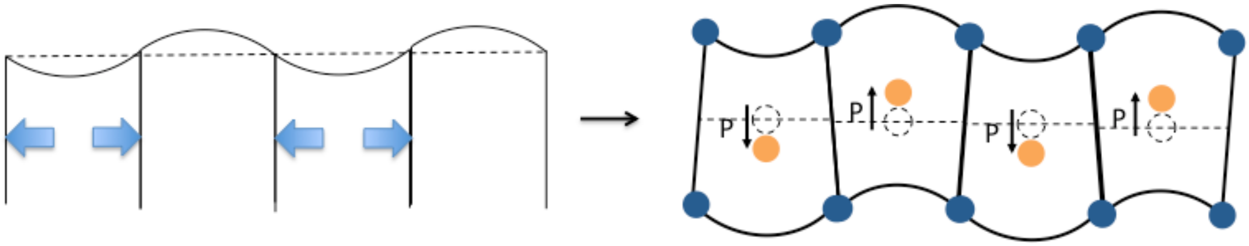

Figure 5.8. Inhomogeneous strain from the transformation leading to the alternation in the polarization.

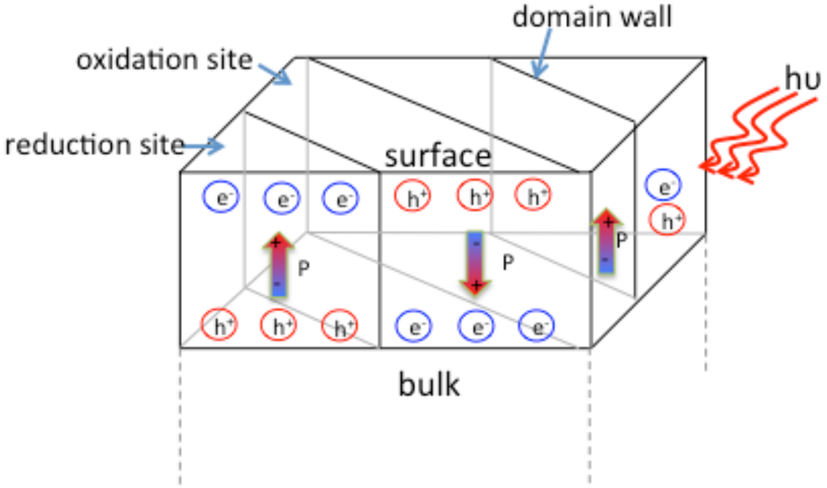

Figure 5.9. Induced polarization in the surface layer of centric materials causes an opposite polar surface and therefore the domain-selectivity of photochemical reactions.

5.5 Conclusions

It was found that ferroelastic domains of a $BiVO_4$ surface can promote the domain selectivity of silver reduction from an aqueous $AgNO_3$ solution and of manganese oxide oxidation from an aqueous $MnSO_4$ solution. Additionally, there was a domain-complementary reactivity between the reduction and the oxidation. The domain-specific photochemical reactivity and its complementary reactivity are consistent with what has been observed in ferroelectric materials. While the equilibrium structure has a center of symmetry and should not have locally polarized domains, the flexoelectric effect in the near surface region creates regular patterns of domains that are piezoresponsive and sometimes aligned to promote the transport of photogenerated electrons to the surface to reduce silver. The polar response of $BiVO_4$ suggests the range of possible materials that may promote photogenerated charge carrier separation and a possibility for engineering centric materials into more functionality.

Chapter 6

STUDY 3:

Effect of ferroelastic domain structure on photochemical properties of $BiVO_4$

6.1 Chapter overview

Photo-generated electron-hole recombination is a crucial problem in photocatalytic materials and it is also a main problem limiting the performance of the $BiVO_4$ photocatalyst.[118] Internal fields in photocatalysts are integral to charge separation, arising from surface terminations and ferroelectric phenomena in single-phase materials, and polymorph or p–n junctions in multi-phase samples.[16] Some of these methods have already been used to introduce internal fields in $BiVO_4$. For example, heterojunctions between Co_3O_4 and $BiVO_4$ have shown notable improvements in the rate of oxidation reactions.[14,119,145,146] Surface orientation differences also impact the overall activity in $BiVO_4$ for water oxidation[120] and control the spatial selectivity of photochemical marker reactions.[20,21,28,105] In marker reaction experiments, reduction appears favored on (001) surfaces and oxidation appears favored on surfaces away from the (001).[20,21,105,120] While the origin of these observations can be associated with different internal fields at or between different facets,[20,21,28,105,120] other factors are known to affect the reactivity and it is generally thought that a single simple parameter might not be sufficient to describe the orientation dependence of the reactions.[28] Whatever the origin, it is important to consider the orientation of the surface when comparing the reactivity of different samples.

In ferroelectrics, domains of different polarization states intersect surfaces and exhibit different photochemical activities. Domains with positive surfaces attract electrons and promote photo-reduction, while domains with negative surfaces attract holes and promote photo-oxidation.[16,57] The ferroelectric contribution to surface reactivity can modulate or even overwhelm orientation-dependent reactivity differences. Unfortunately, most ferroelectrics have wide band gaps that do not absorb significant portions of the solar spectrum. The narrow gap ferroelectric $BiFeO_3$ exhibits domain selective reactivity when illuminated with visible light.[141] Recently, I discovered that the centrosymmetric ferroelastic monoclinic $BiVO_4$ can also exhibit spatially selective visible light stimulated surface photoreactivity that correlates to the ferroelastic domain structure.[126] Moreover, the domains generate contrast in piezoresponse force microscopy (PFM) that correlates to the reactivity, exactly like polar domains in ferroelectrics, yet polarity is not a bulk property of centrosymmetric crystals.[126] In addition, oxidation and reduction occur on distinct subsets of the domains, a property referred to here as "complementarity." The implication is that the ferroelastic domains in monoclinic $BiVO_4$ have internal fields capable of improved charge separation and reduced recombination.[147] Although, it remains to be demonstrated if the ferroelastic domains lead to improved reactivity.

To investigate whether ferroelasticity leads to improved reactivity, I compare the reactivity of monoclinic (ferroelastic) and tetragonal (non-ferroelastic) $BiVO_4$-based samples with similar surface orientations, over all of orientation space. The stable phase of $BiVO_4$ at room temperature is monoclinic.[99] The ferroelastic transformation from the high-temperature tetragonal phase to the low-temperature monoclinic phase occurs at 255 °C. This transformation temperature can be suppressed by co-doping in the $Na_{0.5x}Bi_{1-0.5x}Mo_xV_{1-x}O_4$ family, where the tetragonal structure is maintained to room temperature for $x \geq 0.10$.[31] Therefore, I fabricated and compared the reactivity for a monoclinic x = 0.05 sample and a tetragonal x = 0.175 sample, focusing on comparing whether domain specific reactivity is observed and if quantitative differences in the overall reactivity could be observed for comparable orientations.

6.2 Experimental method

Monoclinic (x= 0 and 0.05) and tetragonal (x = 0.175) samples of $Na_{0.5x}Bi_{1-0.5x}Mo_xV_{1-x}O_4$ were synthesized by solid-state reaction. Stoichiometric ratios of Bi_2O_3, V_2O_5, $NaCO_3$, and MoO_3 were mixed and then wet ball-milled in ethanol for 24 hours using YSZ as a grinding media. The mixed powder was then put in a drying oven at 80 °C to remove the ethanol, and the dried powder was calcined at 600 °C for 3 hours. The powder was manually reground and calcined several times to obtain fine powders, and the calcined powders were characterized by x-ray diffraction (XRD) to confirm full reaction to the targeted structures. Then, a few drops of PVA was mixed manually with 1 g of fine powder, and the mixture was pressed into a 1 cm-diameter cylindrical-shaped pellet using a hydraulic pressure of 6 metric tons. The green pellet was heated at 500 °C for two hours, to remove the PVA, and was then annealed at 780 °C for 20 hours to obtain a dense sintered ceramic. The surfaces of the obtained ceramics were lapped and polished with SiC papers, followed by polishing with successively finer Al_2O_3 polishing suspensions, until mirror-like surfaces were obtained. Afterwards, the samples were annealed at 300 °C for 1 hour to heal surface damage from the polishing. The polished samples were also measured for their order-of-magnitude electronic conductivity using the van der Pauw technique at room temperature.

All samples were used to photochemically reduce Ag^+. An O-ring was placed on the surface of the specimen and then filled with 0.115 M $AgNO_3$ aqueous solution. A quartz slip was put on top of the o-ring(s) to create a flat and uniform surface for illumination. The undoped sample was tested and illuminated alone. The co-doped samples were tested and illuminated together to remove the possibility that differences in reactivity of the two samples were related to changes in the experimental conditions. Each was placed in an o-ring filled with an identical solution environment, placed adjacent to each other in the center of the illuminated region, and then covered with the same quartz. Samples were illuminated from the topside using a blue LED (λ_{peak} = 470 nm, Philips Lumileds, San Jose, CA), and the set-up was arranged to optimize examination of the initial reactivity using atomic force microscopy (AFM). For the undoped sample, the light source was in contact with the quartz slip, the power was 330 mW (0.75 A and 0.44 V), and the exposure time was 60 s (consistent with our previous studies[105,126]). For the co-doped samples (which were more reactive), the light source was ~ 1 cm above the cover slip, the power was 220 mW (0.5 A and 0.44 V), and the exposure time was 10 or 30 s. After exposure, the sample was rinsed in water to avoid the precipitation of residual $AgNO_3$ and then dried. For the undoped $BiVO_4$, the photochemical oxidation of Mn^{2+} was investigated on the same area where Ag^+ reduction was observed, using identical illumination conditions and a 0.115 M $MnSO_4$ aqueous solution containing $NaIO_3$ as an electron acceptor. Prior to the oxidation experiment, silver deposits were wiped from the sample surface, and the sample was cleaned in an ultrasonic bath of methanol and then acetone, for 5 min each.

After reaction, the surface topography of the samples was imaged using AFM[148] and scanning electron microscopy (SEM). The heights of deposits were measured on 50 grains, and these were used to classify the relative reactivity of each co-doped sample. To obtain the relationship between reactivity and orientation, the surface orientations of grains were quantified using electron backscatter diffraction (EBSD) in a Quanta200 SEM (FEI, Hillsboro, Oregon) equipped with an orientation imaging microscopy (OIM) system. For the co-doped samples, the orientations were measured in a 100 μm x 100 μm area, using a scan step of 0.1 μm. EBSD patterns were automatically collected and indexed by the TSL software.[105] Indexing was carried out using a tetragonal unit cell in the Laue group 4/m with $a = b = 5.1509$ Å and $c = 11.73$ Å, for both the monoclinic and tetragonal samples. The co-doped monoclinic system can be indexed as tetragonal because the distortion between a and b is only 2 % and γ is very close to 90° (as described previously[105]). The raw orientation data was cleaned using procedures in the TSL software,[105] including grain dilation (using 5 °), a grain orientation averaging (using 5 °), and a pseudo symmetry correction (for misorientations of 90 ° around (001) axis). Grains were classified as either being high or low reactivity (the quantitative criteria for these distinctions are described later), and the relative reactivity was plotted as a function of orientation using a stereographic projection.

6.3 Results

To test the hypothesis that the ferroelastic domain structure can enhance the overall photochemical reactivity, the orientation and domain dependent reactivities of two compositions in the co-doped $Na_{0.5x}Bi_{1-0.5x}Mo_xV_{1-x}O_4$ family were compared, one composition with a monoclinic structure (x = 0.05) and the other with a tetragonal structure (x = 0.175). The two samples were initially characterized by XRD. The diffraction patterns as given in Fig. 6.1 were consistent with expectations:[31] the x = 0.05 sample was monoclinic and the x = 0.175 sample was tetragonal.

The ferroelastic domain structure of the polished samples was then investigated. Fig. 6.2 shows surface topography investigated by AFM. Ferroelastic domains can be readily observed as striped patterns inside grains on the surface of the monoclinic ferroelastic sample (Fig. 6.2(a)). Contrarily, no domains can be observed on the surface of the tetragonal sample (Fig. 6.2(b)), as expected. The difference of the domain existence in the co-doped monoclinic sample and the co-doped tetragonal sample can also be observed from SEM micrographs, recorded using back-scattered electron (BSE) contrast, are shown in Fig. 6.3(a) and 6.3(b) for the x = 0.05 and x = 0.175 samples, respectively. BSE contrast is sensitive to ferroelastic domains, which gives rise to the striped patterns inside grains for the monoclinic ferroelastic composition (Fig. 6.3(a)). As expected, no domains can be observed for the tetragonal sample (Fig. 6.3(b)).

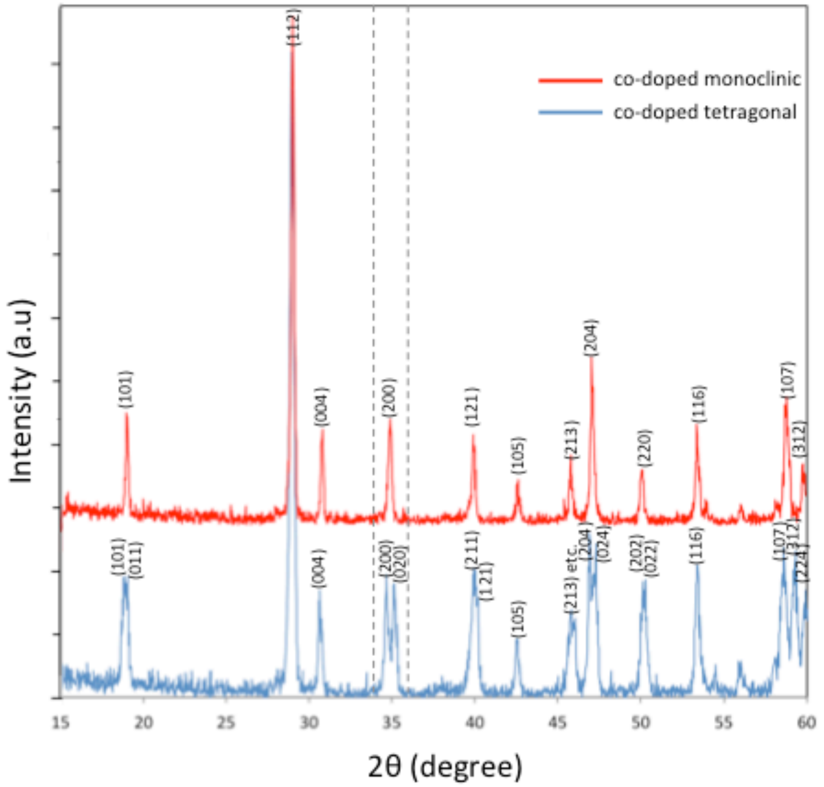

Figure 6.1. X-ray diffraction analysis of co-doped monoclinic $Na_{0.5x}Bi_{1-0.5x}Mo_xV_{1-x}O_4$ (x = 0.05, red) and co-doped tetragonal $Na_{0.5x}Bi_{1-0.5x}Mo_xV_{1-x}O_4$ (x = 0.175, blue).

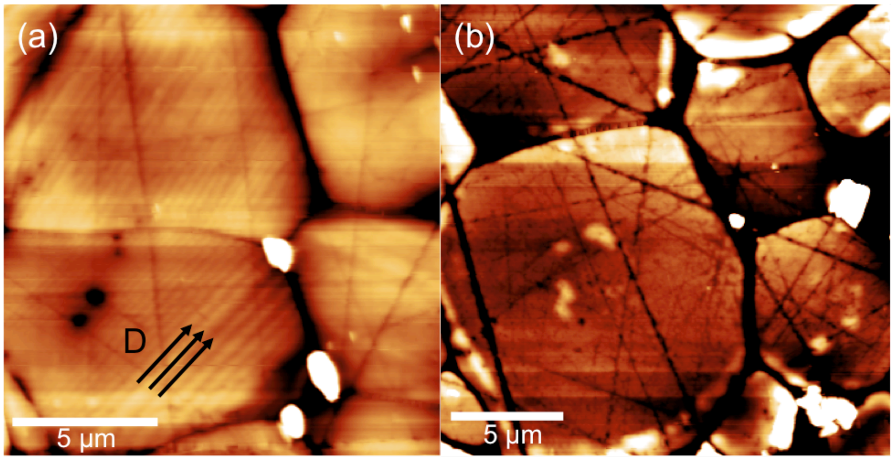

Figure 6.2. AFM surface topography of (a) co-doped monoclinic, and (c) co-doped tetragonal samples. Arrows point to ferroelastic domains denoted ‘D’ observed in the monoclinic samples only. The vertical scale range of (a) and (b) is 35nm.

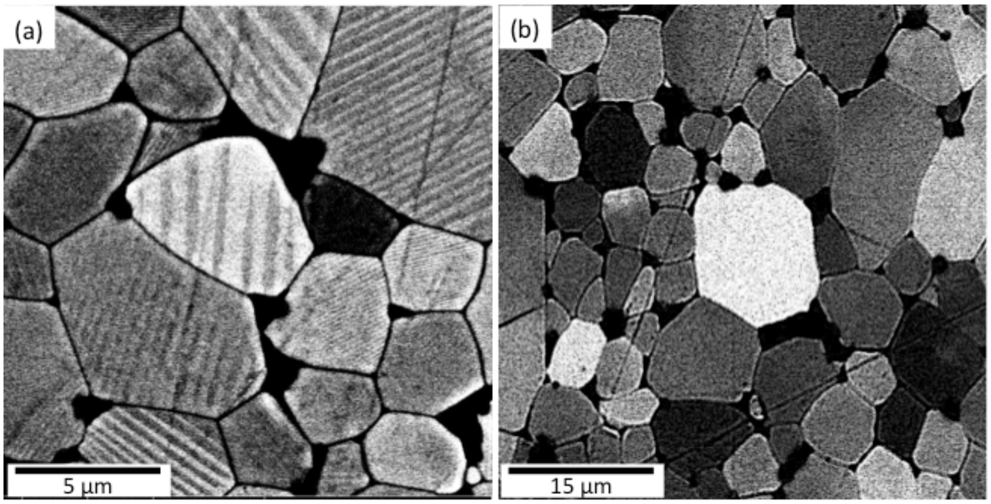

Figure 6.3. SEM micrographs (BSE contrast) of (a) co-doped monoclinic (x = 0.05), and (b) co-doped tetragonal (x = 0.175) $Na_{0.5x}Bi_{1-0.5x}Mo_xV_{1-x}O_4$

The electrical resistivities of the samples were measured. The co-doped samples had similar resistivities of ≈ 10^6 Ω-cm, while the resistivity of the undoped sample was at least (it was too resistive to measure) two orders of magnitude greater at > 10^8 Ω-cm.[51] Co-doping according to the stoichiometry $Na_{0.5x}Bi_{1-0.5x}Mo_xV_{1-x}O_4$ is, ideally, self-compensating: no changes in other defect populations, such as electronic carriers, is required. Nevertheless, the doped samples had conductivities similar to each other and at least 100 times greater than the undoped sample. To avoid complications in interpreting reactivity differences arising from differences in conductivity, we focused on comparing the photochemical reactivity of the co-doped samples of different symmetry but similar conductivity.

In prior work on $BiVO_4$,[126] the domain selectivity for Ag^+ reduction was correlated more strongly to the piezoresponsive nature of domains (measured using PFM) than the surface topography (imaged using AFM). To explore whether surfaces in the $Na_{0.5x}Bi_{1-0.5x}Mo_xV_{1-x}O_4$ family were piezoresponsive, I carried out PFM investigations of the two co-doped samples. The surface topography (plotted as the error signal) of the two co-doped samples are shown in Fig. 6.4(a) and (c), respectively for the monoclinic and tetragonal samples. The piezoresponses (plotted as the phase signal) from the same areas are given in Fig 6.4(b) and 6.4(d), for the monoclinic and tetragonal samples, respectively. In the topographic images, contrast arising from grain boundaries and polishing scratches are clearly observed in both samples. However, contrast arising from ferroelastic domains is observed only for the co-doped monoclinic sample, corresponding to narrow parallel lines within a given grain. In the PFM phase images, weak contrast is observed in both samples from grain boundaries, but strong contrast correlated to domains is observed only in the monoclinic sample. These results indicate that the co-doped monoclinic $x = 0.05$ sample is similar to undoped monoclinic $BiVO_4$,[126] both monoclinic samples having piezoresponsive (polar) ferroelastic domains at their surfaces (these samples are directly compared in Fig. S.5, Appendix 4). The co-doped tetragonal sample, however, does not have ferroelastic domains and has no clear piezoresponsive regions at the surface.

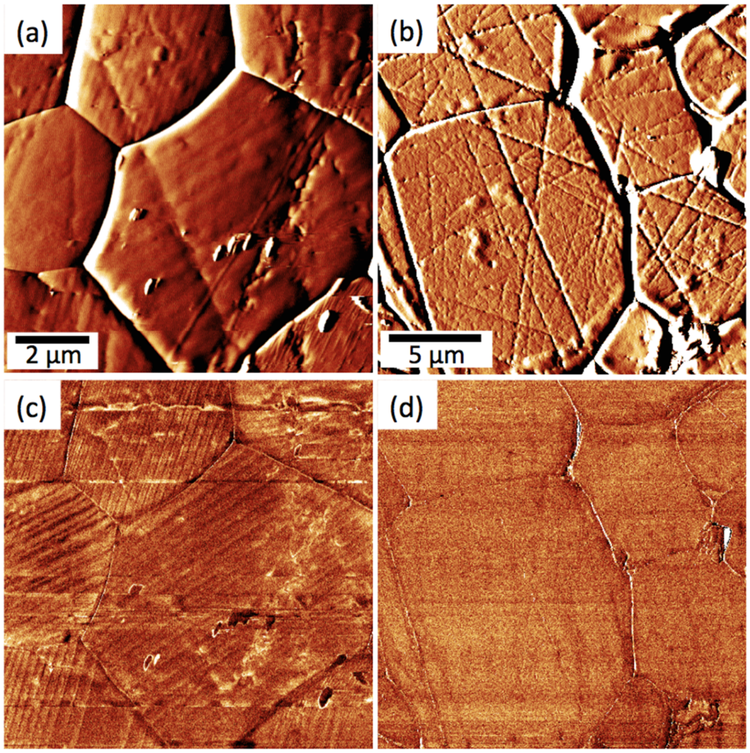

Fig 6.4. Topographic AFM images of the (a) monoclinic x = 0.05 and (c) tetragonal x = 0.175 $Na_{0.5x}Bi_{1-0.5x}Mo_xV_{1-x}O_4$, each plotted as error signals with a vertical scale of 0.2 nA. (b) and (d) are PFM phase images from the same areas as given in (a) and (c), respectively. The range of the vertical scale for the PFM images ((b) and (d)) is 2.4 °.

Example AFM topographs after photochemical reduction of Ag^+ (using a 30 s exposure) are given in Fig. 6.5(a) and 6.5(d) for the monoclinic x = 0.05 and tetragonal x = 0.175 sample, respectively. Silver deposits were found on the surfaces of both co-doped samples, though the amount of silver varied from grain to grain. This is consistent with an orientation dependent reactivity, similar to that reported for the undoped $BiVO_4$ sample.[105] The local surface orientation, determined using EBSD, from these same areas is shown in Fig. 6.5(b) and 6.5(e) for the x = 0.05 and 0.175 samples, respectively. The topographic height profiles of deposits along the dashed lines in Fig. 6.5(a) and 6.5(d) are shown in Fig 6.5(c) and 6.5(f), respectively. I used these height variations to quantify the relative reactivity for grains within each sample. Because the deposition rates on the co-doped monoclinic and co-doped tetragonal samples are different, the criteria for classifying the reactivity for both samples are also different. For the co-doped $x = 0.05$ monoclinic sample, the deposit heights were generally higher, so grains with deposits greater (less) than 20 nm in average height were classified as having high (low) reactivity. For the co-doped $x = 0.175$ sample the average deposit heights were generally lower, and grains with deposits greater (less) than 10 nm height were classified as having high (low) reactivity. The lines in Fig. 6.5(a) and 6.5(d) were chosen such that they traversed grains classified as having high reactivities (H in the images) and low reactivities (L in the images), for both samples. It should be noted here that, for the surfaces on the monoclinic sample classified as low reactivity, such as the grain marked *L* in the lower left of the image, the spatial distribution is reminiscent of the ferroelastic domains. No domains were observed on the tetragonal sample. The domain specificity will be discussed later.

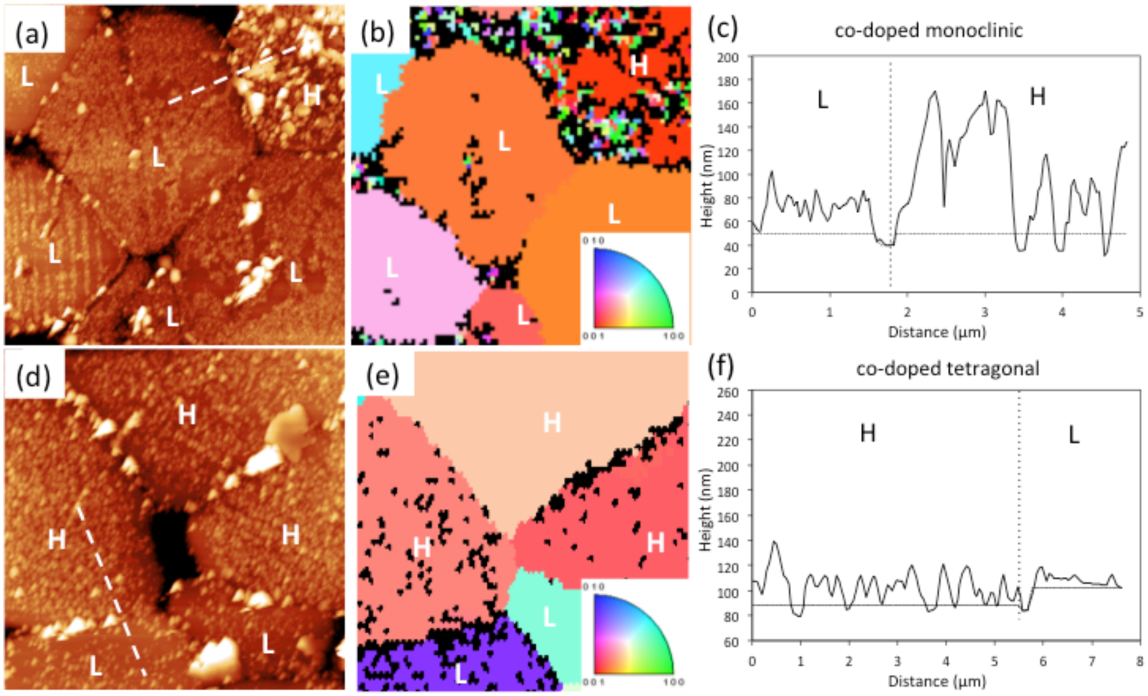

Figure 6.5. Surface topographic images taken after the reduction of Ag^+ for 30 s on the surface of (a) the x = 0.05 monoclinic sample and (d) the x = 0.175 tetragonal sample. Inverse pole figure (orientation) maps from the same areas are shown in (b) and (e), respectively. Pixels with low confidence indices are colored black. Topographic line profiles from the dashed lines in (a) and (d) are shown in (c) and (f), respectively. The vertical (horizontal) lines in (c) and (f) mark the grain boundary (height of bare grain surface). In all images, symbols denote grains of relatively high (H) or low (L) reactivities (see text).

More than 50 grains in each sample were characterized for their relative reactivity and orientation. The relative reactivity is plotted as a function of orientation (in the standard stereographic projection for the tetragonal reference frame[105]) in Fig. 6.6(a) and 6.6(b) for the x = 0.05 monoclinic and x = 0.175 tetragonal samples, respectively. Despite the somewhat subjective distinction between H and L reactive grains in the two samples, (001)-oriented grains were observed to be more highly reactive than others: as the angle between the surface orientation and [001] increases, there are fewer grains whose average heights of silver particles exceed 20 nm for the x = 0.05 (10 nm for x = 0.175) sample. These results are also consistent with the orientation-dependent reactivity observed for undoped $BiVO_4$.[105] The photo-deposition on these co-doped samples was generally higher than for the undoped sample, even with a shorter exposure time, a lower power of illumination, and a larger distance between the light source and samples, which all should decrease the reactivity[105]. It is possible that the higher electronic conductivity of the doped samples contributes to their higher reactivities.[47,149]

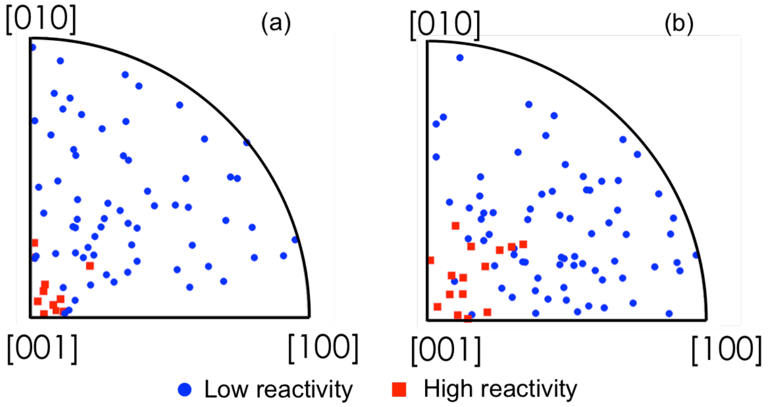

Figure 6.6. Orientation distribution of grains with high and low reactivity in (a) co-doped x = 0.05 monoclinic and (b) co-doped x = 0.175 tetragonal $Na_{0.5x}Bi_{1-0.5x}Mo_xV_{1-x}O_4$.

Figure 6.7 shows similar results to those of Fig. 6.5, but in areas selected to compare the reactivities of monoclinic and tetragonal grains with nearly identical orientations. AFM topographs after the photochemical reduction of Ag^+ (orientations maps) are given in Fig. 6.7(a) and 6.7(d) (Fig. 6.7(b) and 6.7(e)) for the monoclinic and tetragonal sample, respectively. The height profiles along the dashed lines in Fig. 6.7(a) and 6.7(d) are shown in Fig 6.7(c) and 6.7(f), respectively. The lines in Fig. 6.7(a) and (d) were chosen such that they remained within grains of similar orientations indexed in the tetragonal reference frame (marked with * in (b) and (e)). The small distortions from the tetragonal structure for the x = 0.05 sample will not significantly impact this analysis. The height of deposits on the monoclinic grain, see Fig. 6.7(c), was greater than the height of those on the tetragonal grain of the same orientation, see Fig. 6.7(d). In fact, when I compare the relative reactivities of grains of similar orientations (eight pairs), the reactivity the x = 0.05 monoclinic grains was always greater than that of the x = 0.175 tetragonal grains (the orientations and the measured reactivity of all compared grains are shown in Appendix 4, Fig. S.6). These results support the conclusion that the monoclinic sample is more reactive than the tetragonal sample.

In Fig. 6.7(a), domain selective reactivity is clearly observed for several grains in the x = 0.05 monoclinic sample, but not for the tetragonal sample. In fact, domain-to-domain variation was generally observed for the monoclinic co-doped sample, when the reactivity of the grain was low (L). In highly reactive grains, Ag^+ generally coated the entire grain, presumably from lateral growth on the surface of previously nucleated silver deposits. The domain-selective reactivity in monoclinic co-doped $Na_{0.5x}Bi_{1-0.5x}Mo_xV_{1-x}O_4$ is similar to that previously reported for undoped $BiVO_4$.[126] This indicates that the domain-specific spatially-selective reactivity of fergusonite-structured $BiVO_4$ is not restricted to a specific composition (see Appendix 4, Fig. S.5 for a comparison of PFM for the two monoclinic samples, and see Fig. S.7 for one-to-one correlation between PFM domains and photoreduction of Ag^+ on the x = 0.05 sample). Furthermore, the increased conductivity of the x = 0.05 sample appears to render the co-doped sample more reactive than the undoped sample. In a previous study of domain specific reactivity on TiO_2 supported on $BaTiO_3$, increasing the carrier concentration led to spatially uniform reactivity, presumably because the additional donors screened the polarization of the domains.[144] That does not seem to be the case for the surface of $Na_{0.5x}Bi_{1-0.5x}Mo_xV_{1-x}O_4$.

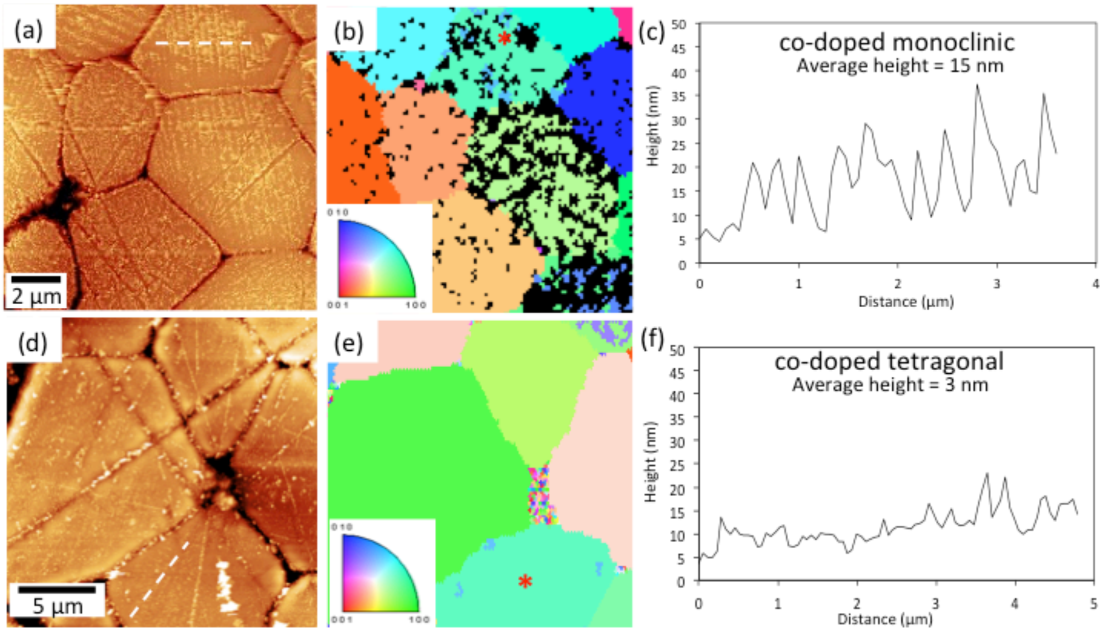

Figure 6.7. Surface topographic images taken after reduction for 10 s of Ag^+ on the surface of (a) the x = 0.05 monoclinic sample and (d) the x = 0.175 tetragonal sample. Orientation maps of the same areas are shown in (b) and (e), respectively. Topographic line profiles from the dashed lines in (a) and (d), from the grains marked with * in (b) and (e), are shown in (c) and (f), respectively. (Note: The pixels with confident index below a tolerance angle of 5° were screened on the maps seen as black pixels).

6.4 Discussion

Despite their different room temperature crystal symmetries, the orientation-dependent reactivities observed for the co-doped monoclinic and tetragonal samples are essentially the same: surfaces near (001) are more reactive than others for the photochemical reduction of Ag^+. A similar orientation dependent reactivity was observed for undoped monoclinic $BiVO_4$.[105] These results indicate that the orientation dependent reactivity is closely tied to the structure (and bonding) of the parent tetragonal scheelite phase, and that the small distortions leading to the monoclinic phase do not markedly influence orientation-dependent behavior. However, the monoclinic co-doped sample was found to be more active on any given orientation than was the tetragonal co-doped sample, which is consistent with prior studies indicating that the monoclinic phase of $BiVO_4$ is more active than the tetragonal phase.[94,150–152] That the increased photoreactivity of monoclinic $BiVO_4$ arises for every orientation indicates orientation effects are not the origin of this improvement.

Prior explanations of the better photocatalytic performance of monoclinic $BiVO_4$ over tetragonal $BiVO_4$ have been attributed to two factors associated with the monoclinic distortion: the appearance of local polarizations in the metal-oxygen environments and a change in the average electronic structure related to the changes in metal-oxygen bonding. In the tetragonal scheelite structure, the metal oxygen polyhedra are symmetric, with the cations at the center of the polyhedra. In the monoclinic fergusonite structure (sometimes called the monoclinic scheelite structure), the polyhedra are distorted and the cations are off-centered within them.[94] This results in local polar units in fergusonite, while the net polarity is zero when all summed over the entire centrosymmetric unit cell. Tokunaga *et al.*[94] proposed that these local polarizations result in a significant improvement of charge separation, and thereby enhance the reactivity of monoclinic $BiVO_4$. It is likely that these local polar units do not completely cancel at the surfaces of $BiVO_4$, where symmetry is broken, which is essentially what I measure in the PFM images that demonstrate net surface polarity in monoclinic $BiVO_4$, but not in tetragonal $BiVO_4$. That the local distortions differ near the surface was implied in Raman signals measured using different laser wavelengths.[153]

The electronic structure also changes as a result of the monoclinic distortion in $BiVO_4$, because it is directly coupled to the metal-oxygen bonding environments.[154] In $BiVO_4$, the Bi 6s lone pair is stereochemically inactive in the symmetric Bi-O environment of the tetragonal scheelite structure, but is active in the distorted environment of the monoclinic fergusonite structure.[38] When the lone-pair becomes active, it hybridizes with the valence band oxygen, contributing significantly to the valence band edge.[22,95,151,152,154,155] Concomitantly, the distortion of the V-O tetrahedra modifies the conduction band states (which are primarily V orbitals). Experimentally, there is little difference in the absorption edges of tetragonal scheelite and monoclinic fergusonite $BiVO_4$ (though a relatively large shift occurs on massive structural change to the tetragonal zircon-structured $BiVO_4$).[94,153,155,156] Therefore, there is little change to the amount of light absorbed. However, these hybridizations are believed to increase the electron and hole mobilities, which therefore improve the performance of the photocatalysts as electron and holes are more easily separated.[157] I cannot determine the role that the improved hybridization of the band edge states in the monoclinic systems played in our observations. However, whatever the role, it cannot explain the orientation-dependent reactivity of the two doped samples. It can, however, contribute to a possible improved performance for a given reaction occurring on a specific ferroelastic domain, when compared to the same reaction occurring on a similarly oriented tetragonal grain.

What prior investigations have not considered is the role that local surface polarity may play on improved reactivity. Local surface polarity is known to promote charge separation, reduce recombination, and drive electrons and holes to different reaction sites on the surface, which also results in a spatial separation of chemical reactions.[16] Here I demonstrated from PFM measurements that monoclinic co-doped $BiVO_4$ exhibits regions of varying surface polarization, similar to that reported for undoped monoclinic $BiVO_4$.[126] Moreover, the reduction of Ag^+ on the surface of the co-doped monoclinic material is spatially correlated to domains (and can be correlated to the PFM signal from domains), as reported for the undoped material.[94,105] Previously in Study 2 (Chapter 5), I also show that complementary redox reactions occur on complementary sets of domains (Fig. 5.5). This indicates that the existence of locally polar polyhedra in the centrosymmetric bulk are not the primary driver for improved performance, but that net, non-zero polar domains at the surface drive the spatial separation of electrons and holes, and therefore the separation of photochemical reactions.

In addition to the increased reactivity, the co-existence of complementary ferroelastic domains on all grains also provides sites for both reduction and oxidation on all surfaces. This makes it possible for both reduction and oxidation to happen on any orientation, which has not been observed in the previous study of polygonal $BiVO_4$.[20] We conclude that the existence local surface polarity separated into complementary domain patterns, which do not exist in the tetragonal $Na_{0.5x}Bi_{1-0.5x}Mo_xV_{1-x}O_4$, leads to the increased reactivity in monoclinic $Na_{0.5x}Bi_{1-0.5x}Mo_xV_{1-x}O_4$. While some additional benefit may arise from improved mobilities associated with the increased hybridization, the results suggest that the primary factor that increases the photocatalytic performance of monoclinic $Na_{0.5x}Bi_{1-0.5x}Mo_xV_{1-x}O_4$ is the existence of complementary sets of polar ferroelastic domains.

Increased reactivities arising from spatially varying polar domains of opposite signs are commonly seen in ferroelectrics, which possess inherently non-centrosymmtric structures.[112,134,141,158] One does not anticipate such effects in centrosymmetric structures, for which a net internal polarization is forbidden. I have previously argued that the non-zero polarizations measured at the surface of centrosymmetric $BiVO_4$ arise from flexoelectric effects.[126] Flexoelectricity is defined as a linear relationship between an electric field and a strain gradient, where the strain gradient breaks the symmetry, resulting in a local polarization. Thus, flexoelectricity is not limited to non-centrosymmetric materials.[70,69] The contribution of the polar nature of ferroelectric surfaces has been shown to spatially promote the separation of charge carriers and therefore increase reactivity in many studies.[16,57,140,159–161] Similarly, the increased reactivity of our monoclinic $BiVO_4$ samples can be attributed by the induced polar nature of surfaces from flexoelectricity, which appears to be coupled to specific sets of ferroelastic domains.

Because the composition was varied to stabilize the monoclinic and tetragonal phases of $Na_{0.5x}Bi_{1-0.5x}Mo_xV_{1-x}O_4$, I need to consider chemical effects as well. For example, the materials studied here all have slightly different colors: undoped $BiVO_4$ is a bright shade of yellow, the x = 0.05 sample is light yellow and the x = 0.175 sample is darker yellow. However, it has already been established by Zhou *et al.*[31] that the band gaps of these two compositions of $Na_{0.5x}Bi_{1-0.5x}Mo_xV_{1-x}O_4$ are comparable, indicating that they absorb approximately the same amount of light. Also, because I used narrow band illumination far from the band edge, a small shift in the band edge will not have a significant effect on the amount of light absorbed. Thus, differences in light absorption are not likely to be responsible for the differences in reactivity.

The conductivity also varies with composition, either from changes in carrier populations or mobilities. Abdi *et al.*[47] demonstrated that doping $BiVO_4$ with W increased the conductivity, which resulted in higher carrier mobility, and therefore better photocatalytic performance. Our co-doped samples have higher conductivities (by at least two orders of magnitude) than the undoped sample, but are similar to each other. The increased conductivity of the co-doped samples explains their improved reactivity when compared to the undoped sample, but does not provide a satisfactory description for the differences in reactivity observed between the doped samples. Also, the fact that both reduction and oxidation reactions can occur on any surface orientation of the sintered ceramic sample, but not the small polygonal crystals,[20] suggests that the co-existence of regions promoting oxidation and reduction on each surface improves the reactivity by promoting local charge separation and balancing the local rates of both redox reactions.

6.5 Conclusion

Complementary, domain-specific, reduction and oxidation reactions were observed on the surface of a ferroelastic monoclinic $BiVO_4$ ceramic. It suggests that surface polarizations correlated with the ferroelastic domain structure controls photogenerated charge separation. A study of the orientation dependence of the photochemical reactivity of co-doped monoclinic and tetragonal $Na_{0.5x}Bi_{1-0.5x}Mo_xV_{1-x}O_4$ showed that, for the reduction of silver, the most reactive orientation was (001) in both materials. Even though the orientation dependence of the reactivity was comparable for the two different compositions of $Na_{0.5x}Bi_{1-0.5x}Mo_xV_{1-x}O_4$, the photochemical reactivity of the monoclinic composition was greater than that of the tetragonal composition. The enhanced photochemical reactivity of the monoclinic sample is most likely caused by the ferroelastic domain structure, which leads to surface polarization measured using PFM. It is therefore likely that the improved photochemical reactivity of the monoclinic ferroelastic material arises from polar domains that transport electrons and holes to the surfaces of different domains, providing spatially distinct sites for oxidation and reduction.

Summary of the Conclusions and Future Prospects

7.1 Summary of the Conclusions

In conclusion, all studies lead to the following findings and conclusions:

(1) The photochemical properties of $Na_{0.5x}Bi_{1-0.5x}Mo_xV_{1-x}O_4$ are strongly orientation-dependent, and this orientation dependence is not strongly symmetry or composition dependent. Specifically, (001) is the most favorable orientation for reduction and (*hk*0), perpendicular to (001), is the most favorable orientation for oxidation. Together, these results can be used to design an ideal orientation combination for efficient $Na_{0.5x}Bi_{1-0.5x}Mo_xV_{1-x}O_4$ photocatalysts, and indicate that the orientation preference is driven by the bonding in the higher symmetry (high temperature) scheelite structure.

(2) Undoped $BiVO_4$ exhibits domain selectivity of photochemical reactivity. In addition, $BiVO_4$ exhibited piezoresponsive domains indicating domain polarity. Importantly, domain selectivity is correlated with the piezoresponsive domains. The domain polarity is consistent with local symmetry-breaking in the near surface region, such as a flexoelectric effect. The results suggest that piezoresponive ferroelastic domains can facilitate the separation of electrons and holes leading to the separation of the redox reactions.

(3) Doped monoclinic and doped tetragonal $BiVO_4$ exhibited the identical relationship between orientation and reactivity: (001)-oriented grains of both structured samples are most active for the reduction reaction. However, the doped monoclinic sample is more reactive than the doped tetragonal sample at any given orientation. This result demonstrates the primary

importance of the underlying similarities in the monoclinic and tetragonal samples, such as the general atomic arrangement, and the secondary importance of the resultant modification related to ferroelastic domains.

7.2 Revision of the hypotheses

This research aims to testify to these following hypotheses:

(i) (from Study1) (001)-oriented grains are more active for reduction than other grains. In addition, this preferential reduction on (001) will lead to oxidation reactions happening away from (001) grains.

(ii) (from Study 3) The formation of ferroelastic domains results in the appearance of piezoresponsive surface domains, which promote charge separation and improve the photochemical reactivity of monoclinic $BiVO_4$.

Overall, the results validate the hypotheses. The results showed that orientation and ferroelastic nature influenced photochemical reactivity of $BiVO_4$. However, the orientation plays a more important role than the ferroelastic nature. In other words, the orientation is a primary factor and the ferroelastic nature is a secondary factor affecting $BiVO_4$ photochemical reactivity.

In particular to the influence of orientation, even though the previous observations on microcrystals[20] and this research's observations on $BiVO_4$ sintered pellets are in general agreement, the $BiVO_4$ pellet offers greater insight for orientation dependence. Explicitly, due to the limited orientation on microcrystal faces, the faceted $BiVO_4$ particle can yield only the orientation dependent reactivity on {001} and {101} faces. On the other hand, with all possible orientations on surfaces of $BiVO_4$ polished pellets, a more complete understanding of the relationship between orientation and reactivity can be obtained. Despite of the agreement of the results, the mechanisms leading to the orientation-dependent reactivity in microcrystal and in a sintered polycrystalline ceramic may be different. It should be noted that grain sizes in the $BiVO_4$ pellet are relatively larger than faceted surfaces of $BiVO_4$ microcrystals. As a result, surface potential differences may play a more significant role in the microcrystal structure, if they are important. Such a surface potential difference was proposed as a mechanism to drive electrons and holes to different surfaces, which is favorable for different reactions.[20] In the case of sintered pellets, it is more difficult for a surface potential difference to drive charge carriers across grain boundaries. Thus, it is more likely that both reduction and oxidation locally occur within a grain. This explanation also supports the idea that ferroelastic domains can facilitate reduction and oxidation reactions by providing available and accessible sites for both redox reactions, such that the catalytic reactions can occur simultaneously at the surface, while being spatially distinct.

Moreover, it should be noted that this is the first observation of piezoresponive domains in a centrosymmetric material. The apparently piezoresponsive domains indicates that surfaces are locally polar, implying the existence of an internal polarization. The polar surfaces of centric bulk materials can possibly be explained by strain-gradient-induced flexoelectric effect, which can result in a broken symmetry. It should be also pointed out that flexoelectric effect is usually neglected in bulk materials due to its small magnitude; however, in ferroelastic domains with submicron dimensions, flexoelectricity could have a significant impact and result in domain polarity. Similar to ferroelectric domains, it is clear that the polarity of ferroelastic domains assists charge separation leading to a spatial separation of photochemical reactions. Additionally, $BiVO_4$ photochemical reactivity is enhanced because of ferroelastic nature.

7.3 Future prospects

This research has favorable implications to photocatalytic applications: photocatalytic properties can be improved by ferroelasticity. However, the current study is limited only to ferroelastic $BiVO_4$. It is possible that similar phenomena can occur in other ferroelastic materials. As a result, it is of great interest to expand investigation into other ferroelastic materials to identify a class of materials that can exhibit the phenomena. To limit the scope of the study, considering that the structure of monoclinic $BiVO_4$ possesses the lowest symmetry in the group, ferroelastic materials with fergusonite structure, such as $YNbO_4$[162], $YTaO_4$[163], and $LaNbO_4$[164], would be a good start for further investigation. The finding from this further study would suggest wider material options for efficient photocatalyst materials.

Based on the current results, even though they do not contradict the hypotheses, they are not conclusive yet. For example, the anisotropic reactivity has been found in many oxides, but the influential factors have not been fully understood. In this particular study, I have not attempted to comprehend the underlying mechanism leading to the variation of reactivity owing to orientation (e.g. why is {001} the most active for reduction?. Thus, future work should address this area to complete the understanding.

Similarly, the origin of piezoresponsive domains in centric materials is still ambiguous. Towards the future direction, a study to determine the underlying physics of this unexpected result should be in great detail. Because the piezoresponsive surface can be observed in only monoclinic $BiVO_4$, it suggests that $BiVO_4$'s ferroelastic transition may lead to the observed polar surface. It is postulated that the phase transition can result in a strain gradient that locally breaks the symmetry as known as flexoelectric effect.

The extent of this effect is still unknown (for example, what is the magnitude of the effect? what is the extent of the effect propagating from the surface? what factors can influence this effect?). The flexoelectric effect could be considered as a local effect,[165] meaning that it may be orientation-dependent. In particular to $BiVO_4$, it is possible that the induced polarization is aligned along [001] direction according to the direction of the largest atomic displacement in monoclinic fergusonite structure. However, at this point, there is no experimental evidence to support this postulation. Thus, as a follow-up to this postulation, the correlation between piezoresponsive extent and orientation would be of interest. In addition to experimental studies, implementing computational studies can provide a better understanding of the effect and an ability to estimate the extent of the phenomena.

Additionally, it should be noted that our explanation of higher photochemical reactivity in monoclinic $BiVO_4$ considers only the influence of the ferroelastic nature. Based on our results, the ferroelastic nature can potentially improve photochemical properties of monoclinic $BiVO_4$. Other than ferroelastic nature, many factors, such as electronic structure, can contribute to the improvement in photochemical reactivity. Previous studies have also demonstrated that monoclinic $BiVO_4$ obtained a higher photochemical reactivity than tetragonal $BiVO_4$. In this research, I neither consider nor attempt to define all factors leading to the higher reactivity in monoclinic $BiVO_4$. However, it would be promising for future work to include more factors into consideration.

Ultimately, these further studies can provide a better understanding of photochemical properties in $BiVO_4$ and also lead to a general strategy to improve photochemical properties in ferroelastic materials. More importantly, this knowledge suggests a possibility to induce ferroelectricity or piezoelectricity into centric ferroelastic materials or, in other words, create multiferroic properties in restricted materials. This potentially broadens the functionality of ferroelasticity into more practical applications, such as sensors.

References

[1] Centi, G. & Perathoner, S. Towards Solar Fuels from Water and CO_2. *ChemSusChem* **3,** 195–208 (2010).

[2] Licht, S. *et al.* Over 18% solar energy conversion to generation of hydrogen fuel; theory and experiment for efficient solar water splitting. *Int. J. Hydrog. Energy* **26,** 653–659 (2001).

[3] Pandit, A. *et al. Harnessing Solar Energy for the Production of Clean Fuel*. (European Science Foundation, 2008). at <https://openaccess.leidenuniv.nl/handle/1887/13349>

[4] Maeda, K. & Domen, K. Photocatalytic Water Splitting: Recent Progress and Future Challenges. *J. Phys. Chem. Lett.* **1,** 2655–2661 (2010).

[5] Bard, A. J. & Fox, M. A. Artificial Photosynthesis: Solar Splitting of Water to Hydrogen and Oxygen. *Acc. Chem. Res.* **28,** 141–145 (1995).

[6] Joya, K. S. & de Groot, H. J. M. Artificial Leaf Goes Simpler and More Efficient for Solar Fuel Generation. *ChemSusChem* **7,** 73–76 (2014).

[7] Luo, J. *et al.* Water photolysis at 12.3% efficiency via perovskite photovoltaics and Earth-abundant catalysts. *Science* **345,** 1593–1596 (2014).

[8] Osterloh, F. E. Inorganic nanostructures for photoelectrochemical and photocatalytic water splitting. *Chem. Soc. Rev.* **42,** 2294–2320 (2013).

[9] Osterloh, F. E. & Parkinson, B. A. Recent developments in solar water-splitting photocatalysis. *MRS Bull.* **36,** 17–22 (2011).

[10] Suib, S. L. *New and Future Developments in Catalysis: Solar Photocatalysis*. (Newnes, 2013).

[11] Zou, Z., Ye, J., Sayama, K. & Arakawa, H. Direct splitting of water under visible light irradiation with an oxide semiconductor photocatalyst. *Nature* **414,** 625–627 (2001).

[12] Valero, J. M., Obregón, S. & Colón, G. Active Site Considerations on the Photocatalytic H_2 Evolution Performance of Cu-Doped TiO_2 Obtained by Different Doping Methods. *ACS Catal.* **4,** 3320–3329 (2014).

[13] Meyerstein, D., Rabani, J., Matheson, M. S. & Meisel, D. Charge separation in photoinitiated electron transfer reactions induced by a polyelectrolyte. *J. Phys. Chem.* **82,** 1879–1885 (1978).

[14] Wang, J. & Osterloh, F. E. Limiting factors for photochemical charge separation in $BiVO_4/Co_3O_4$, a highly active photocatalyst for water oxidation in sunlight. *J. Mater. Chem. A* **2,** 9405–9411 (2014).

[15] Batzill, M. Fundamental aspects of surface engineering of transition metal oxide photocatalysts. *Energy Environ. Sci.* **4,** 3275–3286 (2011).

[16] Li, L., Salvador, P. A. & Rohrer, G. S. Photocatalysts with internal electric fields. *Nanoscale* **6,** 24–42 (2013).

[17] Rabe, K. M., Dawber, M., Lichtensteiger, C., Ahn, C. H. & Triscone, J.-M. in *Physics of Ferroelectrics* 1–30 (Springer Berlin Heidelberg, 2007). at <http://link.springer.com/chapter/10.1007/978-3-540-34591-6_1>

[18] Bhardwaj, A., Burbure, N. V. & Rohrer, G. S. Enhanced Photochemical Reactivity at the Ferroelectric Phase Transition in $Ba_{1-x}Sr_xTiO_3$. *J. Am. Ceram. Soc.* **93,** 4129–4134 (2010).

[19] Morris Hotsenpiller, P. A., Bolt, J. D., Farneth, W. E., Lowekamp, J. B. & Rohrer, G. S. Orientation Dependence of Photochemical Reactions on TiO_2 Surfaces. *J. Phys. Chem. B* **102,** 3216–3226 (1998).

[20] Li, R. *et al.* Spatial separation of photogenerated electrons and holes among {010} and {110} crystal facets of $BiVO_4$. *Nat. Commun.* **4,** 1432 (2013).

[21] Li, R., Han, H., Zhang, F., Wang, D. & Li, C. Highly efficient photocatalysts constructed by rational assembly of dual-cocatalysts separately on different facets of $BiVO_4$. *Energy Environ. Sci.* **7,** 1369–1376 (2014).

[22] Walsh, A., Yan, Y., Huda, M. N., Al-Jassim, M. M. & Wei, S.-H. Band Edge Electronic Structure of $BiVO_4$: Elucidating the Role of the Bi s and V d Orbitals. *Chem. Mater.* **21,** 547–551 (2009).

[23] Seabold, J. A. & Choi, K.-S. Efficient and Stable Photo-Oxidation of Water by a Bismuth Vanadate Photoanode Coupled with an Iron Oxyhydroxide Oxygen Evolution Catalyst. *J. Am. Chem. Soc.* **134,** 2186–2192 (2012).

[24] Wang, D. *et al.* Photocatalytic Water Oxidation on $BiVO_4$ with the Electrocatalyst as an Oxidation Cocatalyst: Essential Relations between Electrocatalyst and Photocatalyst. *J. Phys. Chem. C* **116,** 5082–5089 (2012).

[25] Huang, Z.-F., Pan, L., Zou, J.-J., Zhang, X. & Wang, L. Nanostructured bismuth vanadate-based materials for solar-energy-driven water oxidation: a review on recent progress. *Nanoscale* **6,** 14044–14063 (2014).

[26] Shibata, T., Irie, H., Tryk, D. A. & Hashimoto, K. Effect of Residual Stress on the Photochemical Properties of TiO_2 Thin Films. *J. Phys. Chem. C* **113,** 12811–12817 (2009).

[27] Giocondi, J. L. & Rohrer, G. S. Orientation Dependence of Photochemical Reduction Reactions on $SrTiO_3$ Surfaces. in *Symposium Z – Structure-Property Relationships of Oxide Surfaces and Interfaces II* **751,** (2002).

[28] Yang, J., Wang, D., Zhou, X. & Li, C. A theoretical study on the mechanism of photocatalytic oxygen evolution on $BiVO_4$ in aqueous solution. *Chem. Weinh. Bergstr. Ger.* **19,** 1320–1326 (2013).

[29] Dai, S., Gharbi, M., Sharma, P. & Park, H. S. Surface piezoelectricity: Size effects in nanostructures and the emergence of piezoelectricity in non-piezoelectric materials. *J. Appl. Phys.* **110,** 104305 (2011).

[30] Jiang, X., Huang, W. & Zhang, S. Flexoelectric nano-generator: Materials, structures and devices. *Nano Energy* **2,** 1079–1092 (2013).

[31] Zhou, D. *et al.* Phase transition, Raman spectra, infrared spectra, band gap and microwave dielectric properties of low temperature firing $(Na_{0.5x}Bi_{1-0.5x})(Mo_xV_{1-x})O_4$ solid solution ceramics with scheelite structures. *J. Mater. Chem.* **21,** 18412–18420 (2011).

[32] Kudo, A. Development of photocatalyst materials for water splitting. *Int. J. Hydrog. Energy* **31,** 197–202 (2006).

[33] Fujishima, A. & Honda, K. Electrochemical Photolysis of Water at a Semiconductor Electrode. *Nature* **238,** 37–38 (1972).

[34] Hashimoto, K., Irie, H. & Fujishima, A. TiO2 Photocatalysis: A Historical Overview and Future Prospects. *Jpn. J. Appl. Phys.* **44,** 8269 (2005).

[35] Navarro Yerga, R. M., Álvarez Galván, M. C., del Valle, F., Villoria de la Mano, J. A. & Fierro, J. L. G. Water Splitting on Semiconductor Catalysts under Visible-Light Irradiation. *ChemSusChem* **2,** 471–485 (2009).

[36] Abe, R. Recent progress on photocatalytic and photoelectrochemical water splitting under visible light irradiation. *J. Photochem. Photobiol. C Photochem. Rev.* **11,** 179–209 (2010).

[37] Kamada, K. & Soh, N. Enhanced visible-light-induced photocatalytic activity of α-Fe_2O_3 adsorbing redox enzymes. *J. Asian Ceram. Soc.* **3,** 18–21 (2015).

[38] Hara, M. *et al.* Cu_2O as a photocatalyst for overall water splitting under visible light irradiation. *Chem. Commun.* 357–358 (1998). doi:10.1039/A707440I

[39] Anandan, S. & Miyauchi, M. Improved photocatalytic efficiency of a WO_3 system by an efficient visible-light induced hole transfer. *Chem. Commun.* **48,** 4323–4325 (2012).

[40] Dunkle, S. S., Helmich, R. J. & Suslick, K. S. $BiVO_4$ as a Visible-Light Photocatalyst Prepared by Ultrasonic Spray Pyrolysis. *J. Phys. Chem. C* **113,** 11980–11983 (2009).

[41] Yan, H., Wang, X., Yao, M. & Yao, X. Band structure design of semiconductors for enhanced photocatalytic activity: The case of TiO_2. *Prog. Nat. Sci. Mater. Int.* **23,** 402–407 (2013).

[42] Choi, W., Termin, A. & Hoffmann, M. R. The Role of Metal Ion Dopants in Quantum-Sized TiO_2: Correlation between Photoreactivity and Charge Carrier Recombination Dynamics. *J. Phys. Chem.* **98,** 13669–13679 (1994).

[43] Park, H. S. *et al.* Factors in the Metal Doping of $BiVO_4$ for Improved Photoelectrocatalytic Activity as Studied by Scanning Electrochemical Microscopy and First-Principles Density-Functional Calculation. *J. Phys. Chem. C* **115,** 17870–17879 (2011).

[44] Luo, W. *et al.* Formation energy and photoelectrochemical properties of $BiVO_4$ after doping at Bi^{3+} or V^{5+} sites with higher valence metal ions. *Phys. Chem. Chem. Phys. PCCP* **15,** 1006–1013 (2013).

[45] Yin, W.-J., Wei, S.-H., Al-Jassim, M. M., Turner, J. & Yan, Y. Doping properties of monoclinic $BiVO_4$ studied by first-principles density-functional theory. *Phys. Rev. B* **83,** 155102 (2011).

[46] Abdi, F. F. & van de Krol, R. Nature and Light Dependence of Bulk Recombination in Co-Pi-Catalyzed $BiVO_4$ Photoanodes. *J. Phys. Chem. C* **116,** 9398–9404 (2012).

[47] Abdi, F. F., Savenije, T. J., May, M. M., Dam, B. & van de Krol, R. The Origin of Slow Carrier Transport in $BiVO_4$ Thin Film Photoanodes: A Time-Resolved Microwave Conductivity Study. *J. Phys. Chem. Lett.* **4,** 2752–2757 (2013).

[48] Joly, A. G. *et al.* Carrier dynamics in α-Fe_2O_3 (0001) thin films and single crystals probed by femtosecond transient absorption and reflectivity. *J. Appl. Phys.* **99,** 053521 (2006).

[49] Paracchino, A., Brauer, J. C., Moser, J.-E., Thimsen, E. & Graetzel, M. Synthesis and Characterization of High-Photoactivity Electrodeposited Cu_2O Solar Absorber by Photoelectrochemistry and Ultrafast Spectroscopy. *J. Phys. Chem. C* **116,** 7341–7350 (2012).

[50] Butler, M. A. Photoelectrolysis and physical properties of the semiconducting electrode WO_2. *J. Appl. Phys.* **48,** 1914–1920 (1977).

[51] Rettie, A. J. E. *et al.* Combined Charge Carrier Transport and Photoelectrochemical Characterization of $BiVO_4$ Single Crystals: Intrinsic Behavior of a Complex Metal Oxide. *J. Am. Chem. Soc.* **135,** 11389–11396 (2013).

[52] Miller, E. L., Wang, H. & Chu, D. Solar fuel production for a sustainable energy future: Highlights of a symposium on renewable fuels from sunlight and electricity. **22,** 69

[53] Kato, H., Hori, M., Konta, R., Shimodaira, Y. & Kudo, A. Construction of Z-scheme Type Heterogeneous Photocatalysis Systems for Water Splitting into H_2 and O_2 under Visible Light Irradiation. *Chem. Lett.* **33,** 1348–1349 (2004).

[54] Iwase, A., Ng, Y. H., Ishiguro, Y., Kudo, A. & Amal, R. Reduced Graphene Oxide as a Solid-State Electron Mediator in Z-Scheme Photocatalytic Water Splitting under Visible Light. *J. Am. Chem. Soc.* **133,** 11054–11057 (2011).

[55] Jia, Q., Iwase, A. & Kudo, A. $BiVO_4$–Ru/$SrTiO_3$:Rh composite Z-scheme photocatalyst for solar water splitting. *Chem. Sci.* **5,** 1513–1519 (2014).

[56] Bowen, C. R., Kim, H. A., Weaver, P. M. & Dunn, S. Piezoelectric and ferroelectric materials and structures for energy harvesting applications. *Energy Environ. Sci.* **7,** 25–44 (2013).

[57] Giocondi, J. L. & Rohrer, G. S. Spatial Separation of Photochemical Oxidation and Reduction Reactions on the Surface of Ferroelectric $BaTiO_3$. *J. Phys. Chem. B* **105,** 8275–8277 (2001).

[58] Ye, H., Park, H. S. & Bard, A. J. Screening of Electrocatalysts for Photoelectrochemical Water Oxidation on W-Doped $BiVO_4$ Photocatalysts by Scanning Electrochemical Microscopy. *J. Phys. Chem. C* **115,** 12464–12470 (2011).

[59] Zubko, P., Catalan, G. & Tagantsev, A. K. Flexoelectric Effect in Solids. *Annu. Rev. Mater. Res.* **43,** 387–421 (2013).

[60] Tagantsev, A. K. & Yurkov, A. S. Flexoelectric effect in finite samples. *ArXiv11100380 Cond-Mat* (2011). at <http://arxiv.org/abs/1110.0380>

[61] Lee, D. *et al.* Giant Flexoelectric Effect in Ferroelectric Epitaxial Thin Films. *Phys. Rev. Lett.* **107,** 057602 (2011).

[62] Cross, L. E. in *Frontiers of Ferroelectricity* 53–63 (Springer US, 2006). at <http://link.springer.com/chapter/10.1007/978-0-387-38039-1_5>

[63] Ma, W. & Cross, L. E. Large flexoelectric polarization in ceramic lead magnesium niobate. *Appl. Phys. Lett.* **79,** 4420–4422 (2001).

[64] Scott, J. F. Prospects for Ferroelectrics: 2012-2013;2022. *Int. Sch. Res. Not.* **2013,** e187313 (2013).

[65] Ma, W. A study of flexoelectric coupling associated internal electric field and stress in thin film ferroelectrics. *Phys. Status Solidi B* **245,** 761–768 (2008).

[66] Tagantsev, A. K. Theory of flexoelectric effect in crystals. *J. Exp. Theor. Phys.* **61,** 1246 (1985).

[67] Kogan, S. Piezoelectric effect during inhomogeneous deformation and acoustic scattering of carriers in crystals. *Sov Phys Solid State* **5,** 2069–70

[68] Majdoub, M. S., Sharma, P. & Cagin, T. Enhanced size-dependent piezoelectricity and elasticity in nanostructures due to the flexoelectric effect. *Phys. Rev. B* **77,** 125424 (2008).

[69] Yudin, P. V. & Tagantsev, A. K. Fundamentals of flexoelectricity in solids. *Nanotechnology* **24,** 432001 (2013).

[70] Tagantsev, A. K. Piezoelectricity and flexoelectricity in crystalline dielectrics. *Phys. Rev. B* **34,** 5883–5889 (1986).

[71] Quang, H. L. & He, Q.-C. The number and types of all possible rotational symmetries for flexoelectric tensors. *Proc. R. Soc. Lond. Math. Phys. Eng. Sci.* **467,** 2369–2386 (2011).

[72] Xu, T., Wang, J., Shimada, T. & Kitamura, T. Direct approach for flexoelectricity from first-principles calculations: cases for SrTiO3 and BaTiO3. *J. Phys. Condens. Matter* **25,** 415901 (2013).

[73] Hong, J., Catalan, G., Scott, J. F. & Artacho, E. The flexoelectricity of barium and strontium titanates from first principles. *J. Phys. Condens. Matter* **22,** 112201 (2010).

[74] Ponomareva, I., Tagantsev, A. K. & Bellaiche, L. Finite-temperature flexoelectricity in ferroelectric thin films from first principles. *Phys. Rev. B* **85,** 104101 (2012).

[75] Harada, J., Axe, J. D. & Shirane, G. Neutron-Scattering Study of Soft Modes in Cubic $BaTiO_3$. *Phys. Rev. B* **4,** 155–162 (1971).

[76] Gu, Y. *et al.* Flexoelectricity and ferroelectric domain wall structures: Phase-field modeling and DFT calculations. *Phys. Rev. B* **89,** 174111 (2014).

[77] Catalan, G. *et al.* Flexoelectric rotation of polarization in ferroelectric thin films. *Nat. Mater.* **10,** 963–967 (2011).

[78] Gu, Y., Hong, Z., Britson, J. & Chen, L.-Q. Nanoscale mechanical switching of ferroelectric polarization via flexoelectricity. *Appl. Phys. Lett.* **106,** 022904 (2015).

[79] Morozovska, A. N., Eliseev, E. A., Kalinin, S. V., Chen, L. Q. & Gopalan, V. Surface polar states and pyroelectricity in ferroelastics induced by flexo-roto field. *ArXiv12015085 Cond-Mat* (2012). at <http://arxiv.org/abs/1201.5085>

[80] Yokota, H. *et al.* Direct evidence of polar nature of ferroelastic twin boundaries in $CaTiO_3$ obtained by second harmonic generation microscope. *Phys. Rev. B* **89,** 144109 (2014).

[81] Salje, E. K. H., Aktas, O., Carpenter, M. A., Laguta, V. V. & Scott, J. F. Domains within domains and walls within walls: evidence for polar domains in cryogenic $SrTiO_3$. *Phys. Rev. Lett.* **111,** 247603 (2013).

[82] Biancoli, A., Fancher, C. M., Jones, J. L. & Damjanovic, D. Breaking of macroscopic centric symmetry in paraelectric phases of ferroelectric materials and implications for flexoelectricity. *Nat. Mater.* **14,** 224–229 (2015).

[83] Bhattacharya, A. K., Mallick, K. K. & Hartridge, A. Phase transition in $BiVO_4$. *Mater. Lett.* **30,** 7–13 (1997).

[84] Gotić, M., Musić, S., Ivanda, M., Šoufek, M. & Popović, S. Synthesis and characterisation of bismuth(III) vanadate. *J. Mol. Struct.* **744–747,** 535–540 (2005).

[85] Park, Y., McDonald, K. J. & Choi, K.-S. Progress in bismuth vanadate photoanodes for use in solar water oxidation. *Chem. Soc. Rev.* **42,** 2321–2337 (2013).

[86] David, W. I. F., Glazer, A. M. & Hewat, A. W. The structure and ferroelastic phase transition of $BiVO_4$. *Phase Transit.* **1,** 155–169 (1979).

[87] Sleight, A. W., Chen, H. -y., Ferretti, A. & Cox, D. E. Crystal growth and structure of $BiVO_4$. *Mater. Res. Bull.* **14,** 1571–1581 (1979).

[88] Lim, A. R., Choh, S. H. & Jang, M. S. Twin structure deduced from elastic constants of ferroelastic $BiVO_4$. *J. Phys. Condens. Matter* **1,** 1571 (1989).

[89] Lim, A. R., Choh, S. H. & Jang, M. S. Prominent ferroelastic domain walls in $BiVO_4$ crystal. *J. Phys. Condens. Matter* **7,** 7309 (1995).

[90] David, W. I. F. & Wood, I. G. Ferroelastic phase transition in $BiVO_4$: VI. Some comments on the relationship between spontaneous deformation and domain walls in ferroelastics. *J. Phys. C Solid State Phys.* **16,** 5149–5166 (1983).

[91] David, W. I. F. & Wood, I. G. Ferroelastic phase transition in $BiVO_4$: V. Temperature dependence of Bi^{3+} displacement and spontaneous strains. *J. Phys. C Solid State Phys.* **16,** 5127–5148 (1983).

[92] Kudo, A., Ueda, K., Kato, H. & Mikami, I. Photocatalytic O_2 evolution under visible light irradiation on $BiVO_4$ in aqueous $AgNO_3$ solution. *Catal. Lett.* **53,** 229–230 (1998).

[93] Kudo, A., Omori, K. & Kato, H. A Novel Aqueous Process for Preparation of Crystal Form-Controlled and Highly Crystalline $BiVO_4$ Powder from Layered Vanadates at Room Temperature and Its Photocatalytic and Photophysical Properties. *J. Am. Chem. Soc.* **121,** 11459–11467 (1999).

[94] Tokunaga, S., Kato, H. & Kudo, A. Selective Preparation of Monoclinic and Tetragonal $BiVO_4$ with Scheelite Structure and Their Photocatalytic Properties. *Chem. Mater.* **13,** 4624–4628 (2001).

[95] Stoltzfus, M. W., Woodward, P. M., Seshadri, R., Klepeis, J.-H. & Bursten, B. Structure and Bonding in $SnWO_4$, $PbWO_4$, and $BiVO_4$: Lone Pairs vs Inert Pairs. *Inorg. Chem.* **46,** 3839–3850 (2007).

[96] Payne, D. J. *et al.* The nature of electron lone pairs in $BiVO_4$. *Appl. Phys. Lett.* **98,** 212110 (2011).

[97] Zhao, Z., Li, Z. & Zou, Z. Electronic structure and optical properties of monoclinic clinobisvanite $BiVO_4$. *Phys. Chem. Chem. Phys.* **13,** 4746–4753 (2011).

[98] Roth, R. S. & Waring, J. L. Synthesis and Stability of Bismutotantalite,. Stibiotantalite and Chemically Similar ABO_4 Compounds. *Am. Mineral.* **48,** 1348–56 (1963).

[99] David, W. I. F., Glazer, A. M. & Hewat, A. W. The structure and ferroelastic phase transition of $BiVO_4$. *Phase Transit.* **1,** 155–169 (1979).

[100] Wiley: Introduction to X-Ray Powder Diffractometry - Ron Jenkins, Robert Snyder. at <http://www.wiley.com/WileyCDA/WileyTitle/productCd-0471513393.html>

[101] Suryanarayana, C. & Norton, M. G. *X-Ray Diffraction: A Practical Approach*. (Springer Science & Business Media, 2013).

[102] *Electron Backscatter Diffraction in Materials Science*. (Springer US, 2009). at <http://link.springer.com/10.1007/978-0-387-88136-2>

[103] Stojakovic, D. Electron backscatter diffraction in materials characterization. *Process. Appl. Ceram.* **6,** 1–13 (2012).

[104] Yao, N. & Wang, Z. L. *Handbook of Microscopy for Nanotechnology*. (Springer Science & Business Media, 2005).

[105] Munprom, R., Salvador, P. A. & Rohrer, G. S. The orientation dependence of the photochemical reactivity of $BiVO_4$. *J. Mater. Chem. A* **3,** 2370–2377 (2015).

[106] Vaudin, M. D. Pseudosymmetry in EBSD Patterns. *Microsc. Microanal.* **11,** 510–511 (2005).

[107] Clark, W. C. & Vondjidis, A. G. An infrared study of the photocatalytic reaction between titanium dioxide and silver nitrate. *J. Catal.* **4,** 691–696 (1965).

[108] Herrmann, J.-M., Disdier, J. & Pichat, P. Photocatalytic deposition of silver on powder titania: Consequences for the recovery of silver. *J. Catal.* **113,** 72–81 (1988).

[109] Tanaka, K., Harada, K. & Murata, S. Photocatalytic deposition of metal ions onto TiO_2 powder. *Sol. Energy* **36,** 159–161 (1986).

[110] Valenzuela, M. in *Molecular Photochemistry - Various Aspects* (ed. Saha, S.) (InTech, 2012). at <http://www.intechopen.com/books/molecular-photochemistry-various-aspects/photocatalytic-deposition-of-metal-oxides-on-semiconductor-particles-a-review>

[111] Fundamentals of Atomic Force Microscopy. *World Scientific Publishing Company* at <http://www.worldscientific.com/worldscibooks/10.1142/9343>

[112] Jungk, T., Hoffmann, Á. & Soergel, E. in *Ferroelectric Crystals for Photonic Applications* (eds. Ferraro, D. P., Grilli, D. S. & Natale, D. P. D.) 209–228 (Springer Berlin Heidelberg, 2009). at <http://link.springer.com/chapter/10.1007/978-3-540-77965-0_8>

[113] Kholkin, D. A. L., Kalinin, D. S. V., Roelofs, D. A. & Gruverman, P. A. in *Scanning Probe Microscopy* (eds. Kalinin, S. & Gruverman, A.) 173–214 (Springer New York, 2007). at <http://link.springer.com/chapter/10.1007/978-0-387-28668-6_7>

[114] Lepadatu, S., Stewart, M. & Cain, M. G. Quantification of electromechanical coupling measured with piezoresponse force microscopy. *J. Appl. Phys.* **116,** 066806 (2014).

[115] Van der Pauw, L. J. A method of measuring the resistivity and hall coefficient on lamellae arbitrary shape. *Philips Res. Rep.* **13,** 1–9 (1958).

[116] US Department of Commerce, N. Hall Effect Measurements Resistivity. at <http://www.nist.gov/pml/div683/hall_resistivity.cfm>

[117] Ramadan, A. A., Gould, R. D. & Ashour, A. On the Van der Pauw method of resistivity measurements. *Thin Solid Films* **239,** 272–275 (1994).

[118] Ma, Y., Pendlebury, S. R., Reynal, A., Le Formal, F. & Durrant, J. R. Dynamics of photogenerated holes in undoped $BiVO_4$ photoanodes for solar water oxidation. *Chem. Sci.* **5,** 2964 (2014).

[119] Abdi, F. F., Firet, N. & van de Krol, R. Efficient $BiVO_4$ Thin Film Photoanodes Modified with Cobalt Phosphate Catalyst and W-doping. *ChemCatChem* **5,** 490–496 (2013).

[120] Wang, D. *et al.* Crystal Facet Dependence of Water Oxidation on $BiVO_4$ Sheets under Visible Light Irradiation. *Chem. – Eur. J.* **17,** 1275–1282 (2011).

[121] Jiang, H. *et al.* Morphology-Dependent Photocatalytic Performance of Monoclinic $BiVO_4$ for Methyl Orange Degradation under Visible-Light Irradiation. *Chin. J. Catal.* **32,** 939–949 (2011).

[122] Obregón, S. & Colón, G. On the different photocatalytic performance of $BiVO_4$ catalysts for Methylene Blue and Rhodamine B degradation. *J. Mol. Catal. Chem.* **376,** 40–47 (2013).

[123] Lowekamp, J. B., Rohrer, G. S., Morris Hotsenpiller, P. A., Bolt, J. D. & Farneth, W. E. Anisotropic Photochemical Reactivity of Bulk TiO_2 Crystals. *J. Phys. Chem. B* **102,** 7323–7327 (1998).

[124] Zhang, X. *et al.* Selective synthesis and visible-light photocatalytic activities of $BiVO_4$ with different crystalline phases. *Mater. Chem. Phys.* **103,** 162–167 (2007).

[125] Bierlein, J. D. & Sleight, A. W. Ferroelasticity in $BiVO_4$. *Solid State Commun.* **16,** 69–70 (1975).

[126] Munprom, R., Salvador, P. A. & Rohrer, G. S. Polar Domains at the Surface of Centrosymmetric $BiVO_4$. *Chem. Mater.* **26,** 2774–2776 (2014).

[127] Torres, J. & Cervera-March, S. Kinetics of the photoassisted catalytic oxidation of Pb(II) in TiO_2 suspensions. *Chem. Eng. Sci.* **47,** 3857–3862 (1992).

[128] Marschall, R. & Wang, L. Non-metal doping of transition metal oxides for visible-light photocatalysis. *Catal. Today* **225,** 111–135 (2014).

[129] Giocondi, J. L. & Rohrer, G. S. Structure Se nsitivity of Photochemical Oxidation and Reduction Reactions on $SrTiO_3$ Surfaces. *J. Am. Ceram. Soc.* **86,** 1182–1189 (2003).

[130] Shi, J. *et al.* Interface Engineering by Piezoelectric Potential in ZnO-Based Photoelectrochemical Anode. *Nano Lett.* **11,** 5587–5593 (2011).

[131] Tiwari, D. & Dunn, S. Photochemistry on a polarisable semi-conductor: what do we understand today? *J. Mater. Sci.* **44,** 5063–5079 (2009).

[132] Giocondi, J. L. & Rohrer, G. S. Spatially Selective Photochemical Reduction of Silver on the Surface of Ferroelectric Barium Titanate. *Chem. Mater.* **13,** 241–242 (2001).

[133] Kalinin, S. V. *et al.* Atomic Polarization and Local Reactivity on Ferroelectric Surfaces: A New Route toward Complex Nanostructures. *Nano Lett.* **2,** 589–593 (2002).

[134] Halasyamani, P. S. & Poeppelmeier, K. R. Noncentrosymmetric Oxides. *Chem. Mater.* **10,** 2753–2769 (1998).

[135] Kholkin, A., Bdikin, I., Ostapchuk, T. & Petzelt, J. Room temperature surface piezoelectricity in $SrTiO_3$ ceramics via piezoresponse force microscopy. *Appl. Phys. Lett.* **93,** 222905 (2008).

[136] Manolikas, C. & Amelinckx, S. Ferroelastic domains in $BiVO_4$. *Phys. Status Solidi A* **60,** 167–172 (1980).

[137] Lim, A. R. & Jeong, S.-Y. Ferroelastic Phase Transition of $BiVO_4$ Single Crystals with Prominent W -Domain Walls by Stress-Strain Hysteresis Measurements. *J. Intell. Mater. Syst. Struct.* **21,** 915–920 (2010).

[138] Nepochatenko, V. A. & Dudnik, E. F. Ferroelastic domain walls in $BiVO_4$. *Crystallogr. Rep.* **50,** 102–107 (2005).

[139] Herrmann, J.-M., Disdier, J. & Pichat, P. Photocatalytic deposition of silver on powder titania: Consequences for the recovery of silver. *J. Catal.* **113,** 72–81 (1988).

[140] Burbure, N. V., Salvador, P. A. & Rohrer, G. S. Photochemical Reactivity of Titania Films on $BaTiO_3$ Substrates: Influence of Titania Phase and Orientation. *Chem. Mater.* **22,** 5831–5837 (2010).

[141] Schultz, A. M., Zhang, Y., Salvador, P. A. & Rohrer, G. S. Effect of Crystal and Domain Orientation on the Visible-Light Photochemical Reduction of Ag on $BiFeO_3$. *ACS Appl. Mater. Interfaces* **3,** 1562–1567 (2011).

[142] Dunn, S., Jones, P. M. & Gallardo, D. E. Photochemical Growth of Silver Nanoparticles on c- and c+ Domains on Lead Zirconate Titanate Thin Films. *J. Am. Chem. Soc.* **129,** 8724–8728 (2007).

[143] Inoue, Y., Sato, K., Sato, K. & Miyama, H. Photoassisted water decomposition by ferroelectric lead zirconate titanate ceramics with anomalous photovoltaic effects. *J. Phys. Chem.* **90,** 2809–2810 (1986).

[144] Burbure, N. V., Salvador, P. A. & Rohrer, G. S. Photochemical Reactivity of Titania Films on $BaTiO_3$ Substrates: Origin of Spatial Selectivity. *Chem. Mater.* **22,** 5823–5830 (2010).

[145] Long, M. *et al.* Efficient Photocatalytic Degradation of Phenol over $Co_3O_4/BiVO_4$ Composite under Visible Light Irradiation. *J. Phys. Chem. B* **110,** 20211–20216 (2006).

[146] Long, Cai & Kisch, H. Visible Light Induced Photoelectrochemical Properties of n-$BiVO_4$ and n-$BiVO_4$/p-Co_3O_4. *J. Phys. Chem. C* **112,** 548–554 (2008).

[147] Ma, Y., Pendlebury, S. R., Reynal, A., Le Formal, F. & Durrant, J. R. Dynamics of photogenerated holes in undoped $BiVO_4$ photoanodes for solar water oxidation. *Chem. Sci.* **5,** 2964–2973 (2014).

[148] Last, J. A., Russell, P., Nealey, P. F. & Murphy, C. J. The Applications of Atomic Force Microscopy to Vision Science. *Invest. Ophthalmol. Vis. Sci.* **51,** 6083–6094 (2010).

[149] Parmar, K. P. S. *et al.* Photocatalytic and Photoelectrochemical Water Oxidation over Metal-Doped Monoclinic $BiVO_4$ Photoanodes. *ChemSusChem* **5,** 1926–1934 (2012).

[150] Fan, H. *et al.* Effect of $BiVO_4$ Crystalline Phases on the Photoinduced Carriers Behavior and Photocatalytic Activity. *J. Phys. Chem. C* **116,** 2425–2430 (2012).

[151] Coronado, J., Fresno, F., Hernández-Alonso, M. D. & Portela, R. *Design of Advanced Photocatalytic Materials for Energy and Environmental Applications*. (Springer Science & Business Media, 2013).

[152] Kudo, A. & Hijii, S. H_2 or O_2 Evolution from Aqueous Solutions on Layered Oxide Photocatalysts Consisting of Bi^{3+} with $6s^2$ Configuration and d^0 Transition Metal Ions. *Chem. Lett.* **28,** 1103–1104 (1999).

[153] Yu, J. & Kudo, A. Effects of Structural Variation on the Photocatalytic Performance of Hydrothermally Synthesized $BiVO_4$. *Adv. Funct. Mater.* **16,** 2163–2169 (2006).

[154] Kweon, K. E. & Hwang, G. S. Hybrid density functional study of the structural, bonding, and electronic properties of bismuth vanadate. *Phys. Rev. B* **86,** 165209 (2012).

[155] Li, G., Bai, Y. & Zhang, W. F. Difference in valence band top of $BiVO_4$ with different crystal structure. *Mater. Chem. Phys.* **136,** 930–934 (2012).

[156] 156. Zhang, H. M., Liu, J. B., Wang, H., Zhang, W. X. & Yan, H. Rapid microwave-assisted synthesis of phase controlled $BiVO_4$ nanocrystals and research on photocatalytic properties under visible light irradiation. *J. Nanoparticle Res.* **10,** 767–774 (2007).

[157] 157. Kweon, K. E. & Hwang, G. S. Structural phase-dependent hole localization and transport in bismuth vanadate. *Phys. Rev. B* **87,** 205202 (2013).

[158] Zhao, H. *et al.* in *Advances in Ferroelectrics* (ed. Peliz-Barranco, A.) (InTech, 2012). at <http://www.intechopen.com/books/advances-in-ferroelectrics/ferroelectric-domain-imaging-multiferroic-films-using-piezoresponse-force-microscopy>

[159] Stock, M. & Dunn, S. Influence of the Ferroelectric Nature of Lithium Niobate to Drive Photocatalytic Dye Decolorization under Artificial Solar Light. *J. Phys. Chem. C* **116,** 20854–20859 (2012).

[160] Cui, Y., Briscoe, J. & Dunn, S. Effect of Ferroelectricity on Solar-Light-Driven Photocatalytic Activity of $BaTiO_3$—Influence on the Carrier Separation and Stern Layer Formation. *Chem. Mater.* **25,** 4215–4223 (2013).

[161] Li, L., Rohrer, G. S. & Salvador, P. A. Heterostructured Ceramic Powders for Photocatalytic Hydrogen Production: Nanostructured TiO_2 Shells Surrounding Microcrystalline $(Ba,Sr)TiO_3$ Cores. *J. Am. Ceram. Soc.* **95,** 1414–1420 (2012).

[162] Shian, S. *et al.* The tetragonal–monoclinic, ferroelastic transformation in yttrium tantalate and effect of zirconia alloying. *Acta Mater.* **69,** 196–202 (2014).

[163] Wolten, G. M. The structure of the M'-phase of $YTaO_4$, a third fergusonite polymorp*h,*. (1967).

[164] Fisher, E. S. Elastic moduli and acoustic symmetry of ferroelastic $LaNbO_4$ and $BiVO_4$. *J. Phys. Condens. Matter* **1,** 2875 (1989).

[165] Ma, W. Flexoelectric charge separation and size dependent piezoelectricity in dielectric solids. *Phys. Status Solidi B* **247,** 213–218 (2010).

Appendix 1

X-ray diffraction

XRD patterns from the three samples investigated in the $Na_{0.5x}Bi_{1-0.5x}Mo_xV_{1-x}O_4$ family with different composition: x = 0, 0.05 and 0.175. This data shows that the x = 0 and 0.05 samples are monoclinic (ferroelastic) and the x = 0.175 is tetragonal (non-ferroelastic). The data was collected using a Panalytical X'Pert Pro MPD diffractometer with a CuKα source operated at 45 kV and 40 mA. The step size and time per step of the scan were 0.0263 ° and 48 s, respectively. Also, a 1° fixed divergence slit was used in the measurement.

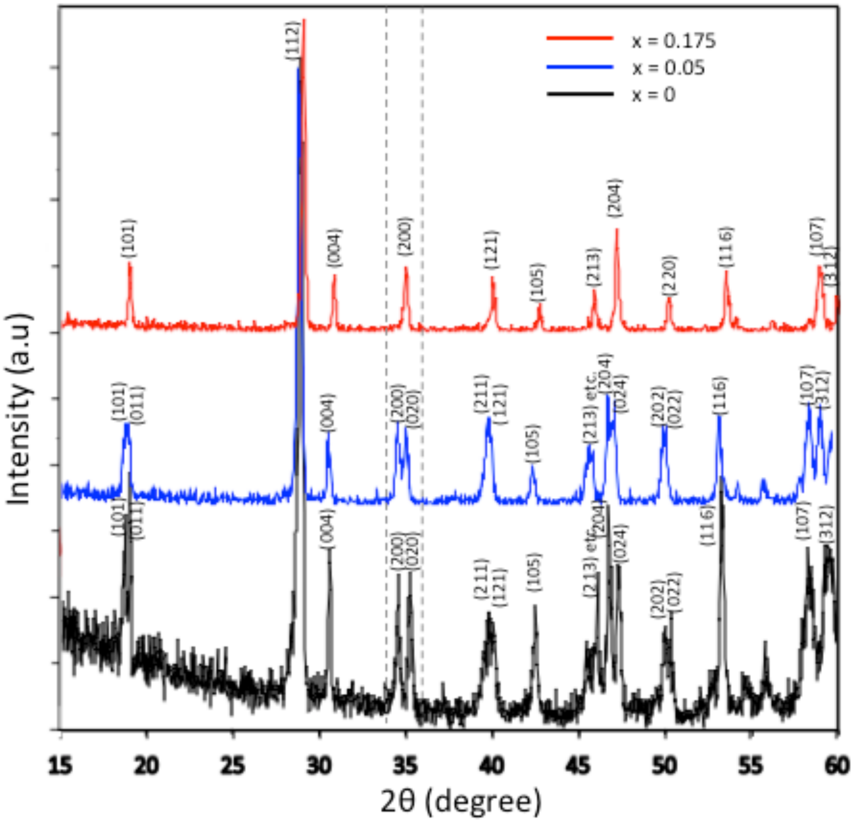

Figure S.1. X-ray diffraction patterns of $BiVO_4$ and related compounds

Appendix 2

Comment on the correlation between domain sizes and reactivity

The relationship between domain sizes and reactivity is unknown. However, it is believed that the observed reactivity in $BiVO_4$ is affected by flexoelectric polarization, which scales with size. Flexoelectricity has been known for its size-dependent behavior: specifically, the flexoelectric effect is much stronger when the size shrinks down to nanoscales owing to the relatively large strain gradient.[18] As a result, the degree of reactivity potentially depends on sizes. One prediction about the correlation between domain sizes and reactivity is that smaller sizes of domain have a stronger flexoelectric effect, which leads to higher reactivity.

On the other hand, one may argue that considering that several nm of surface relief mark the areas where domains intersect the surface in the topographic AFM images, the strain gradient should be present over vertical and horizontal lengths comparable to the domain sizes. This argument would predict that larger domain sizes show a relatively stronger effect and thereby higher reactivity.

Based on these two contradicted hypotheses, further observation was conducted in this research to comment on the domain size-reactivity correlation and qualitatively estimate the extent of the strain gradient-induced polarization effect. First, we eliminated the effect of surface orientation by observing the variation of size-dependent reactivity of similar-oriented grains. Fig. S.2 shows a common surface observed by BSE signal of scanning electron microscope. Different domains give rise to contrast in the image. The image also shows that some grains obtain domains with various sizes and alignments. Thus, the reactivity of domains within the same grain would be observed from SEM images (SE mode) so that the correlation between domain sizes and reactivity can be acquired.

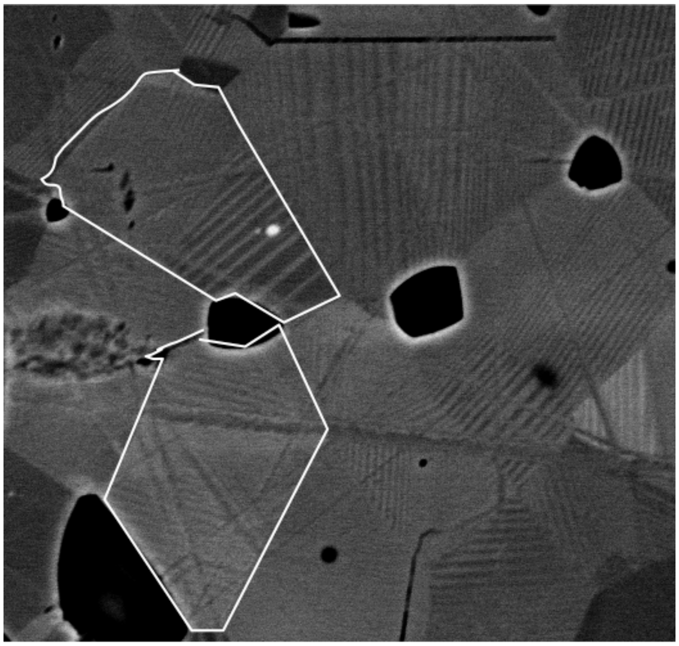

Figure S.2. SEM micrograph (BSE contrast). The outlined grains are examples of grains that have multiple domain sizes and orientations.

A couple one-to-one comparisons between BSE contrasting surface before reduction (a and c) and SE contrasting surface after reduction (b and d) were shown in Fig. S.3. The grains of interest are marked with '*', 'x' and 'o'.

Within all considered grains, SEM images showing BSE contrast (Fig. S.3 (a) and (c)) reveal sets of multiple domain widths: narrow and wide domains. Correlated with photoreduction of Ag+ shown in Fig S.3 (b) and (d), here are some points from observation:

(1) For the grain denoted with '*' (Fig. S.3 (a) and (b)), silver particles were uniformly coated, showing no domain-size dependent reactivity.

(2) Contrary, in Fig. S.3 (c) and (d) the heterogeneous reactivity was observed on the grain of interest, and importantly the reactivity was varied with domain sizes. Apparently, the wider domains in SEM images (BSE mode) obtained relatively higher reactivity. This potentially indicates that the wider domains possess a stronger strain gradient-induced polarization effect, which can result in the higher reactivity.

Based on these two example observations, domain-size dependent reactivity is not strongly apparent. In other words, domain sizes may have some degree of influence on reactivity, but they are not a dominant factor. Thus, there is no correlation between domain sizes and reactivity in monoclinic $BiVO_4$.

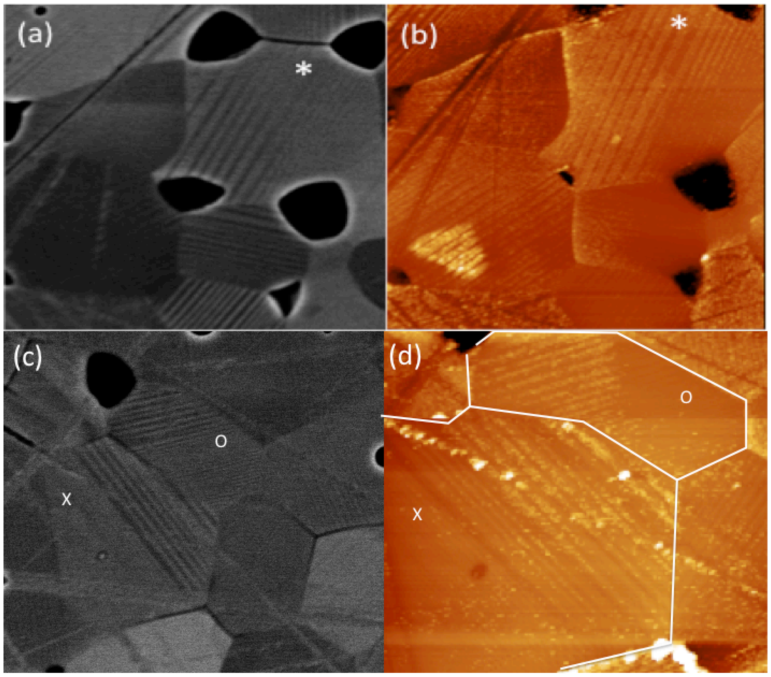

Figure S.3. SEM micrographs (BSE contrast) in (a) and (c) compare with the AFM topographic images after photochemical reduction of Ag^+ in (b) and (d), respectively. The outlined grains are examples of grains that have multiple domain sizes and orientations.

Appendix 3

EBSD measurement indexed in the monoclinic reference frame

Figure S.4 shows the comparison of the EBSD results indexed in the tetragonal reference frame and in the monoclinic reference frame of the same area. The colors in Fig. S.4(a) and S.4(b) represent the orientations of grains regarding the standard stereographic triangle of the tetragonal reference frame and that of the monoclinic reference frame, respectively. The lattice parameters used for the tetragonal reference frame are a = b = 5.147 Å, c = 11.7216 Å, while the ones used for the monoclinic reference frame are a = 5.1935 Å, b = 5.0898 Å, c = 11.6972 Å, and $\gamma = 90.38°$. The correlation between orientation and low reactivity for silver reduction was also made using the monoclinic-indexed orientation map. The correlation results from the tetragonal reference frame and the monoclinic reference frame are illustrated in Fig. S.4(c) and (d), respectively.

Using the same clean-up procedure, the map indexed with the tetragonal reference (Fig. S.4(a)) appears nicer. However, the correlations from both reference systems are in agreement. Specifically, both correlations showed that grain with low reactivity for silver reduction orient away from (001). Because of this consistency, the tetragonal reference frame is used in this thesis study.

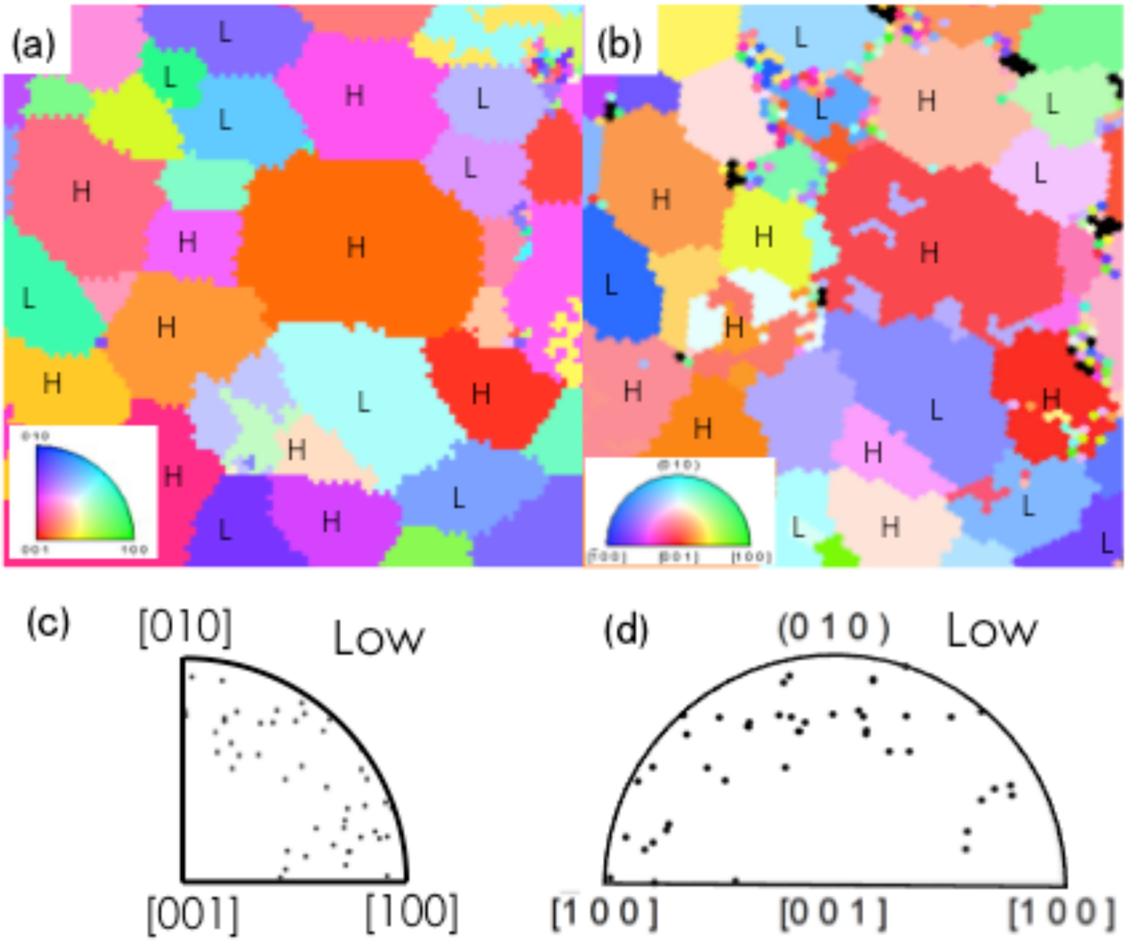

Figure S.4. A comparison of (a) color-coded inverse pole figure (IPF) map indexed with the tetragonal reference frame and (b) color-coded inverse pole figure (IPF) map indexed with the monoclinic reference frame. (c) and (d) are the correlation between orientation and low reactivity using the orientation in (a) and (b), respectively.

Appendix 4

Supplementary Information for Study 3 (Chapter 6):

Effect of ferroelastic domain structure on photochemical properties of $BiVO_4$

Three supplemental figures are provided to support the primary information given in Study 3: Effect of ferroelastic domain structure on photochemical properties of $BiVO_4$ (Chapter 6).

Figure S.5 compares directly the AFM error signal signals (a, b) and PFM phase signals (c, d) between the monoclinic undoped (a, c) and monoclinic co-doped $x = 0.05$ (b, d) samples. Contrast in the AFM images corresponds to topographical ferroelastic domains, while contrast in the PFM images is correlated to surface piezoresponse or surface polarity. These images were collected in a similar manner to those given in the main document (Fig. 6.4). Here I compare the two monoclinic samples, which show that although they have different compositions, these two monoclinic samples behave analogously under PFM measurement; piezoresponsive domains were observed.

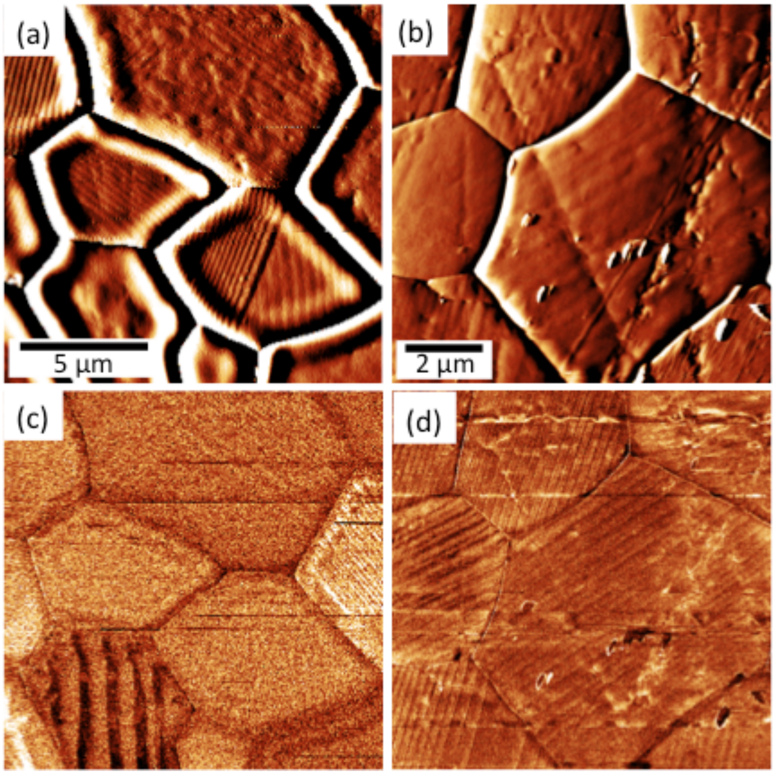

Figure S.5. Topographic AFM images of the monoclinic-structured samples: (a) x = 0 and (b) x = 0.05, each plotted as error signals with a vertical scale of 0.2 nA. (c) and (d) are PFM phase images from the same areas as given in (a) and (b), respectively. The ranges of the vertical scale for the PFM images in (c) and (d) are 17° and 2.4°, respectively.

Figure S.6 compares reactivities of eight similar-oriented grains of the co-doped monoclinic and tetragonal samples. The orientations of the 8-pair comparison are shown on a stereographic projection in (a). Also, the measured heights of deposits on the given grains are provided in the table (b). Regardless of the orientation, all given surfaces of the co-doped monoclinic sample show quantitatively greater heights of deposits, indicating that they are more reactive.

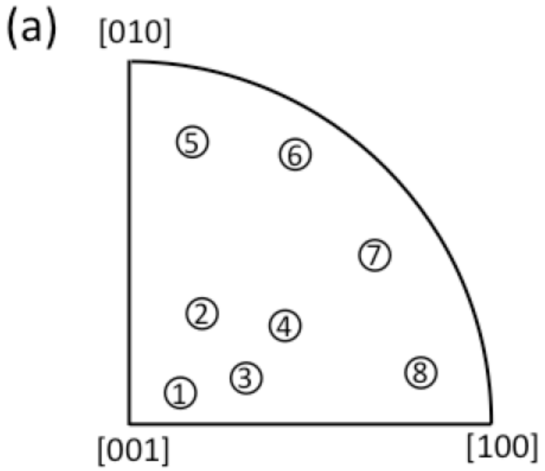

(b)

Pair no.	Average height of deposits (nm)	
	co-doped monoclinic	co-doped tetragonal
1	20	8
2	16	5
3	15	4
4	14	3
5	15	3.5
6	10	2
7	15	3
8	13	3.5

Figure S.6. Reactivity comparison of similar-oriented monoclinic and tetragonal grains (8 pairs): (a) the orientation of the 8-paired grains in the orientation space and (b) the actual average height of deposits on the given grain. Note: the average value is measured from the baseline (no deposit area).

Figure S.7 shows the one-to-one correlation between piezoresponse (a) and reactivity (b) on the monoclinic co-doped x = 0.05 sample. Both PFM contrast and reactivity have similar patterns of parallel laminar strips. This implies that domain-selective reactivity is associated with PFM domains.

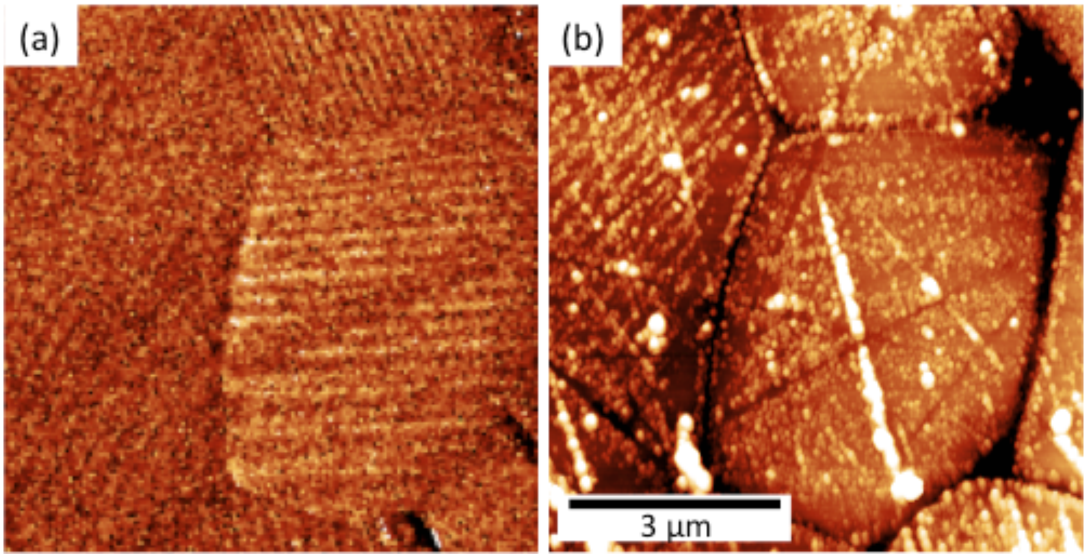

Figure S.7. A correlation between (a) piezoresponsive domains and (b) photoreduction of Ag^+ on the x = 0.05 sample. The vertical scale of PFM image in (a) is 2° and that of AFM topographic image in (b) is 50 nm.